

The Vera C. Rubin Observatory Data Preview 1

VERA C. RUBIN OBSERVATORY TEAM,¹ TATIANA ACERO-CUELLAR ,² EMILY ACOSTA ,¹ CHRISTINA L. ADAIR ,³
PRAKRUTH ADARI ,⁴ JENNIFER K. ADELMAN-MCCARTHY ,⁵ ANASTASIA ALEXOV ,¹ RUSS ALLBERRY ,¹
ROBYN ALLSMAN,¹ YUSRA ALSAYYAD ,⁶ JHONATAN AMADO ,⁵ NATHAN AMOUROUX ,⁷ PIERRE ANTILOGUS,⁸
ALEXIS ARACENA ALCAYAGA,⁹ GONZALO ARAVENA-ROJAS ,⁹ CLAUDIO H. ARAYA CORTES,⁹ ÉRIC AUBOURG ,¹⁰
TIM S. AXELROD ,¹¹ JOHN BANOVETZ ,¹² CARLOS BARRÍA,⁹ AMANDA E. BAUER ,¹³ BRIAN J. BAUMAN,¹⁴
ELLEN BECHTOL ,¹⁵ KEITH BECHTOL ,^{1,16} ANDREW C. BECKER ,¹⁷ VALERIE R. BECKER ,¹⁸ MARK G. BECKETT ,¹⁹
ERIC C. BELL ,²⁰ PEDRO H. BERNARDINELLI ,²¹ FEDERICA B. BIANCO ,^{2,22,23} ROBERT D. BLUM ,¹⁸
JOANNE BOGART,²⁴ ADAM BOLTON ,³ MICHAEL T. BOOTH,¹ JAMES F. BOSCH ,⁶ ALEXANDRE BOUCAUD ,²⁵
DOMINIQUE BOUTIGNY ,⁷ ROBERT A. BOVILL,¹ ANDREW BRADSHAW,^{3,24} JOHAN BREGEON ,²⁶ BRIAN J. BRONDEL ,²⁷
ALEX BROUGHTON ,²⁴ AUDREY BUDLONG,²⁸ DIMITRI BUFFAT,²⁶ RODOLFO CANESTRARI ,²⁹ NEVEN CAPLAR ,²⁰
JEFFREY L. CARLIN ,¹ ROSS CEBALLO ,¹⁸ COLIN ORION CHANDLER ,^{30,20,31} CHIHWAY CHANG ,³²
GLENNAVER CHARLES-EMERSON,¹ HSIN-FANG CHIANG ,³ JAMES CHIANG ,²⁴ YUMI CHOI ,³³ ERIC J. CHRISTENSEN,⁹
CHARLES F. CLAVER,¹ ANDY W. CLEMENTS,¹ JOSEPH J. COCKRUM,¹ FRANCO COLLEONI,⁹ CÉLINE COMBET ,²⁶
ANDREW J. CONNOLLY ,²¹ JULIO EDUARDO CONSTANZO CÓRDOVA ,⁹ HANS E CONTRERAS,⁹
JOHN FRANKLIN CRENSHAW ,²¹ SYLVIE DAGORET-CAMPAGNE ,³⁴ SCOTT F. DANIEL,²⁰ FELIPE DARUICH,⁹
GUILLAUME DAUBARD ,⁸ GREG DAUES,³⁵ ERIK DENNHY ,¹ STEPHANIE JH DEPPE ,¹⁸ SETH W. DIGEL ,³
PETER E. DOHERTY,³⁶ ALEX DRLICA-WAGNER ,⁵ GREGORY P. DUBOIS-FELSMANN ,³⁷ FROSSIE ECONOMOU ,¹
ORION EIGER ,^{3,24} LUKAS EISERT ,³ ALAN M. EISNER ,³⁸ ANTHONY ENGLERT ,³⁹ BADEN ERB,⁹ JUAN A. FABREGA,⁹
PARKER FAGRELIUS,¹ KEVIN FANNING ,³ ANGELO FAUSTI NETO ,¹ PETER S. FERGUSON ,^{21,16} AGNÈS FERTÉ ,³
MERLIN FISHER-LEVINE ,⁴⁰ GLORIA FONSECA ALVAREZ ,³³ MICHAEL D. FOSS,³ DOMINIQUE FOUCHEZ ,⁴¹
DAN C. FUCHS ,³ EMMANUEL GANGLER ,⁴² IGOR GAPONENKO,³ JULEN GARCIA ,⁴³ JOHN H. GATES,³
RANPAL K. GILL ,²⁷ ENRICO GIRO ,⁴⁴ THOMAS GLANZMAN ,³ ROBINSON GODOY,⁹ IAIN GOODENOW,¹
MIRANDA R. GORSUCH ,¹⁶ MICHELLE GOWER ,³⁵ MIKAEL GRANVIK ,^{45,46} SARAH GREENSTREET ,³³ WEN GUAN ,¹²
THIBAULT GUILLEMIN ,⁷ LEANNE P. GUY ,⁹ DIANE HASCALL,³ AREN NATHANIEL HEINZE ,²¹ FABIO HERNANDEZ ,⁴⁷
KENNETH HERNER ,⁵ ARDIS HERROLD,¹ CLARE R. HIGGS ,¹⁸ JOSHUA HOBLITT ,¹ ERIN LEIGH HOWARD ,²⁰
MINHEE HYUN ,⁹ PATRICK INGRAHAM ,¹¹ DAVID H. IRVING ,¹⁸ ŽELJKO IVEŽIĆ ,^{1,20} SUZANNE H. JACOBY,¹
BUELL T. JANNUZI ,⁴⁸ SREEVANI JARUGULA ,⁵ M. JAMES JEE ,^{49,50} TIM JENNESS ,¹ TOBY C. JENNINGS ,³
ANDREA JEREMIE ,⁷ GARRETT JERNIGAN,^{51,*} DAVID JIMÉNEZ MEJÍAS,⁹ ANTHONY S. JOHNSON ,³ R. LYNNE JONES ,²⁰
ROGER WILLIAM LEWIS JONES ,⁵² CLAIRE JURAMY-GILLES ,⁸ MARIO JURIĆ ,²¹ STEVEN M. KAHN ,⁵³
J. BRYCE KALMBACH ,³ YIJUNG KANG ,^{24,9} ARUN KANNAWADI ,^{54,6} JEFFREY P. KANTOR,¹ EDWARD KARAVAKIS ,¹²
KSHITIJA KELKAR ,⁹ LEE S. KELVIN ,⁶ IVAN V. KOTOV,¹² GÁBOR KOVÁCS ,²¹ MIKOŁAJ KOWALIK ,³⁵
VICTOR L. KRABBENDAM,¹ K. SIMON KRUGHOFF ,^{1,*} PETR KUBÁNEK ,⁹ JACOB A. KURLANDER ,²¹ MILE KUSULJA,²⁶
CRAIG S. LAGE ,⁵⁰ P. J. A. LAGO ,²⁷ KATHERINE LALIOTIS ,⁵⁵ TRAVIS LANGE ,³ DIDIER LAPORTE,⁸
RYAN M. LAU ,³³ JUAN CARLOS LAZARTE,³ QUENTIN LE BOULC'H ,⁴⁷ PIERRE-FRANÇOIS LÉGET ,⁶
LAURENT LE GUILLOU ,⁸ BENJAMIN LEVINE ,⁴ MING LIANG,¹ SHUANG LIANG,³ KIAN-TAT LIM ,³
ANJA VON DER LINDEM ,⁴ HUAN LIN ,⁵ MARGAUX LOPEZ ,³ JUAN J. LOPEZ TORO,⁹ PETER LOVE,⁵²
ROBERT H. LUPTON ,⁶ NATE B. LUST ,⁶ LAUREN A. MACARTHUR ,⁶ SEAN PATRICK MACBRIDE ,⁵⁶
GREG M. MADEJSKI,²⁴ GABRIELE MAINETTI ,⁴⁷ STEVEN J. MARGHEIM ,²⁷ THOMAS W. MARKIEWICZ ,³
PHIL MARSHALL ,³ STUART MARSHALL,²⁴ GUIDO MAULEN,⁹ MORGAN MAY,^{57,12} JEREMY MCCORMICK ,³
DAVID MCKAY ,⁵⁸ ROBERT MCKERCHER,¹ GUILLEM MEGIAS HOMAR ,^{59,24} AARON M. MEISNER ,³³
FELIPE MENANTEAU,³⁵ HEATHER R. MENTZER ,³⁸ KRISTEN METZGER,¹⁸ JOSHUA E. MEYERS ,²⁴ MICHELLE MILLER,³³
DAVID J. MILLS,¹ JOACHIM MOEYENS ,²¹ MARC MONIEZ,³⁴ FRED E. MOOLEKAMP ,⁶⁰ C. A. L. MORALES MARÍN ,⁹
FRITZ MUELLER ,³ JAMES R. MULLANEY ,⁶¹ FREDDY MUÑOZ ARANCIBIA,¹ KATE NAPIER ,²⁴ HOMER NEAL,³
ERIC H. NEILSEN, JR. ,⁵ JEREMY NEVEU ,³⁴ TIMOTHY NOBLE,⁶² ERFAN NOURBAKHS ,⁶ KNUT OLSEN ,³³
WILLIAM O'MULLANE ,⁹ DMITRY ONOPRIENKO,³ MARCO ORIUNNO ,³ SHAWN OSIER,³ RUSSELL E. OWEN,²⁰
AASHAY PAI ,³² JOHN K. PAREJKO ,²⁰ HYE YUN PARK ,⁵⁴ JAMES B. PARSONS,^{35,*} MARIA T. PATTERSON ,²⁰
MARINA S. PAVLOVIC ,⁹ KARLA PEÑA RAMÍREZ ,⁹ JOHN R. PETERSON ,⁶³ STEPHEN R. PIETROWICZ ,³⁵
ANDRÉS A. PLAZAS MALAGÓN ,^{3,24} REBEKAH POLEN,⁵⁴ HANNAH MARY MARGARET POLLEK,³ PAUL A. PRICE ,⁶

50 BRUNO C. QUINT ,¹ JOSÉ MIGUEL QUINTERO MARIN,⁹ MARKUS RABUS ,⁶⁴ BENJAMIN RACINE ,⁴¹ VELJKO RADEKA,¹²
 51 MANON RAMEL,²⁶ ARIANNA RANABHAT ,⁶⁵ ANDREW P. RASMUSSEN ,²⁴ DAVID A. RATHFELDER,⁶⁶
 52 MEREDITH L. RAWLS ,^{20,21} SOPHIE L. REED ,⁶ KEVIN A. REIL ,³ DAVID J. REISS,²⁰ MICHAEL A. REUTER ,¹
 53 TIAGO RIBEIRO ,¹ MICKAEL RIGAULT ,⁶⁷ VINCENT J. RIOT ,¹⁴ STEVEN M. RITZ ,³⁸ MARIO F. RIVERA,⁹
 54 BRANT E. ROBERTSON ,³⁸ WILLIAM ROBY ,³⁷ GABRIELE RODEGHIERO ,⁶⁸ AARON ROODMAN ,²⁴
 55 LUCA ROSIGNOLI ,^{69,68} CÉCILE ROUCELLE ,²⁵ MATTHEW R. RUMORE ,¹² STEFANO RUSSO,⁸ ELI S. RYKOFF ,²⁴
 56 ANDREI SALNIKOV ,³ BRUNO O. SÁNCHEZ ,⁴¹ DAVID SANMARTIM ,⁹ CLARE SAUNDERS ,⁶ RAFE H. SCHINDLER,²⁴
 57 SAMUEL J. SCHMIDT ,⁵⁰ JACQUES SEBAG,⁹ BRIAN SELVY,¹ EDGARD ESTEBAN SEPULVEDA VALENZUELA,⁹
 58 GONZALO SERICHE ,⁹ JACQUELINE C. SERON-NAVARRETE ,⁹ IGNACIO SEVILLA-NOARBE ,⁷⁰ ALYSHA SHUGART ,⁹
 59 JONATHAN SICK ,^{71,1} CRISTIÁN SILVA ,⁹ MATHEW C. SIMS ,⁷² JALADH SINGHAL ,³⁷ KEVIN BENJAMIN SIRUNO,⁹
 60 COLIN T. SLATER ,²⁰ BRIANNA M. SMART ,²⁰ ADAM SNYDER ,⁵⁰ CHRISTINE SOLDAHL,³
 61 IOANA SOTUELA ELORRIAGA ,⁹ BRIAN STALDER ,¹ HERNAN STOCKEBRAND ,⁹ ALAN L. STRAUSS ,¹⁸
 62 MICHAEL A. STRAUSS ,⁶ KRZYSZTOF SUBERLAK ,²⁰ IAN S. SULLIVAN ,²⁰ JOHN D. SWINBANK ,^{73,6} DIEGO TAPIA ,⁹
 63 ALESSIO TARANTO ,^{68,69} DAN S. TARANU ,⁶ JOHN GREGG THAYER ,³ SANDRINE THOMAS ,¹
 64 ADAM J. THORNTON ,¹ ROBERTO TIGHE,⁹ LAURA TORIBIO SAN CIPRIANO,⁷⁰ TE-WEI TSAI ,¹ DOUGLAS L. TUCKER ,⁵
 65 MAX TURRI,³ J. ANTHONY TYSON ,⁵⁰ ELANA K. URBACH ,⁷⁴ YOUSUKE UTSUMI ,⁷⁵ BRIAN VAN KLAVEREN,³
 66 WOUTER VAN REEVEN ,⁹ PETER ANTHONY VAUCHER ,³ PAULINA VENEGAS,⁹ APRAJITA VERMA ,⁷⁶
 67 ANTONIA SIERRA VILLARREAL ,³ STELIOS VOUTSINAS ,¹ CHRISTOPHER W. WALTER ,⁵⁴ YUANKUN (DAVID) WANG ,²¹
 68 CHRISTOPHER Z. WATERS ,⁶ CHRISTINA C. WILLIAMS ,³³ BETH WILLMAN ,⁷⁷ MATTHIAS WITTGEN ,³
 69 W. M. WOOD-VASEY ,⁷⁸ WEI YANG ,³ ZHAOYU YANG ,¹² BRIAN P. YANNY ,⁵ PETER YOACHIM ,²⁰
 70 TIANQING ZHANG ,⁷⁸ AND CONGHAO ZHOU ,³⁸

¹ *Vera C. Rubin Observatory Project Office, 950 N. Cherry Ave., Tucson, AZ 85719, USA*

² *Department of Physics and Astronomy, University of Delaware, Newark, DE 19716-2570, USA*

³ *SLAC National Accelerator Laboratory, 2575 Sand Hill Rd., Menlo Park, CA 94025, USA*

⁴ *Department of Physics and Astronomy, Stony Brook University, Stony Brook, NY 11794, USA*

⁵ *Fermi National Accelerator Laboratory, P. O. Box 500, Batavia, IL 60510, USA*

⁶ *Department of Astrophysical Sciences, Princeton University, Princeton, NJ 08544, USA*

⁷ *Université Savoie Mont-Blanc, CNRS/IN2P3, LAPP, 9 Chemin de Bellevue, F-74940 Annecy-le-Vieux, France*

⁸ *Sorbonne Université, Université Paris Cité, CNRS/IN2P3, LPNHE, 4 place Jussieu, F-75005 Paris, France*

⁹ *Vera C. Rubin Observatory, Avenida Juan Cisternas #1500, La Serena, Chile*

¹⁰ *Université Paris Cité, CNRS/IN2P3, CEA, APC, 4 rue Elsa Morante, F-75013 Paris, France*

¹¹ *Steward Observatory, The University of Arizona, 933 N. Cherry Ave., Tucson, AZ 85721, USA*

¹² *Brookhaven National Laboratory, Upton, NY 11973, USA*

¹³ *Yerkes Observatory, 373 W. Geneva St., Williams Bay, WI 53191, USA*

¹⁴ *Lawrence Livermore National Laboratory, 7000 East Avenue, Livermore, CA 94550, USA*

¹⁵ *Wisconsin IceCube Particle Astrophysics Center, University of Wisconsin—Madison, Madison, WI 53706, USA*

¹⁶ *Department of Physics, University of Wisconsin-Madison, Madison, WI 53706, USA*

¹⁷ *Amazon Web Services, Seattle, WA 98121, USA*

¹⁸ *Vera C. Rubin Observatory/NSF NOIRLab, 950 N. Cherry Ave., Tucson, AZ 85719, USA*

¹⁹ *Institute for Astronomy, University of Edinburgh, Royal Observatory, Blackford Hill, Edinburgh EH9 3HJ, UK*

²⁰ *University of Washington, Dept. of Astronomy, Box 351580, Seattle, WA 98195, USA*

²¹ *Institute for Data-intensive Research in Astrophysics and Cosmology, University of Washington, 3910 15th Avenue NE, Seattle, WA 98195, USA*

²² *Joseph R. Biden, Jr., School of Public Policy and Administration, University of Delaware, Newark, DE 19717 USA*

²³ *Data Science Institute, University of Delaware, Newark, DE 19717 USA*

²⁴ *Kavli Institute for Particle Astrophysics and Cosmology, SLAC National Accelerator Laboratory, 2575 Sand Hill Rd., Menlo Park, CA 94025, USA*

²⁵ *Université Paris Cité, CNRS/IN2P3, APC, 4 rue Elsa Morante, F-75013 Paris, France*

²⁶ *Université Grenoble Alpes, CNRS/IN2P3, LPSC, 53 avenue des Martyrs, F-38026 Grenoble, France*

²⁷ *Vera C. Rubin Observatory/NSF NOIRLab, Casilla 603, La Serena, Chile*

²⁸ *University of Washington, Dept. of Physics, Box 351580, Seattle, WA 98195, USA*

²⁹ *INAF Istituto di Astrofisica Spaziale e Fisica Cosmica di Palermo, Via Ugo la Malfa 153, 90146, Palermo, Italy*

³⁰ *LSST Interdisciplinary Network for Collaboration and Computing, Tucson, USA*

³¹ *Department of Astronomy and Planetary Science, Northern Arizona University, P.O. Box 6010, Flagstaff, AZ 86011, USA*

³² *Department of Astronomy and Astrophysics, University of Chicago, 5640 South Ellis Avenue, Chicago, IL 60637, USA*

³³ *NSF NOIRLab, 950 N. Cherry Ave., Tucson, AZ 85719, USA*

106 ³⁴Université Paris-Saclay, CNRS/IN2P3, IJCLab, 15 Rue Georges Clemenceau, F-91405 Orsay, France
 107 ³⁵NCSA, University of Illinois at Urbana-Champaign, 1205 W. Clark St., Urbana, IL 61801, USA
 108 ³⁶Smithsonian Astrophysical Observatory, 60 Garden St., Cambridge MA 02138, USA
 109 ³⁷Caltech/IPAC, California Institute of Technology, MS 100-22, Pasadena, CA 91125-2200, USA

110 ³⁸Santa Cruz Institute for Particle Physics and Physics Department, University of California-Santa Cruz, 1156 High St., Santa Cruz,
 111 CA 95064, USA

112 ³⁹Department of Physics, Brown University, 182 Hope Street, Providence, RI 02912, USA

113 ⁴⁰D4D CONSULTING LTD., Suite 1 Second Floor, Everdene House, Deansleigh Road, Bournemouth, UK BH7 7DU

114 ⁴¹Aix Marseille Université, CNRS/IN2P3, CPPM, 163 avenue de Luminy, F-13288 Marseille, France

115 ⁴²Université Clermont Auvergne, CNRS/IN2P3, LPCA, 4 Avenue Blaise Pascal, F-63000 Clermont-Ferrand, France

116 ⁴³C. Iñaki Goenaga, 5, 20600, Guipúzcoa, Spain

117 ⁴⁴INAF Osservatorio Astronomico di Trieste, Via Giovan Battista Tiepolo 11, 34143, Trieste, Italy

118 ⁴⁵Department of Physics, P.O. Box 64, 00014 University of Helsinki, Finland

119 ⁴⁶Asteroid Engineering Laboratory, Luleå University of Technology, Box 848, SE-981 28 Kiruna, Sweden

120 ⁴⁷CNRS/IN2P3, CC-IN2P3, 21 avenue Pierre de Coubertin, F-69627 Villeurbanne, France

121 ⁴⁸University of Arizona, Department of Astronomy and Steward Observatory, 933 N. Cherry Ave, Tucson, AZ 85721, USA

122 ⁴⁹Department of Astronomy, Yonsei University, 50 Yonsei-ro, Seoul 03722, Republic of Korea

123 ⁵⁰Physics Department, University of California, One Shields Avenue, Davis, CA 95616, USA

124 ⁵¹Space Sciences Lab, University of California, 7 Gauss Way, Berkeley, CA 94720-7450, USA

125 ⁵²Lancaster University, Lancaster, UK

126 ⁵³Physics Department, University of California, 366 Physics North, MC 7300 Berkeley, CA 94720, USA

127 ⁵⁴Department of Physics, Duke University, Durham, NC 27708, USA

128 ⁵⁵Center for Cosmology and Astro-Particle Physics, The Ohio State University, Columbus, OH 43210, USA

129 ⁵⁶Physik-Institut, University of Zurich, Winterthurerstrasse 190, 8057 Zurich, Switzerland

130 ⁵⁷Department of Physics Columbia University, New York, NY 10027, USA

131 ⁵⁸EPCC, University of Edinburgh, 47 Potterrow, Edinburgh, EH8 9BT, UK

132 ⁵⁹Department of Aeronautics and Astronautics, Stanford University, Stanford, CA 94305, USA

133 ⁶⁰soZen Inc., 105 Clearview Dr, Penfield, NY 14526

134 ⁶¹Astrophysics Research Cluster, School of Mathematical and Physical Sciences, University of Sheffield, Sheffield, S3 7RH, United
 135 Kingdom

136 ⁶²Science and Technology Facilities Council, Rutherford Appleton Laboratory, Harwell, UK

137 ⁶³Department of Physics and Astronomy, Purdue University, 525 Northwestern Ave., West Lafayette, IN 47907, USA

138 ⁶⁴Departamento de Matemática y Física Aplicadas, Facultad de Ingeniería, Universidad Católica de la Santísima Concepción, Alonso de
 139 Rivera 2850, Concepción, Chile

140 ⁶⁵Australian Astronomical Optics, Macquarie University, North Ryde, NSW, Australia

141 ⁶⁶AURA, 950 N. Cherry Ave., Tucson, AZ 85719, USA

142 ⁶⁷Université Claude Bernard Lyon 1, CNRS/IN2P3, IP2I, 4 Rue Enrico Fermi, F-69622 Villeurbanne, France

143 ⁶⁸INAF Osservatorio di Astrofisica e Scienza dello Spazio Bologna, Via P. Gobetti 93/3, 40129, Bologna, Italy

144 ⁶⁹Department of Physics and Astronomy (DIFA), University of Bologna, Via P. Gobetti 93/2, 40129, Bologna, Italy

145 ⁷⁰Centro de Investigaciones Energéticas, Medioambientales y Tecnológicas, Av. Complutense 40, 28040 Madrid, Spain

146 ⁷¹J.Sick Codes Inc., Penetanguishene, Ontario, Canada

147 ⁷²Science and Technology Facilities Council, UK Research and Innovation, Polaris House, North Star Avenue, Swindon, SN2 1SZ, UK

148 ⁷³ASTRON, Oude Hoogeveensedijk 4, 7991 PD, Dwingeloo, The Netherlands

149 ⁷⁴Department of Physics, Harvard University, 17 Oxford St., Cambridge MA 02138, USA

150 ⁷⁵National Astronomical Observatory of Japan, Chile Observatory, Los Abedules 3085, Vitacura, Santiago, Chile

151 ⁷⁶Department of Physics, University of Oxford, Denys Wilkinson Building, Keble Road, Oxford, OX1 3RH, UK

152 ⁷⁷LSST Discovery Alliance, 933 N. Cherry Ave., Tucson, AZ 85719, USA

153 ⁷⁸Department of Physics and Astronomy, University of Pittsburgh, 3941 O'Hara Street, Pittsburgh, PA 15260, USA

154 (Dated: December 5, 2025)

ABSTRACT

155 We present Rubin Data Preview 1 (DP1), the first data from the NSF-DOE Vera C. Rubin Observatory, comprising raw and calibrated single-epoch images, coadds, difference images, detection
 156 catalogs, and ancillary data products. DP1 is based on 1792 optical/near-infrared exposures ac-
 157 quired over 48 distinct nights by the Rubin Commissioning Camera, LSSTComCam, on the Si-

159 Simonyi Survey Telescope at the Summit Facility on Cerro Pachón, Chile in late 2024. DP1 covers
 160 ~ 15 deg 2 distributed across seven roughly equal-sized non-contiguous fields, each independently ob-
 161 served in six broad photometric bands, *ugrizy*. The median FWHM of the point-spread function
 162 across all bands is approximately 1''.14, with the sharpest images reaching about 0''.58. The 5 σ point
 163 source depths for coadded images in the deepest field, Extended Chandra Deep Field South, are:
 164 $u = 24.55, g = 26.18, r = 25.96, i = 25.71, z = 25.07, y = 23.1$. Other fields are no more than 2.2
 165 magnitudes shallower in any band, where they have nonzero coverage. DP1 contains approximately
 166 2.3 million distinct astrophysical objects, of which 1.6 million are extended in at least one band in
 167 coadds, and 431 solar system objects, of which 93 are new discoveries. DP1 is approximately 3.5 TB
 168 in size and is available to Rubin data rights holders via the Rubin Science Platform, a cloud-based
 169 environment for the analysis of petascale astronomical data. While small compared to future LSST
 170 releases, its high quality and diversity of data support a broad range of early science investigations
 171 ahead of full operations in late 2025.

172 *Keywords:* Rubin Observatory – LSST

1. INTRODUCTION

173 The National Science Foundation (NSF)–Department
 174 of Energy (DOE) Vera C. Rubin Observatory is a
 175 ground-based, wide-field optical/near-infrared facility
 176 located on Cerro Pachón in northern Chile. Named in
 177 honor of Vera C. Rubin, a pioneering astronomer whose
 178 groundbreaking work in the 20th century provided the
 179 first convincing evidence for the existence of dark matter
 180 (V. C. Rubin & W. K. Ford 1970; V. C. Rubin et al.
 181 1980), the observatory’s prime mission is to carry out the
 182 Legacy Survey of Space and Time (formerly Large Syn-
 183 optic Survey Telescope) (LSST) (Ž. Ivezić et al. 2019a).
 184 This 10-year survey is designed to obtain rapid-cadence,
 185 multi-band imaging of the entire visible southern sky
 186 approximately every 3–4 nights. Over its main 18,000
 187 deg 2 footprint, the LSST is expected to reach a depth
 188 of ~ 27 magnitude in the r-band, with ~ 800 visits per
 189 pointing in all filters (F. B. Bianco et al. 2022).

190 The Rubin Observatory system consists of four main
 191 components: the Simonyi Survey Telescope, featuring
 192 an 8.4 m diameter (6.5 m effective aperture) primary
 193 mirror that delivers a wide field of view; a 3.2-gigapixel
 194 camera, capable of imaging 9.6 square degrees per ex-
 195 posure⁷⁹ with seeing-limited quality in six broadband
 196 filters, *ugrizy* (320–1050 nm); an automated Data Man-
 197 agement System that processes and archives tens of ter-
 198 abytes of data per night, generating science-ready data
 199 products within minutes for a global community of sci-
 200 entists; and an Education and Public Outreach (EPO)

202 program that provides real-time data access, interactive
 203 tools, and educational content to engage the public. The
 204 integrated system’s étendue⁸⁰ of 319 m 2 deg 2 , is over an
 205 order of magnitude larger than that of any previous op-
 206 tical observatory, enabling a fast, large-scale survey with
 207 exceptional depth in a fraction of the time compared to
 208 other observatories.

209 The observatory’s design is driven by four key science
 210 themes: probing dark energy and dark matter; taking
 211 an inventory of the solar system; exploring the tran-
 212 sient and variable optical sky; and mapping the Milky
 213 Way (Ž. Ivezić et al. 2019a). These themes inform the
 214 optimization of a range of system parameters, includ-
 215 ing image quality, photometric and astrometric accu-
 216 racy, the depth of a single visit and the co-added survey
 217 depth, the filter complement, the total number of visits
 218 per pointing as well as the distribution of visits on the
 219 sky, and total sky coverage. Additionally, they inform
 220 the design of the data processing and access systems.
 221 By optimizing the system parameters to support a wide
 222 range of scientific goals, we maximize the observatory’s
 223 scientific output across all areas, making Rubin a pow-
 224 erful discovery machine capable of addressing a broad
 225 range of astrophysical questions.

226 Throughout the duration of the LSST, Rubin Obser-
 227 vatory will issue a series of Data Releases, each repre-
 228 senting a complete reprocessing of all LSST data col-
 229 lected up to that point. Prior to the start of the LSST
 230 survey, commissioning activities will generate a signifi-
 231 cant volume of science-grade data. To make this early
 232 data available to the community, the Rubin Early Sci-
 233 ence Program (L. P. Guy et al. 2025) was established.

^{*} Author is deceased

⁷⁹ We define an “exposure” as the process of exposing all detectors in the focal plane. It is synonymous with the term “visit” in DP1. By contrast, an “image” is the output of a single detector following an exposure.

⁸⁰ The product of the primary mirror area and the angular area of its field of view for a given set of observing conditions.

234 One key component of this program is a series of Data
 235 Previews; early versions of the **LSST** Data Releases.
 236 These previews include preliminary data products de-
 237 rived from both simulated and commissioning data,
 238 which, together with early versions of the data access
 239 services, are intended to support high-impact early sci-
 240 ence, facilitate community readiness, and inform the de-
 241 velopment of Rubin’s operational capabilities ahead of
 242 the start of full survey operations. All data and services
 243 provided through the Rubin Early Science Program are
 244 offered on a shared-risk basis⁸¹.

245 This paper describes Rubin’s second of three planned
 246 Data Previews: **Data Preview 1 (DP1)** (NSF-DOE Vera
 247 C. Rubin Observatory 2025a). The first, **Data Preview**
 248 **0 (DP0)**⁸², contained data products produced from the
 249 processing of simulated **LSST**-like data sets. These were
 250 released together with a very early version of the Rubin
 251 **Science Platform** (M. Jurić et al. 2019), which provided
 252 the data access services. **DP0** was released in multiple
 253 phases; DP0.1, DP0.2, and DP0.3, each building upon
 254 the previous one and incorporating new data and func-
 255 tionalities. DP0.1 and DP0.2 used data from the Cos-
 256 moDC2 simulations (**LSST Dark Energy Science Collab-**
 257 **oration (LSST DESC)** et al. 2021) prepared by the Dark
 258 Energy Science Collaboration (DESC), whereas DP0.3
 259 is based on simulated datasets from the Solar System
 260 Science Collaboration (SSSC).

261 **DP1** contains data products derived from the repro-
 262 cessing of science-grade exposures acquired by the **Ru-**
 263 **bin Commissioning Camera (LSSTComCam)**, in late
 264 2024. The third and final Data Preview, **Data Preview**
 265 **2 (DP2)**, is planned to be based on a reprocessing of all
 266 science-grade data taken with the Rubin’s **LSST Science**
 267 **Camera (LSSTCam)** during commissioning.

268 All Rubin Data Releases and Previews are subject
 269 to a two-year proprietary period, with immediate ac-
 270 cess granted exclusively to LSST data rights holders (R.
 271 Blum & the Rubin Operations Team 2020). Data rights
 272 holders⁸³ are individuals or institutions with formal au-
 273 thorization to access proprietary data collected by the
 274 Vera C. Rubin Observatory. After the two-year propri-
 275 etary period, **DP1** will be made public. However, even
 276 once the data become public, access for non-data rights
 277 holders will not be provided through Rubin Data Access
 278 Centers in the US and Chile (R. Blum & the Rubin Op-

279 **erations Team 2020**). Alternative access mechanisms are
 280 still under discussion and have not yet been finalized.

281 In this paper, we present the contents and validation
 282 of, and the data access and community support ser-
 283 vices for, Rubin **DP1**, the first Data Preview to deliver
 284 data derived from observations conducted by the Vera
 285 C. Rubin Observatory. **DP1** is based on the reprocess-
 286 ing of 1792 science-grade exposures acquired during the
 287 first on-sky commissioning campaign conducted in late
 288 2024. It covers a total area of approximately $\sim 15 \text{ deg}^2$
 289 distributed across seven distinct non-contiguous fields.
 290 The data products include raw and calibrated single-
 291 epoch images, coadded images, difference images, de-
 292 tection catalogs, and other derived data products. **DP1**
 293 is about 3.5 TB in size and contains around 2.3 million
 294 distinct astronomical objects, detected in 2644 coadded
 295 images. Full **DP1** release documentation is available at
 296 <https://dp1.lsst.io>. Despite Rubin Observatory still be-
 297 ing in commissioning and not yet complete at the time
 298 the observations were acquired, Rubin **DP1** provides an
 299 important first look at the data, showcasing its char-
 300 acteristics and capabilities.

301 The structure of this paper is as follows. In section
 302 2 we describe the observatory system and overall con-
 303 struction and commissioning status at the time of data
 304 acquisition, the seven fields included in **DP1**, and the
 305 observing strategy used. Section 3 summarizes the con-
 306 tents of **DP1** and the data products contained in the
 307 release. The data processing pipelines are described in
 308 section 4, followed by a description of the data valida-
 309 tion and performance assessment in section 5. Section
 310 6 describes the Rubin **Science Platform** (RSP), a cloud-
 311 based data science infrastructure that provides tools and
 312 services to Rubin data rights holders to access, visual-
 313 ize and analyze peta-scale data generated by the **LSST**.
 314 Section 7 presents the Rubin Observatory’s model for
 315 community support, which emphasizes self-help via doc-
 316 umentation and tutorials, and employs an open platform
 317 for issue reporting that enables crowd-sourced solutions.
 318 Finally, a summary of the **DP1** release and information
 319 on expected future releases of data is given in section 8.
 320 The appendix contains a useful glossary of terms used
 321 throughout this paper.

322 All magnitudes quoted are in the AB system (J. B.
 323 Oke & J. E. Gunn 1983), unless otherwise specified.

2. ON-SKY COMMISSIONING CAMPAIGN

324 The first Rubin on-sky commissioning campaign was
 325 conducted using the **LSSTComCam**. The campaign’s
 326 primary objective was to optically align the Simonyi
 327 Survey Telescope and verify its ability to deliver accept-
 328 able image quality using **LSSTComCam**. In addition,
 329

⁸¹ Shared risk means early access with caveats: the community benefits from getting a head start on science, preparing analyses, and providing feedback, while also accepting that the system may not work as well as it will during full operations.

⁸² See <https://dp0.lsst.io>

⁸³ See <https://www.lsst.org/scientists/international-drh-list>

330 the campaign provided valuable operations experience
 331 to facilitate commissioning the full **LSSTCam** (T. Lange
 332 et al. 2024; A. Roodman et al. 2024). We note that
 333 commissioning **LSSTComCam** was not an objective of
 334 the campaign. Instead, **LSSTComCam** was used as a tool
 335 to support broader observatory commissioning, in-
 336 cluding early testing of the **Active Optics System (AOS)**
 337 and the LSST Science Pipelines. As a result, many arti-
 338 facts present in the data are specific to **LSSTComCam**
 339 and will be addressed only if they persist with **LSST-
 340 Cam**. Accordingly, the image quality achieved during
 341 this campaign, and in the **DP1** data, do not reflect the
 342 performance ultimately expected from **LSSTCam**.

343 Approximately 16,000 exposures were collected during
 344 this campaign across all six filters, spanning a wide range
 345 of observing conditions, airmass, and stellar densities.
 346 The majority were obtained in support of **AOS** com-
 347 missioning, system-level verification, and end-to-end testing
 348 of the telescope’s hardware and software. This included
 349 over 10000 exposures for **AOS** commissioning, more than
 350 2000 bias and dark calibration frames, and over 2000 ex-
 351 posures dedicated to commissioning the LSST Science
 352 Pipelines.

353 For **DP1**, we selected a subset of 1792 science-grade
 354 exposures from this campaign, covering seven non-
 355 contiguous fields. These fields were deliberately chosen
 356 to sample a range of stellar densities, overlap with ex-
 357 ternal reference datasets, and span the full breadth of
 358 the four primary LSST science themes in order to enable
 359 the maximum of early science

360 At the time of the campaign, the observatory was
 361 still under construction, with several key components,
 362 such as dome thermal control, full mirror control, and
 363 the final **AOS** configuration either incomplete or still
 364 undergoing commissioning. As a result, image qual-
 365 ity varied widely throughout the campaign and exhib-
 366 ited a broader distribution than is expected with **LSST-
 367 Cam**. Despite these limitations, the campaign suc-
 368 cessfully demonstrated system integration and established a
 369 functional observatory.

370 2.1. Simonyi Survey Telescope

371 The Simonyi Survey Telescope (B. Stalder et al. 2024)
 372 features a unique three-mirror design, including an 8.4-
 373 meter **Primary Mirror Tertiary Mirror (M1M3)** fabri-
 374 cated from a single substrate, and a 3.5-meter **Secondary
 375 Mirror (M2)**. This compact **configuration** supports a
 376 wide 3.5-degree field of view while enabling exceptional
 377 stability, allowing the telescope to slew and settle in under
 378 five seconds. To achieve the scientific goals of the
 379 10-year **LSST**, the Observatory must maintain high im-
 380 age quality across its wide field of view (Ž. Ivezić et al.

381 2019b). This is accomplished through the **AOS** (B. Xin
 382 et al. 2015; G. Megias Homar et al. 2024), which cor-
 383 rects, between successive exposures, wavefront distor-
 384 tions caused by optical misalignments and mirror surface
 385 deformations, primarily due to the effect of gravitational
 386 and thermal loads.

387 The **AOS**, which comprises an open-loop component
 388 and a closed-loop component, optimizes image qual-
 389 ity by aligning the camera and **M2** relative to **M1M3**,
 390 as well as adjusting the shapes of all three mirrors
 391 to nanometer precision. The **AOS** open-loop compo-
 392 nent corrects for predictable distortions and misalign-
 393 ments, while the closed-loop component addresses un-
 394 predictable or slowly varying aberrations using feed-
 395 back from the corner wavefront sensors. The closed-
 396 loop wavefront sensing technique is curvature wavefront
 397 sensing, which infers wavefront errors in the optical sys-
 398 tem by analyzing extra- and intra-focal star images (S.
 399 Thomas et al. 2023). Since **LSSTComCam** lacks dedi-
 400 cated wavefront sensors, wavefront errors were instead
 401 estimated by defocusing the telescope ± 1.5 mm on ei-
 402 ther side of focus and applying the curvature wavefront
 403 sensing pipeline to the resulting images. Each night be-
 404 gan with an initial alignment correction using a laser
 405 tracker to position the system within the capture range
 406 of the closed-loop **algorithm** (G. Megias Homar et al.
 407 2024). Once this coarse alignment was complete, the
 408 **AOS** refined the optical alignment and applied mirror
 409 surfaces corrections to optimize the image quality across
 410 the **LSSTComCam** field of view.

411 During LSST Science Pipelines commissioning (§2.4),
 412 observations were conducted using the **AOS** in open-
 413 loop mode only, without closed-loop corrections between
 414 exposures. Closed-loop operation, which requires ad-
 415 ditional intra- and extra-focal images with **LSSTCom-
 416 Cam**, was not compatible with the continuous data ac-
 417 quisition needed by the pipelines. The image quality
 418 for these data was monitored by measuring the **Point
 419 Spread Function (PSF) Full Width at Half-Maximum
 420 (FWHM)**, and closed-loop sequences were periodically
 421 run when image quality degradation was observed.

422 2.2. The LSST Commissioning Camera

423 **LSSTComCam** (B. Stalder et al. 2022, 2020; J.
 424 Howard et al. 2018; SLAC National Accelerator Lab-
 425 oratory & NSF-DOE Vera C. Rubin Observatory 2024)
 426 is a 144-megapixel version of the 3.2-gigapixel **LSST-
 427 Cam**. It covers approximately 5% of the **LSSTCam** focal
 428 plane area, with a field of view of ~ 0.5 deg 2 (40'x40'),
 429 compared to **LSSTCam**’s 9.6 deg 2 . It was developed to
 430 validate camera interfaces with other observatory com-
 431 ponents and evaluate overall system performance prior

432 to the start of **LSSTCam** commissioning. Although it
 433 has a smaller imaging area, **LSSTComCam** shares the
 434 same plate scale of $0''.2$ per pixel and is housed in a sup-
 435 port structure that precisely replicates the total mass,
 436 center of gravity, and physical dimensions of **LSSTCam**.
 437 All mechanical and utility interfaces to the telescope are
 438 implemented identically, enabling full end-to-end test-
 439 ing of observatory systems, including readout electron-
 440 ics, image acquisition, and data pipelines.

441 The **LSSTCam** focal plane is composed of 25 modular
 442 rafts arranged in a 5×5 grid; 21 rafts are dedicated to
 443 science imaging, while four corner rafts are used for guid-
 444 ing and wavefront sensing. Each science raft is a self-
 445 contained unit comprising nine $4K \times 4K$ Charge-Coupled
 446 Device (CCD) (G. E. Smith 2010) sensors arranged in a
 447 3×3 mosaic, complete with integrated readout electron-
 448 ics and cooling systems. Each sensor is subdivided into
 449 16 segments arranged in a 2×8 layout, with each seg-
 450 ment consisting of 512×2048 pixels and read out in par-
 451 allel using individual amplifiers. **LSSTCam** uses CCD
 452 sensors from two vendors: Imaging Technology Labora-
 453 tory, University of Arizona (UA)) (ITL) and Teledyne
 454 (E2V). To maintain uniform performance and calibra-
 455 tion each raft is populated with sensors from only one
 456 vendor.

457 **LSSTComCam** consists of a single science raft
 458 equipped exclusively with ITL sensors. It is designated
 459 as Raft 22 (R22). Figure 1 shows the **LSSTComCam** fo-
 460 cal plane layout illustrating the placement and number-
 461 ing scheme of sensors (S) and amplifiers (C) within Raft
 462 22 (R22). The sensors selected for **LSSTComCam** rep-
 463 resent the best performing of the remaining ITL devices
 464 after the **LSSTCam** rafts were fully populated. Some
 465 sensors exhibit known issues such as elevated readout
 466 noise (e.g., Detector 8, S22) and increased Charge Trans-
 467 fer Inefficiency (CTI) (e.g., Detector 5, S12).

468 As a result, certain image artifacts present in the DP1
 469 dataset may be specific to **LSSTComCam**. Although
 470 the cryostat in **LSSTComCam**, uses a different cooling
 471 system than that of **LSSTCam**, **LSSTComCam** incorpo-
 472 rated a refrigeration pathfinder to validate the cryogenic
 473 refrigeration system intended for **LSSTCam**. Figure 2
 474 shows the single-raft **LSSTComCam** positioned at the
 475 center of the full **LSSTCam** focal plane, correspond-
 476 ing to the central science raft position.

477 The **LSSTCam** and **LSSTComCam** focal planes are
 478 described in detail in A. A. Plazas Malagón et al. (2025).

2.2.1. Filter Complement

482 **LSSTComCam** supports imaging with six broadband
 483 filters *ugrizy* spanning 320–1050 nm, identical in de-
 484 sign to **LSSTCam**. Whereas the **LSSTCam** filter ex-

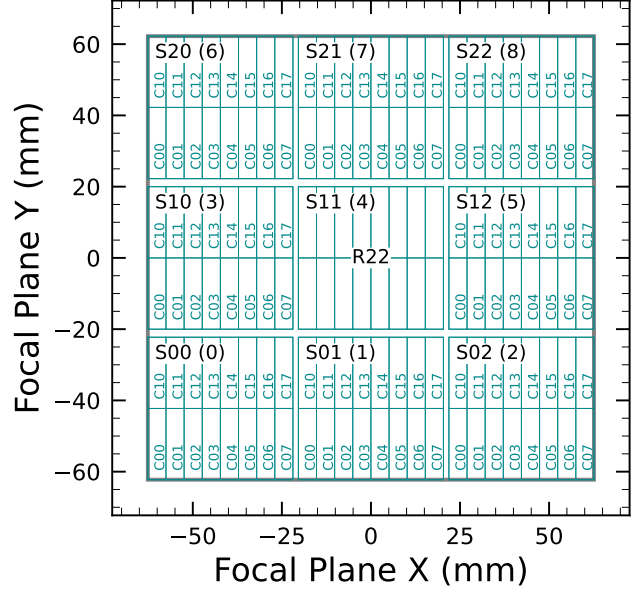


Figure 1. **LSSTComCam** focal plane layout illustrating the placement and numbering scheme of sensors (S) and amplifiers (C). The view is looking down from above the focal plane through the **LSSTComCam** lenses. Each sensor contains 16 amplifiers, and a group of nine sensors comprises one raft. **LSSTComCam** is Raft 22 (R22). The detector number for each sensor is shown in parentheses.

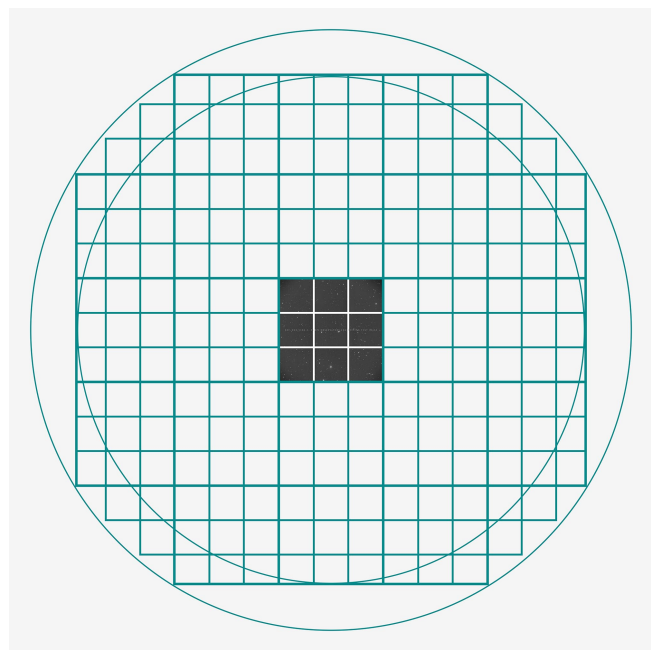


Figure 2. Schematic showing the single-raft **LSSTComCam** positioned at the center of the full **LSSTCam** focal plane. The perspective is from above, looking down through the **LSSTComCam** lenses onto the focal plane. Credit: RubinObs/NOIRLab/SLAC/NSF/DOE/AURA.

485 changer holds five filters, the LSSTComCam exchanger
 486 holds only three at a time. The full-system throughput
 487 of the six LSSTComCam filters, which encompasses contribu-
 488 tions from a standard atmosphere at airmass 1.2, telescope
 489 optics, camera surfaces, and the mean ITL detector
 490 quantum efficiency is shown in Figure 3. The cor-
 491 responding transmission curves are provided as a DP1
 492 data product and are described in §3.6.1

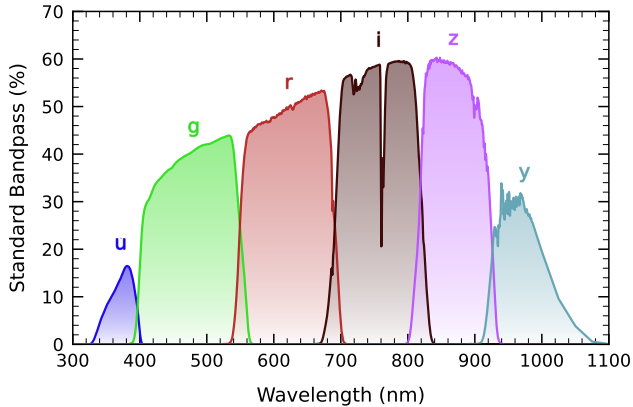


Figure 3. LSSTComCam standard bandpasses, illustrating full system throughput. The bandpasses include a standard atmosphere at airmass 1.2, telescope optics, camera surfaces, and mean ITL detector quantum efficiency.

2.2.2. Timing Calibration

493 The absolute time accuracy of data taken with **LSST-
 494 ComCam** relies on the Network Time Protocol (NTP)
 495 for clock synchronization, which should be accurate
 496 to approximately 1 millisecond. In order to evaluate
 497 the absolute timing accuracy of the entire system we
 498 observed the geosynchronous satellite EUTELSAT 117
 499 West B with a set of 10 usable 10-second exposures over
 500 two nights. EUTELSAT 117 West B is part the GPS
 501 system and serves as one of the WAAS (Wide Area Aug-
 502 mentation System) satellites operated for the U.S. Fed-
 503 eral Aviation Administration (FAA) and used to broad-
 504 cast GPS corrections to air traffic.

505 As these satellites are part of the GPS system, their
 506 positions are tracked very precisely and the record of
 507 their locations is published after the fact and can be
 508 downloaded. Following the technique previously em-
 509 ployed by other surveys, (J. L. Tonry et al. 2018), we
 510 observed the satellite while tracking the sky and then
 511 downloaded the data-files with its precise locations from
 512 the National Satellite Test Bed web site⁸⁴. By compar-
 513 ing the measured and predicted locations of the start of

514 the satellite track on the sky, we determined that (rela-
 515 tive to the start of integration-time recorded in the FITS
 516 headers) our time was accurate to 53.6 ± 11.0 millisec-
 517 onds.

518 This work continues to be an area of ongoing study, as
 519 the exact timing of when the shutter open command is
 520 issued, and the complete profile of the shutter movement
 521 are not yet determined. However the open command
 522 is on average near 29 milliseconds later. Incorporating
 523 the delays into the fit reduces the offset to 24.8 ± 11.0
 524 milliseconds.

525 The full shutter takes approximately 396 milliseconds
 526 to completely open. As the **LSSTComCam** sensors are
 527 centered in the aperture, the center of the focal plane
 528 should be exposed about half-way through the shutter
 529 open procedure, 198 milliseconds after the open com-
 530 mand. There are uncertainties on the full motion pro-
 531 file, and the blade direction motions are currently not
 532 known, but the fraction of the shutter aperture sub-
 533 tended by the focal plane is 52%. This implies that the
 534 shutter will pass any pixel between 198 ± 103 millisec-
 535 onds. Subtracting this from the fitted delay of 24.8 mil-
 536 liseconds and adding the fitted error of 11.0 millisec-
 537 onds in quadrature, results in a current conservative esti-
 538 mate of the delay of -173.2 ± 104.1 milliseconds, consist-
 539 ent with and smaller than the constraints on the timing off-
 540 set determined using astrometric residuals from known
 541 asteroid associations presented in §5.10.2.

2.3. Flat Field System

542 During the on-sky campaign, key components of the
 543 Rubin calibration system (P. Ingraham et al. 2022),
 544 including the flat field screen, had not yet been in-
 545 stalled. As a result, flat fielding for DP1 relied en-
 546 tirely on twilight flats. While twilight flats pose chal-
 547 lenges such as non-uniform illumination and star print-
 548 through, they were the only available option during
 549 **LSSTComCam** commissioning and for DP1 processing.
 550 To mitigate these limitations, dithered, tracked expo-
 551 surees were taken over a broad range of azimuth and rota-
 552 tor angles to construct combined flat calibration frames.
 553 Exposure times were dynamically adjusted to reach tar-
 554 get signal levels of between 10,000 and 20,000 electrons.
 555 Future campaigns with LSSTCam will benefit from more
 556 stable and uniform flat fielding using the Rubin flat field
 557 system, described in P. Fagrelius & E. S. Rykoff (2025).

2.4. LSST Science Pipelines Commissioning

560 Commissioning of the LSST Science Pipelines, (Rubin
 561 Observatory Science Pipelines Developers 2025), began
 562 once the telescope was able to routinely deliver sub-
 563 arcsecond image quality. The goals included testing the

⁸⁴ <https://www.nstb.tc.faa.gov/nstarchive.html>

internal astrometric and photometric calibration across a range of observing conditions, validating the difference image analysis and Prompt Processing (K.-T. Lim 2023) framework, and accumulating over 200 visits per band to evaluate deep coadded images with integrated exposure times roughly equivalent to those of the planned LSST Wide Fast Deep (WFD) 10-year depth. To support these goals, seven target fields were selected that span a range of stellar densities, overlap with external reference datasets, and collectively span the full breadth of the four primary LSST science themes. These seven fields form the basis of the DP1 dataset. Figure 4 shows the locations of these seven fields on the sky, overlaid on the LSST baseline survey footprint (R. L. Jones et al. 2021; P. Yoachim 2022; Rubin’s Survey Cadence Optimization Committee et al. 2022, 2023, 2025), along with sky coverage of both the LSSTCam and LSSTComCam focal planes.

Each of the seven target fields was observed repeatedly in multiple bands over many nights. A typical observing epoch on a given target field consisted of 5-20 visits in each of the three loaded filters (§2.2.1). All DP1 images were captured as single 1×30 -second exposures for all bands, rather than as 2×15 -second “snap” exposures. Additionally, some u -band exposures were taken as 38-second exposures. The exposure time for LSST images will be determined following further testing during the commissioning phase with LSSTCam. All images were acquired using the Rubin Feature-Based Scheduler (FBS), version 3.0 (E. Naghib et al. 2019; P. Yoachim et al. 2024). Table 1 lists the seven DP1 fields and their pointing centers, and provides a summary of the band coverage in each.

The temporal sampling distribution of observations per band and per night is shown in Figure 5. Gaps in coverage across some bands arise from the fact that LSSTComCam can only hold three filters at a time (see §2.2.1). As the campaign progressed, the temporal sampling became denser across all fields, reflecting improved efficiency and increased time allocated for science observations.

It is important to note that the time sampling in the DP1 dataset differs significantly from that of LSST survey cadence. Table 2 reports the 5σ point source depths for coadded images per field and per band, where coverage in a band is non-zero, together with the expected 10-year LSST depths derived from the baseline simulated survey (F. B. Bianco et al. 2022).

All fields except for the low ecliptic latitude field, Rubin_SV_38_7, used a small random dithering pattern. The random translational dithers of the telescope boresight were applied for each visit, with offsets of up to

0.2 degrees around the pointing center (Table 1). The rotational dithers of the camera rotator were typically approximately 1 degree per visit, with larger random offsets at each filter change, which worked to keep operational efficiency high. The Rubin_SV_38_7 field used a different dither pattern to optimize coverage of Solar System Objects and test Solar System Object linking across multiple nights. These observations used a 2×2 grid of LSSTComCam pointings to cover an area of about 1.3 degree \times 1.3 degrees. The visits cycled between the grid’s four pointing centers, using small random translational dithers to fill chip gaps with the goal of acquiring 3-4 visits per pointing center per band in each observing epoch.

2.5. Delivered Image Quality

The delivered image quality is influenced by contributions from both the observing system (i.e., dome, telescope and camera) and the atmosphere. During the campaign, the Rubin Differential Image Motion Monitor (DIMM) was not operational, so atmospheric seeing was estimated using live data from the Southern Astrophysical Research Telescope (SOAR) Ring-Image Next Generation Scintillation Sensor (RINGSS) seeing monitor, also located on Cerro Pachón. Although accelerometers mounted on the mirror cell and top-end assembly were available to track dynamic optics effects, such as mirror oscillations that can degrade optical alignment, this data was not used during the campaign. Mount encoder data were used to measure the mount jitter in every image, with a measured median contribution of 0.004 arcseconds to image degradation. As the pointing model was not fine-tuned, tracking errors could range from 0.2 to 0.4 arcseconds per image, depending on RA and Dec. Dome and mirror-induced seeing were not measured during the campaign.

The DP1 median delivered image quality, quantified as the PSF FWHM across all bands, is $1.^{\prime\prime}14$, with the best images achieving approximately $0.^{\prime\prime}58$. It varies both by passband and target field. The per-band median PSF FWHM values are: $u = 1.^{\prime\prime}39$, $g = 1.^{\prime\prime}25$, $r = 1.^{\prime\prime}11$, $i = 0.^{\prime\prime}965$, $z = 1.^{\prime\prime}15$, $y = 0.^{\prime\prime}856$ arcsecs. Figure 7 shows the distribution of PSF FWHM (arcsec) over all 16071 individual sensors images.

Ongoing efforts aim to quantify all sources of image degradation, including contributions from the camera system, static and dynamic optical components, telescope mount motion, observatory-induced seeing from the dome and mirror, and atmospheric conditions.

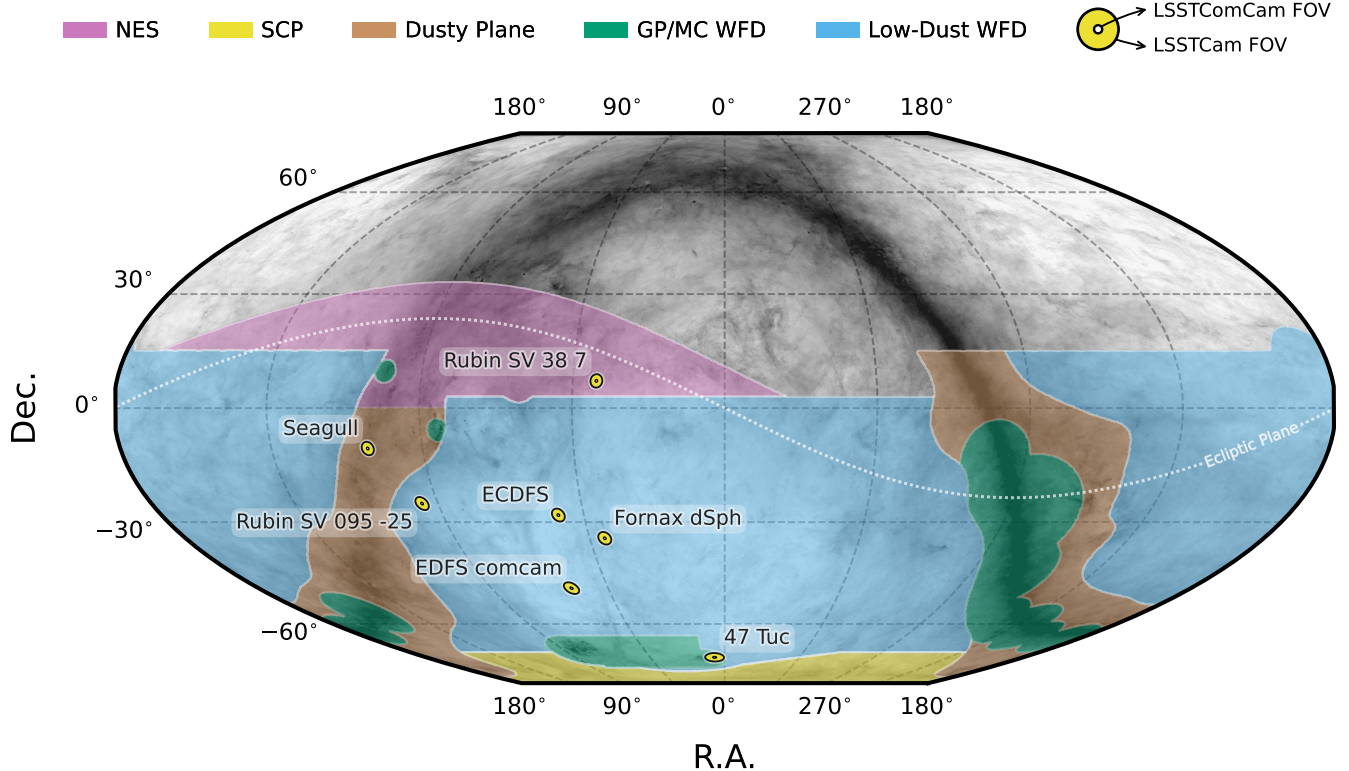


Figure 4. Locations of the seven DP1 fields overlaid on the LSST baseline survey footprint (Rubin’s Survey Cadence Optimization Committee et al. 2025). NES: North Ecliptic Spur, SCP: South Celestial Pole, Low-Dust WFD: regions away from the Galactic Plane (GP) observed with a WFD cadence, GP/MC WFD: Galactic Plane and Magellanic Clouds regions observed with a WFD cadence. The fields of view covered by the LSSTCam and LSSTComCam focal planes are represented as outer and inner concentric circles, respectively, centered on the pointing center of each field.

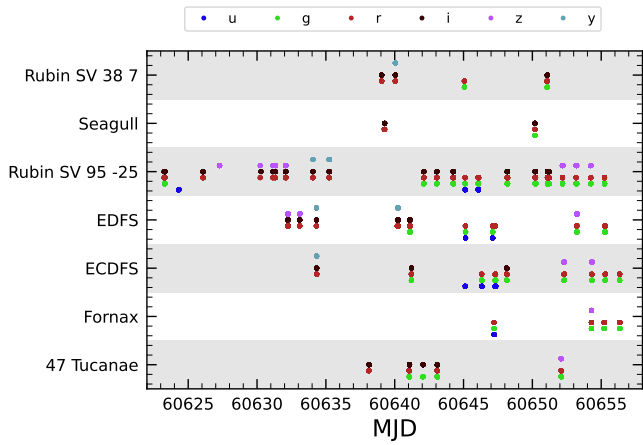


Figure 5. Distribution of DP1 observations by date grouped by field as a function of time over the 48 nights of data taking with LSSTComCam. Each dot represents a single exposure, color-coded by band.

3. OVERVIEW OF THE CONTENTS OF RUBIN DP1

669 Here we describe Rubin DP1 data products and pro-
 670 vide summary statistics for each. The DP1 science data
 671 products are derived from the 15972 individual CCD
 672 images taken across 1792 exposures in the seven LSST-
 673 ComCam commissioning fields (§2.4).

674 The data products that comprise DP1 provide an early
 675 preview of future LSST data releases and are strongly
 676 dependent on the type and quality of the data that was
 677 collected during LSSTComCam on-sky campaign (§2.4).
 678 Consequently not all anticipated LSST data products,
 679 as described in the Data Product Definition Document
 680 (DPDD) (M. Jurić et al. 2023) were produced for the
 681 DP1 dataset.

682 Rubin Observatory has adopted the convention by
 683 which single-epoch detections are referred to as Sources.
 684 By contrast, the astrophysical object associated with a

Table 1. DP1 fields and pointing centers with the number of exposures in each band per field. ICRS coordinates are in units of decimal degrees, and are specified as J2000.

Field Code	Field Name	RA	DEC	Band						Total	
				deg	deg	u	g	r	i	z	
47_Tuc	47 Tucanae Globular Cluster	6.128	-72.090	6	10	32	19	0	5		72
ECDFS	Extended Chandra Deep Field South	53.160	-28.100	43	230	237	162	153	30		855
EDFS_comcam	Rubin SV Euclid Deep Field South	59.150	-48.730	20	61	87	42	42	20		272
Fornax_dSph	Fornax Dwarf Spheroidal Galaxy	40.080	-34.450	0	5	25	12	0	0		42
Rubin_SV_095_-25	Rubin SV Low Galactic Latitude Field	95.040	-25.000	33	82	84	23	60	10		292
Rubin_SV_38_7	Rubin SV Low Ecliptic Latitude Field	37.980	7.015	0	44	40	55	20	0		159
Seagull	Seagull Nebula	106.300	-10.510	10	37	43	0	10	0		100
Total				112	469	548	313	285	65		1792

Table 2. DP1 median 5 σ coadded point-source detection limits per field and band, along with the expected 10-year LSST values derived from the baseline simulated survey (F. B. Bianco et al. 2022).

Field Code	Band					
	u	g	r	i	z	y
47_Tuc	-	24.03	24.24	23.90	-	21.79
ECDFS	24.55	26.18	25.96	25.71	25.07	23.10
EDFS_comcam	23.42	25.77	25.72	25.17	24.47	23.14
Fornax_dSph	-	24.53	25.07	24.64	-	-
Rubin_SV_095_-25	24.29	25.46	24.95	24.86	24.32	22.68
Rubin_SV_38_7	-	25.46	25.15	24.86	23.52	-
Seagull	23.51	24.72	24.19	-	23.30	-
LSST 10-year	25.73	26.86	26.88	26.34	25.63	24.87

given detection is referred to as an Object⁸⁵. As such, a given Object will likely have multiple associated Sources, since it will be observed in multiple epochs.

At the highest level, the DP1 data products fall into one of five types:

- **Images**, including single-epoch images, deep and template coadded images, and difference images;
- **Catalogs** of astrophysical Sources and Objects detected and measured in the aforementioned images. We also provide the astrometric and photometric reference catalog generated from external

⁸⁵ We caution that this nomenclature is not universal; for example, some surveys call “detections” what we call “sources”, and use the term “sources” for what we call “objects”.

sources that was used during processing to generate the DP1 data products;

- **Maps**, which provide non-science-level visualizations of the data within the release. They include, for example, zoomable multi-band images and coverage maps;
- **Ancillary data products**, including, for example, the parameters used to configure the data processing pipelines, log and processing performance files, and **calibration** data products (e.g., **CTI** models, brighter-fatter kernels, etc.);
- **Metadata** in the form of tables containing information about each visit and processed image, such as pointing, exposure time, and a range of image quality summary statistics.

While images and catalogs are expected to be the primary data products for scientific research, we also recognize the value of providing access to other data types to support investigations and ensure transparency.

To facilitate processing, Rubin DP1 uses a single skymap⁸⁶ that covers the entire sky area encompassing the seven DP1 fields. The DP1 skymap divides the entire celestial sphere into 18938 **tracts**, each covering approximately 2.8 deg². Each **tract** is further subdivided into 10 **times10** equally-sized patches, with each **patch** covering roughly 0.028 deg². Both tracts and patches overlap with their neighboring regions. Since the LSST-ComCam only observed \sim 15 deg² of the sky during its campaign, only 29 out of the 18938 tracts have cover-

⁸⁶ A skymap is a tiling of the celestial sphere, organizing large-scale sky coverage into manageable sections for processing and analysis.

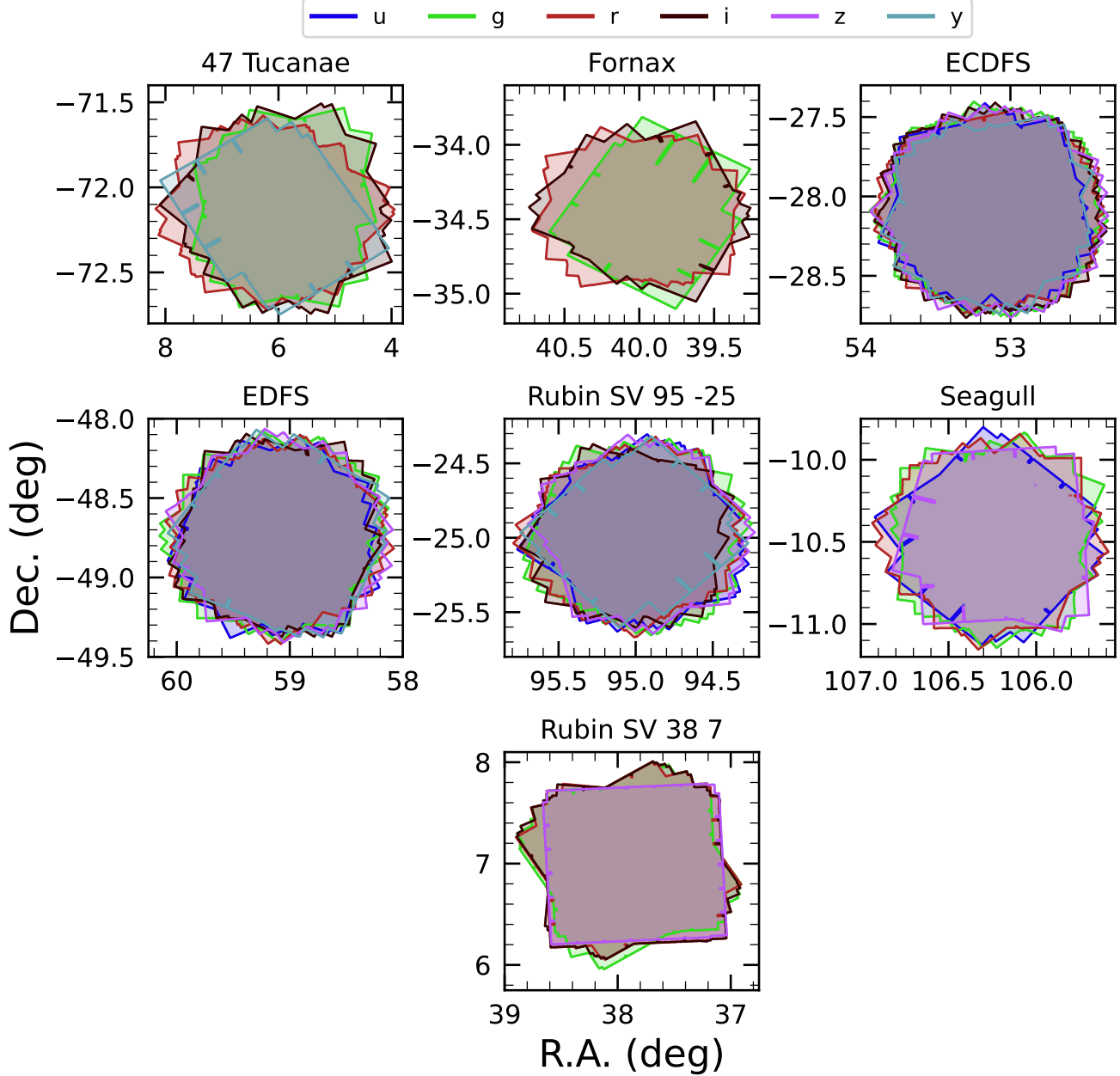


Figure 6. Sky coverage maps showing the distribution of visits in each field, color coded by band. The images clearly show the focal plane chip gaps and dithering pattern. Only the detectors for which single frame processing succeeded are included in the plots, which explains why the central region of 47_Tuc looks thinner than the other fields.

age in DP1. The tract identification numbers and corresponding target names for these tracts are listed in Table 3. The size of a tract is larger than the LSSTCam field of view; however, since each observed field extends across more than one tract, each field covers multiple tracts.

The skymap is integral to the production of co-added images. To create a coadded image, the processing pipeline selects all calibrated science images in a given

field that meet specific quality thresholds (§3.1 and §4.5.1) for a given `patch`, warps them onto a single consistent pixel grid for that `patch`, as defined by the skymap, then coadds them. Each individual coadd image therefore covers a single `patch`. Coadded images and the catalogs of detections from them are termed `tract`-level data products. By contrast, visit-level data products are those derived from individual LSSTComCam exposures, such as a raw image or a catalog of detections

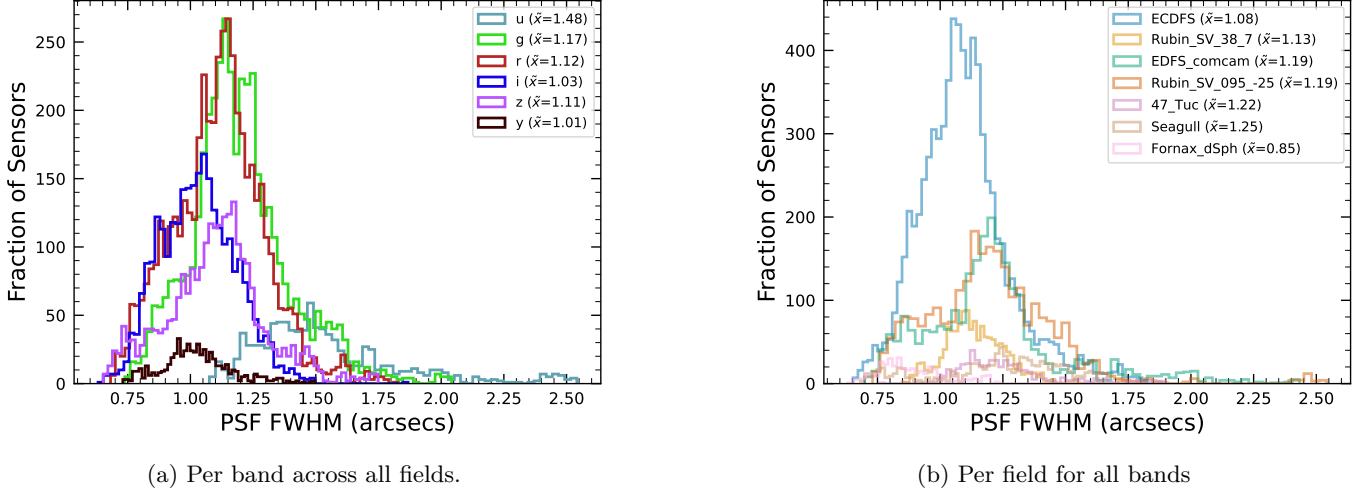


Figure 7. Histograms showing the distribution of PSF FWHM for all 16071 single-epoch individual sensors in the DP1 dataset. The median values are given in the legend.

Table 3. Tract coverage of each DP1 field. The size of a tract is larger than the LSSTCam field of view; however, since each observed field extends across more than one tract, each field covers multiple tracts.

Field Code	Tract ID
47_Tuc	453, 454
ECDFS	4848, 4849, 5062, 5063, 5064
EDFS_comcam	2234, 2235, 2393, 2394
Fornax_dSph	4016, 4017, 4217, 4218
Rubin_SV_095_-25	5305, 5306, 5525, 5526
Rubin_SV_38_7	10221, 10222, 10463, 10464, 10704, 10705
Seagull	7610, 7611, 7849, 7850

763 the Data Butler, but the names used in the IVOA Services
764 differ only slightly in that they are prepended by
765 “lsst.”.

766 • **raw** images (NSF-DOE Vera C. Rubin Observatory 2025b) are unprocessed data received directly
767 from the camera. Each **raw** corresponds to a single CCD from a single LSSTComCam exposure of
768 30 s duration. Each LSSTComCam exposure typically produces up to nine **raws**, one per sensor in
769 the focal plane. However, a small number of exposures resulted in fewer than nine **raw** images due
770 to temporary hardware issues or readout faults.

771 In total, DP1 includes 16125 **raw** images. Table 4 provides a summary by target and band. A
772 **raw** contains 4608×4096 pixels, including prescan and overscan, and occupies around 18 MB of
773 disk space.⁸⁷ The field of view of a single **raw**, excluding prescan and overscan regions, is roughly
774 $0.23 \times 0.22 \approx 0.051 \text{ deg}^2$, corresponding to a plate
775 scale of $0''.2$ per pixel.

776 • **visit_images** (NSF-DOE Vera C. Rubin Observatory 2025c) are fully-calibrated processed images.
777 They have undergone instrument signature removal (§4.2.1) and all the single frame processing
778 steps described in §4.2 which are, in summary:
779 **PSF** modeling, **background** subtraction, and astrometric and photometric **calibration**. As with
780 **raws**, a **visit_image** contains processed data from
781

782 ⁸⁷ Each amplifier image contains 3 and 64 columns of serial prescan and overscan pixels, respectively, and 48 rows of parallel overscan pixels, meaning a **raw** contains 4072×4000 exposed pixels.

3.1. Science Images

783 Science images are exposures of the night sky, as distinct from **calibration** images (§3.6.3). Although the release includes **calibration** images, allowing users to reprocess the raw images if needed, this is expected to be necessary only in rare cases. Users are strongly encouraged to start from the visit-level images provided. The data product names shown here are those used by

746 from a single calibrated image. Most science data products (i.e., images and catalogs) in DP1 are either **tract**
747 or **visit**–level, the main exception being the **Calibration**
748 **reference catalog**.

749 Throughout this section, the data product names are
750 indicated using monospace font. Data products are accessed via either the International Virtual Observatory
751 Alliance (IVOA) Services (§6.2.1) or the Data Butler
752 (§6.2.2), or both.

753 **3.1. Science Images**
754
755 Science images are exposures of the night sky, as distinct from **calibration** images (§3.6.3). Although the release includes **calibration** images, allowing users to reprocess the raw images if needed, this is expected to be necessary only in rare cases. Users are strongly encouraged to start from the visit-level images provided. The data product names shown here are those used by

Table 4. Number of `raw` images per field and band. Each `raw` image corresponds to a single 30-second LSSTComCam exposure on one CCD. Most exposures produce nine `raw` images, one per sensor in the focal plane, however some yield fewer due to occasional hardware or readout issues.

Field Code	Band						Total
	<i>u</i>	<i>g</i>	<i>r</i>	<i>i</i>	<i>z</i>	<i>y</i>	
47_Tuc	54	90	288	171	0	45	648
ECDFS	387	2070	2133	1455	1377	270	7692
EDFS_comcam	180	549	783	378	378	180	2448
Fornax_dSph	0	45	225	108	0	0	378
Rubin_SV_095_25	297	738	756	207	540	90	2628
Rubin_SV_38_7	0	396	360	495	180	0	1431
Seagull	90	333	387	0	90	0	900
Total	1008	4221	4932	2814	2565	585	16125

a single `CCD` resulting from a single 30 s `LSST-ComCam` exposure. As a consequence, a single `LSSTComCam` exposure typically results in nine `visit_images`. The handful of exposures with fewer than nine `raw` images also have fewer than nine `visit_images`, but there are an additional 153 `raw` that failed processing and for which there is thus no corresponding `visit_image`. Almost all failures were due to challenges with astrometric fits or `PSF` models in crowded fields.

In total, there are 15972 `visit_images` in `DP1`. Each `visit_image` comprises three images: a calibrated science image, a variance image, and a pixel-level bitmask that flags issues such as saturation, cosmic rays, or other artifacts. Each `visit_image` also contains a position-dependent `PSF` model, `World Coordinate System (WCS)` information, and various `metadata` providing information about the observation and processing. The science and variance images and the pixel mask each contain 4072×4000 pixels. In total, a single `visit_image`, including all extensions and `metadata`, occupies around 110 MB of disk space.

- `deep_coadds` ([NSF-DOE Vera C. Rubin Observatory 2025d](#)) are the product of warping and co-adding multiple `visit_images` covering a given `patch`, as defined by the skymap. `deep_coadds` are created on a per-band basis, meaning only data from exposures taken with a common filter are coadded. As such, there are up to six `deep_coadds` covering each `patch` – one for each of the six `LSSTComCam` bands. The process of produc-

ing `deep_coadds` is described in detail in [§4.5](#) but, to summarize, it involves the selection of suitable `visit_images` (both in terms of `patch` coverage, band, and image quality), the warping of those `visit_images` onto a common pixel grid, and the co-adding of the warped `visit_images`. To be included in a `DP1` `deep_coadd`, a `visit_image` needed to have a `PSF FWHM` smaller than $1''.7$. Of the 15972 `visit_images`, 15375 satisfied this criterion and were therefore used to create `deep_coadds`.

There are a total of 2644 `deep_coadds` in `DP1`. As mentioned above, a single `deep_coadd` covers one `patch`, and includes a small amount of overlap with its neighboring `patch`. The skymap used for `DP1` defines a `patch` as having an on-sky area of 0.028 deg^2 excluding overlap, and 0.036 deg^2 including overlap. A single `deep_coadd` – including overlap – contains 3400×3400 equal-sized pixels, corresponding to a platescale of $0''.2$ per pixel. Each `deep_coadd` contains the science image (i.e., the coadd), a variance image, and a pixel mask; all three contain the same number of pixels. Each `deep_coadd` also contains a position-dependent `PSF` model (which is the weighted sum of the `PSF` models of the input `visit_images`), `WCS` information, plus various `metadata`.

Since coadds always cover an entire `patch`, it is common for a `deep_coadd` to contain regions that were not covered by any of the selected `visit_images`, particularly if the `patch` is on the outskirts of a field and was thus not fully observed. By the nature of how coadds are produced, such regions may contain seemingly valid `flux` values (i.e., not necessarily zeros or `NaNs`), but will instead be flagged with the `NO_DATA` flag in the pixel mask. It is therefore crucial that the pixel mask be referred to when analyzing `deep_coadds`.

- `template_coadds` ([NSF-DOE Vera C. Rubin Observatory 2025e](#)) are those created to use as templates for difference imaging, i.e., the process of subtracting a template image from a `visit_image` to identify either variable or `transient` objects.⁸⁸ As with `deep_coadds`, `template_coadds` are pro-

⁸⁸ It should be noted that `template_coadds` are not themselves subtracted from `visit_images` but are, instead, warped to match the `WCS` of a `visit_image`. It is this warped template that is subtracted from the `visit_image` to create a difference image. For storage space reasons, warped templates are not retained for `DP1`, as they can be readily and reliably recreated from the `template_coadds`.

duced by warping and co-adding multiple `visit_images` covering a given skymap-defined `patch`. The process of building `template_coadds` is the same as that for `deep_coadds`, but the selection criteria differ between the two types of coadd. In the case of `template_coadds`, one third of `visit_images` covering the `patch` in question with the narrowest `PSF FWHM` are selected. If one third corresponds to fewer than twelve `visit_images` (i.e., there are fewer than 36 `visit_images` covering the `patch`), then the twelve `visit_images` with the narrowest `PSF FWHM` are selected. Finally, if there are fewer than twelve `visit_images` covering the `patch`, then all `visit_images` are selected. Of the 15972 `visit_images`, 13113 were used to create `template_coadds`. This selection strategy is designed to optimize for `seeing` when a `patch` is well-covered by `visit_images`, yet still enable the production of `template_coadds` for poorly-covered patches.

DP1 contains a total of 2730 `template_coadds`.⁸⁹ As with `deep_coadds`, a single `template_coadd` covers a single `patch`. Since the same skymap is used when creating both `deep_coadd` and `template_coadds`, the on-sky area and pixel count of `template_coadds` are the same as that of a `deep_coadd` (see above). Similarly, `template_coadds` contain the science image (i.e., the coadd), a variance image, and a pixel mask; all three contain the same number of pixels. Also included are the `PSF` model, `WCS` information, and `metadata`. As is the case for `deep_coadd`, those pixels within `template_coadds` that are not covered by any of the selected `visit_images` may still have seemingly valid values, but are indicated with the `NO_DATA` flag within the pixel mask.

- `difference_images` (NSF-DOE Vera C. Rubin Observatory 2025f) are generated by the subtraction of the warped, scaled, and `PSF`-matched `template_coadd` from the `visit_image` (see §4.6.1). In principle, only those sources whose `flux` has changed relative to the `template_coadd` should be apparent (at a significant level) within a `difference_image`. In practice, however, there are numerous spurious sources present in `difference_images` due to unavoidably imperfect template matching.

⁸⁹ The difference in the number of `deep_coadds` and `template_coadds` is due to the difference in the `visit_image` selection criteria for each coadd.

In total, there are 15972 `difference_images` in DP1, one for each `visit_image`.

Like `visit_images`, `difference_images` contain the science (i.e., difference) image, a variance image, and a pixel mask; all three contain the same number of pixels, which is the same as that of the input `visit_image`. Also included is the `PSF` model, `WCS` information, and `metadata`.

- Background images contain the model `background` that has been generated and removed from a science image. `visit_images`, `deep_coadds` and `template_coadds` all have associated `background` images.⁹⁰ Background images contain the same number of pixels as their respective science image, and there is one `background` image for each `visit_image`, `deep_coadd`, and `template_coadd`. Difference imaging analysis also measures and subtracts a `background` model, but the `difference_background` data product is not written out by default and is not part of DP1.

Background images are not available via the IVOA Service; they can only be accessed via the Butler Data Service.

3.2. Catalogs

Here we describe science-ready tables produced by the science pipelines. All but one of the catalogs described here contain data for detections in the images described in section 3.1, the exception being the `Calibration` catalog, which contains reference data obtained from previous surveys. Observatory-produced `metadata` tables are described in §3.5. Each type of catalog contains measurements for either Sources detected in `visit_images` and `difference_images`, or Objects detected in `deep_coadds`.

While the `Source`, `Object`, `ForcedSource`, `DiaSource`, `DiaObject`, and `ForcedSourceOnDiaObject` catalogs described below each differ in terms of their specific columns, in general they each contain: one or more unique identification numbers, positional information, one or more types of `flux` measurements (e.g., aperture fluxes, `PSF` fluxes, Gaussian fluxes, etc.), and a series of boolean flags (indicating, for example, whether the source/object is affected by saturated pixels, cosmic rays, etc.) for each source/object. The Solar System catalogs `SSObject` and `SSSSource` deviate from this general structure in that they instead contain orbital parameters for all known asteroids. Where applicable, all

⁹⁰ In future data releases, `background` images may be included as part of their respective science image data product.

962 measured properties are reported with their associated
 963 1σ uncertainties.
 964

965 Since [DP1](#) is a preview, it doesn't include all the cat-
 966 alogs expected in a full [LSST Data Release](#). Addi-
 967 tionally, the catalogs it does include may be missing some
 968 columns planned for future releases. Where this is the
 969 case, we note what data are missing in the catalog de-
 970 scriptions that follow.
 971

972 Catalog data are stored in the [Qserv](#) database (§6.5.1)
 973 and are accessible via [Table Access Protocol \(IVOA](#)
 974 [standard\)](#) (IVOA), and an online [DP1](#) catalog schema
 975 is available at <https://sdm-schemas.lsst.io/dp1.html>. Catalog data are also accessible via the Data [Butler](#)
 976 (§6.2.2).
 977

- 978 • The [Source](#) catalog ([NSF-DOE Vera C. Rubin](#)
 979 [Observatory 2025g](#)) contains data on all sources
 980 which are, prior to deblending (§4.5.2), detected
 981 with a greater than 5σ significance in each individ-
 982 ual visit. The detections reported in the [Source](#)
 983 catalog have undergone deblending; in the case of
 984 blended detections, only the deblended sources are
 985 included in the [Source](#) catalog. It is important
 986 to note that while the criterion for inclusion in a
 987 [Source](#) catalog is a $> 5\sigma$ detection in a [visit_im-](#)
 988 [age](#) prior to deblending, the positions and fluxes
 989 are reported post-deblending. Hence, it is possible
 990 for the [Source](#) catalog to contain sources whose
 991 [flux](#)-to-error ratios – potentially of all types (i.e.,
 992 [aperture flux](#), [PSF flux](#), etc.) – are less than 5.
 993

994 In addition to the general information mentioned
 995 above (i.e., IDs, positions, fluxes, flags), the
 996 [Source](#) catalog also includes basic [shape](#) and ex-
 997 tendedness information.
 998

999 The [Source](#) catalog contains data for 46 million
 1000 sources in [DP1](#).
 1001

- 1002 • The [Object](#) catalog ([NSF-DOE Vera C. Rubin](#)
 1003 [Observatory 2025h](#)) contains data on all objects
 1004 detected with a greater than 5σ significance in the
 1005 [deep_coadds](#). With coadd images produced on a
 1006 per-band basis, a $> 5\sigma$ detection in one or more of
 1007 the bands will result in an object being included in
 1008 the [Object](#) catalog. For cases where an object is
 1009 detected at $> 5\sigma$ in more than one band, a cross-
 1010 matching has been performed between bands to
 1011 associate an object in one band with its counter-
 1012 part(s) in the other bands. As such, unlike the
 1013 [Source](#) catalog, the [Object](#) catalog contains data
 1014 from multiple bands. The objects reported in the
 1015 [Object](#) catalog have also undergone deblending; in
 1016 the case of blended detections, only the deblended
 1017 objects are included in the catalog.
 1018

1019 child objects are included in the catalog. As with
 1020 the [Source](#) catalog, the criterion for inclusion in
 1021 the [Object](#) catalog is a $> 5\sigma$ detection in one
 1022 of the [deep_coadds](#) prior to deblending, yet the
 1023 positions and fluxes of objects are reported post-
 1024 deblending. Hence, it is possible for [Object](#) cata-
 1025 log to contain [objects](#) whose [flux](#)-to-error ratios
 1026 — potentially of all types and in all bands — are
 1027 less than 5.
 1028

1029 In addition to the general information mentioned
 1030 above (i.e., IDs, positions, fluxes, flags), the [Ob-](#)
 1031 [ject](#) catalog also includes basic [shape](#) and extend-
 1032 edness information. While they may be included
 1033 in future data releases, no photometric redshifts,
 1034 Petrosian magnitudes (V. Petrosian 1976), proper
 1035 motions or periodicity information are included in
 1036 the [DP1](#) object catalogs.
 1037

1038 The [Object](#) catalog contains data for 2.3 million
 1039 objects in [DP1](#).
 1040

- 1041 • The [ForcedSource](#) catalog ([NSF-DOE Vera C. Rubin](#)
 1042 [Observatory 2025i](#)) contains forced [PSF](#)
 1043 photometry measurements performed on both
 1044 [difference_images](#) (i.e., the [psfDiffFlux](#) col-
 1045 umn) and [visit_images](#) (i.e., the [psfFlux](#) col-
 1046 umn) at the positions of all the objects in the
 1047 [Object](#) catalog, to allow assessment of the time
 1048 variability of the fluxes. We recommend using
 1049 the [psfDiffFlux](#) column when generating light
 1050 curves because this quantity is less sensitive to [flux](#)
 1051 from neighboring sources than [psfFlux](#). In addi-
 1052 tion to forced photometry [PSF](#) fluxes, a number
 1053 of boolean flags are also included in the [Forced-](#)
 1054 [Source](#) catalog.
 1055

1056 The [ForcedSource](#) catalog contains a total of 269
 1057 million entries across 2.3 million unique objects.
 1058

- 1059 • The [DiaSource](#) catalogs ([NSF-DOE Vera C. Rubin](#)
 1060 [Observatory 2025j](#)) contains data on all the
 1061 sources detected at a $> 5\sigma$ significance — includ-
 1062 ing those associated with known Solar System
 1063 objects — in the [difference_images](#). Unlike sources
 1064 detected in [visit_images](#), sources detected in
 1065 difference images (hereafter, “DiaSources”) have
 1066 gone through an association step in which an at-
 1067 tempt has been made to associate them into un-
 1068 derlying objects called “DiaObject”s. The [Dia-](#)
 1069 [Source](#) catalog consolidates all this information
 1070 across multiple visits and bands. The detections
 1071 reported in the [DiaSource](#) catalog have not un-
 1072 dergone deblending.
 1073

1061 The **DiaSource** catalog contains data for 3.1 mil-
 1062 lion **DiaSources** in **DP1**.
 1063

- 1063 The **DiaObject** catalog ([NSF-DOE Vera C. Rubin
 1064 Observatory 2025k](#)) contains the astrophysical ob-
 1065 jects that DiaSources are associated with (i.e., the
 1066 “DiaObjects”). The **DiaObject** catalog contains
 1067 only non-Solar System Objects; Solar System Ob-
 1068 jects are, instead, recorded in the **SSObject** cata-
 1069 log. When a DiaSource is identified, the **DiaOb-
 1070 ject** and **SSObject** catalogs are searched for ob-
 1071 jects to associate it with. If no association is found,
 1072 a new **DiaObject** is created and the **DiaSource** is
 1073 associated to it. Along similar lines, an attempt
 1074 has been made to associate **DiaObjects** across mul-
 1075 tiple bands, meaning the **DiaObject** catalog, like
 1076 the **Object** catalog, contains data from mul-
 1077 tiple bands. Since **DiaObjects** are typically [transient](#)
 1078 or variable (by the nature of their means of
 1079 detection), the **DiaObject** catalog contains sum-
 1080 mary statistics of their fluxes, such as the mean
 1081 and standard deviation over multiple epochs; users
 1082 must refer to the **ForcedSourceOnDiaObject** cat-
 1083 alog (see below) or the **DiaSource** catalog for sin-
 1084 gle [epoch flux](#) measurements of **DiaObjects**.
 1085

1085 The **DIAObject** catalog contains data for 1.1 mil-
 1086 lion **DiaObjects** in **DP1**.
 1087

- 1087 The **ForcedSourceOnDiaObject** catalog ([NSF-
 1088 DOE Vera C. Rubin Observatory 2025l](#)) is equiv-
 1089 alent to the **ForcedSource** catalog, but contains
 1090 [forced photometry](#) measurements obtained at the
 1091 positions of all the **DiaObjects** in the **DiaObject**
 1092 catalog.
 1093

1093 The **ForcedSourceOnDiaObject** catalog contains
 1094 a total of 197 million entries across 1.1 million
 1095 unique **DiaObjects**.
 1096

- 1096 The **CcdVisit** catalog ([NSF-DOE Vera C. Ru-
 1097 bin Observatory 2025m](#)) contains data for each
 1098 individual processed **visit_image**. In addition
 1099 to technical information, such as the on-sky co-
 1100 ordinates of the central pixel and measured pixel
 1101 scale, the **CcdVisit** catalog contains a range of
 1102 data quality measurements, such as whole-image
 1103 summary statistics for the **PSF** size, zeropoint, sky
 1104 [background](#), sky noise, and quality of astrometric
 1105 solution. It provides an efficient method to access
 1106 **visit_image** properties without needing to access
 1107 the image data.
 1108

1108 The **CcdVisit** catalog contains entries summariz-
 1109 ing data for all 16071 **visit_images**.
 1110

- 1110 The **SSObject** catalog ([NSF-DOE Vera C. Rubin
 1111 Observatory 2025n](#)), [Minor Planet Center Orbit
 1112 database \(MPCORB\)](#) and **SSObject**, carry infor-
 1113 mation about solar system objects. The **MPCORB**
 1114 table provides the Minor Planet [Center](#)-computed
 1115 orbital elements for all known asteroids, includ-
 1116 ing those that Rubin discovered. For DP1, the
 1117 **SSObject** catalog serves primarily to provide the
 1118 mapping between the [International Astronomical
 1119 Union \(IAU\)](#) designation of an object (listed in
 1120 **MPCORB**), and the internal **ssObject** identifier,
 1121 which is used as a key to find solar system object
 1122 observations in the **DiaSource** and **SSSource** ta-
 1123 bles.
 1124
- 1124 The **SSSource** catalog ([NSF-DOE Vera C. Ru-
 1125 bin Observatory 2025o](#)) contains data on all **Dia-
 1126 Sources** that are either associated with previously-
 1127 known Solar System Objects, or have been con-
 1128 firmed as newly-discovered Solar System Objects
 1129 by confirmation of their orbital properties. As en-
 1130 tries in the **SSSource** catalog stem from the **Di-
 1131 aSource** catalog, they have all been detected at
 1132 $> 5\sigma$ significance in at least one band. The **SS-
 1133 Source** catalog contains data for 5988 Solar Sys-
 1134 tem Sources.
 1135

- 1135 The **Calibration** catalog is the reference catalog
 1136 that was used to perform astrometric and photo-
 1137 metric [calibration](#). It is a whole-sky catalog built
 1138 specifically for **LSST**, as no single prior reference
 1139 catalog had both the depth and coverage needed
 1140 to calibrate **LSST** data. It combines data from
 1141 multiple previous reference catalogs and contains
 1142 only stellar sources. Full details on how the **Cal-
 1143 ibration** catalog was built are provided in [P. S.
 1144 Ferguson et al. \(2025\)](#)⁹¹. We provide a brief sum-
 1145 mary here.
 1146

1146 For the *grizy* bands, the input catalogs were (in
 1147 order of decreasing priority): [Dark Energy Sur-
 1148 vey \(DES\)](#) Y6 Calibration Stars (E. S. Rykoff
 1149 et al. 2023); [Gaia-B or R Photometry \(Gaia\)](#)
 1150 ([XP](#)) Synthetic Magnitudes ([Gaia](#) Collec-
 1151 tion et al. 2023a); the [Panoramic Survey Teles-
 1152 cope and Rapid Response System \(Pan-STARRS\)1 3PI](#)
 1153 Survey (K. C. Chambers et al. 2016); [Data Re-
 1154 lease 2 of the SkyMapper survey \(C. A. Onken](#)
 1155 et al. 2019); and [Data Release 4 of the VLT Sur-
 1156 vey Telescope \(VST\) Asteroid Terrestrial-impact](#)

⁹¹ In [P. S. Ferguson et al. \(2025\)](#), the calibration reference catalog is referred to as “The Monster”. This terminology is also carried over to the DP1 Butler.

1157 Last Alert System (ATLAS) survey (T. Shanks
 1158 et al. 2015). For the *u*-band, the input catalogs
 1159 were (in order of decreasing priority): Standard
 1160 Stars from Sloan Digital Sky Survey (SDSS) Data
 1161 Release 16 (R. Ahumada et al. 2020); Gaia-XP
 1162 Synthetic Magnitudes (Gaia Collaboration et al.
 1163 2023a); and synthetic magnitudes generated us-
 1164 ing Single Lens Reflex (SLR), which estimates the
 1165 *u*-band **flux** from the *g*-band **flux** and *g-r* colors.
 1166 This **SLR** estimates were used to boost the num-
 1167 ber of *u*-band reference sources, as otherwise the
 1168 source density from the *u*-band input catalogs is
 1169 too low to be useful for the **LSST**.

1170 Only stellar sources were selected from each input
 1171 catalog. Throughout, the **Calibration** catalog
 1172 uses the **DES** bandpasses for the *grizy* bands and
 1173 the **SDSS** bandpass for the *u*-band; color trans-
 1174 formations derived from high quality sources were
 1175 used to convert fluxes from the various input cat-
 1176 alogs (some of which did not use the **DES**/**SDSS**
 1177 bandpasses) to the respective bandpasses. All
 1178 sources from the input catalogs are matched to
 1179 **Gaia-Data Release 3 (DR3)** sources for robust
 1180 astrometric information, selecting only isolated
 1181 sources (i.e., no neighbors within 1").

1182 After collating the input catalogs and transform-
 1183 ing the fluxes to the standard **DES**/**SDSS** band-
 1184 passes, the catalog was used to identify sources
 1185 within a specific region of the sky. This process
 1186 generated a set of standard columns containing
 1187 positional and flux information, along with their
 1188 associated uncertainties.

1189 3.2.1. *Source and Object Designations*

1190 To refer to individual sources or objects from the DP1
 1191 catalogs, one should follow the LSST DP1 naming con-
 1192 vention that has been registered with the International
 1193 Astronomical Union. Because the **Source**, **Object**, **Di-**
 1194 **aSource**, **DiaObject**, and **SSObject** tables each have
 1195 their own unique IDs, their designations should dif-
 1196 fer. In general, source designations should begin with
 1197 the string "LSST-DP1" (denoting the Legacy Survey
 1198 of Space and Time, Data Preview 1), followed by a
 1199 string specifying the table from which the source was
 1200 obtained. These strings should be "O" (for the **Ob-**
 1201 **ject** table), "S" (**Source**), "DO" (**DiaObject**), "DS"
 1202 (**DiaSource**), or "SSO" (**SSObject**). Following the table
 1203 identifier, the designation should contain the full unique
 1204 numeric identifier from the specified table (i.e., the
 1205 **objectId**, **sourceId**, **diaObjectId**, **diaSourceId**, or **ssObjec-**
 1206 **tId**). Each component of the identifier should be sep-
 1207 arated by dashes, resulting in a designation such as

1208 "LSST-DP1-TAB-123456789012345678". In summary,
 1209 source designations should adhere to the formats listed
 1210 below:

- 1211 • Object: LSST-DP1-O-609788942606161356 (for
 1212 **objectId** 609788942606161356)
- 1213 • Source: LSST-DP1-S-600408134082103129 (for
 1214 **sourceId** 600408134082103129)
- 1215 • DiaObject: LSST-DP1-DO-609788942606140532
 1216 (for **diaObjectId** 609788942606140532)
- 1217 • DiaSource: LSST-DP1-DS-600359758253260853
 1218 (for **diaSourceId** 600359758253260853)
- 1219 • SSObject: LSST-DP1-SSO-21163611375481943
 1220 (for **ssObjectId** 21163611375481943)

1221 Tables that were not explicitly mentioned in the de-
 1222 scription above do not have their own unique IDs, but
 1223 are instead linked to one of the five tables listed above
 1224 via a unique ID. For example, the **ForcedSource** ta-
 1225 ble is keyed on **objectId**, **ForcedSourceOnDiaObject**
 1226 uses **diaObjectId**, **SSSource** is linked to **diaSourceId** and
 1227 **ssObjectId**, and **MPCORB** uses **ssObjectId**.

1228 3.3. *Survey Property Maps*

1229 Maps are two-dimensional visualizations of survey
 1230 data. In **DP1**, these fall into two categories: Survey
 1231 Property Maps and **Hierarchical Progressive Sur-**
 1232 **vey (HiPS)** Maps (P. Fernique et al. 2015). Survey
 1233 Property Maps (**NSF-DOE Vera C. Rubin Observatory**
 1234 **2025p**) summarize how properties such as observing con-
 1235 ditions or exposure time vary across the observed sky.
 1236 Each map provides the spatial distribution of a spe-
 1237 cific quantity at a defined sky position for each band
 1238 by aggregating information from the images used to
 1239 make the **deep_coadd**. Maps are initially created per-
 1240 **tract** and then combined to produce a final consolidated
 1241 map. At each sky location, represented by a spatial pixel
 1242 in the **Hierarchical Equal-Area iso-Latitude Pixelisation**
 1243 (**HEALPix**)(K. M. Górski et al. 2005) grid, values are
 1244 derived using statistical operations, such as minimum,
 1245 maximum, mean, weighted mean, or sum, depending on
 1246 the property.

1247 **DP1** contains 14 survey property maps. The avail-
 1248 able maps describe total exposure times, observation
 1249 epochs, **PSF** size and **shape**, **PSF** magnitude limits,
 1250 sky **background** and noise levels, as well as astro-
 1251 metric shifts and **PSF** distortions due to wavelength-
 1252 dependent atmospheric **Differential Chromatic Refrac-**
 1253 **tion (DCR)** effects. They all use the dataset type

1254 format `deep_coadd_<PROPERTY>_consolidated_map_-` 1299
 1255 `<STATIC>`. For example, `deep_coadd_exposure_-`
 1256 `time_consolidated_map_sum` provides a spatial map of
 1257 the total exposure time accumulated per sky position in
 1258 units of seconds. All maps are stored in `HealSparse`⁹²
 1259 format. Survey property maps are only available via
 1260 the Data Butler (§6.2.2) and have dimensions `band` and
 1261 `skymap`.

1262 Figure 8 presents three survey property maps for ex-
 1263 posure time, PSF magnitude limit, and sky noise, com-
 1264 puted for representative tracts and bands. Because full
 1265 consolidated maps cover widely separated tracts, we use
 1266 clipped per-tract views here to make the spatial patterns
 1267 more discernible. Many more survey property maps are
 1268 available in the DP1 repository.

1270 3.4. *HiPS Maps*

1271 **HiPS** Maps (P. Fernique et al. 2015), offer an inter-
 1272 active way to explore seamless, multi-band tiles of the
 1273 sky regions covered by DP1, allowing for smooth pan-
 1274 ning and zooming. DP1 provides multi-band **HiPS** im-
 1275 ages created by combining data from individual bands
 1276 of `deep_coadd` and `template_coadd` images. These im-
 1277 ages are false-color representations generated using
 1278 various filter combinations for the red, green, and blue
 1279 channels. The available filter combinations include *gri*,
 1280 *izy*, *riz*, and *ugr* for both `deep_coadd` and `template_-`
 1281 `coadd`. Additionally, for `deep_coadd` only, we provide
 1282 color blends such as *uug* and *grz*. Post-DP1, we plan
 1283 to also provide single-band HiPS images for all *ugrizy*
 1284 bands in both **Portable Network Graphics (PNG)** and
 1285 **Flexible Image Transport System (FITS)** formats.

1286 HiPS maps are only accessible through the **HiPS**
 1287 viewer in the **Rubin Science Platform (RSP)** Portal
 1288 (§6.3) and cannot be accessed via the Data Butler
 1289 (§6.2.2). All multi-band **HiPS** images are provided in
 1290 **PNG** format.

1291 3.5. *Metadata*

1292 DP1 also includes `metadata` about the observations,
 1293 which are stored in the `Visit` table. The data it con-
 1294 tains was produced by the observatory directly, rather
 1295 than the science pipelines. It contains technical data
 1296 for each visit, such as telescope pointing, camera rota-
 1297 tion, `airmass`, exposure start and end time, and total
 1298 exposure time.

3.6. *Ancillary Data Products*

1300 DP1 also includes several ancillary data products.
 1301 While we do not expect most users to need these, we
 1302 describe them here for completeness. All the Data Prod-
 1303 ucts described in this section can only be accessed via
 1304 the Data Butler (§6.2.2).

1305 3.6.1. *Standard Bandpasses*

1306 **Figure 3** shows the full-system throughput of the six
 1307 LSSTComCam filters. The corresponding transmission
 1308 curves are provided as a DP1 data product. These
 1309 datasets tabulate the full-system transmission of the six
 1310 LSSTComCam filters as a function of wavelength and
 1311 were used as a reference for the LSSTComCam DP1
 1312 photometry. The `standard_passband` dataset is keyed
 1313 by band and is stored in Astropy Table format.

1314 3.6.2. *Task configuration, log, and metadata*

1315 DP1 includes `provenance`-related data products such
 1316 as task logs, `configuration` files, and task metadata.
 1317 Configuration files record the parameters used in each
 1318 processing task, while logs and `metadata` contain infor-
 1319 mation output during processing. These products help
 1320 users understand the processing setup and investigate
 1321 potential processing failures.

1322 3.6.3. *Calibration Data Products*

1323 Calibration data products include a variety of images
 1324 and models that are used to characterize and correct
 1325 the performance of the camera and other system com-
 1326 ponents. These include bias, dark, and flat-field images,
 1327 **Photon Transfer Curve (PTC)** gains, brighter-fatter ker-
 1328 nels (P. Antilogus et al. 2014), charge transfer ineffi-
 1329 ciency (CTI) models, linearizers, and illumination cor-
 1330 rections. For flat-field corrections, DP1 processing used
 1331 combined flats, which are averaged from multiple indi-
 1332 vidual flat-field exposures to provide a stable `calibra-`
 1333 `tion`. These `calibration` products are essential inputs
 1334 to `Instrument Signal Removal (ISR)` (§4.2.1). While
 1335 these products are included in DP1 for transparency and
 1336 completeness, users should not need to rerun ISR for
 1337 their science and are advised to start with the processed
 1338 `visit_image`.

1339 4. DATA RELEASE PROCESSING

1340 **Data Release Processing (DRP)** is the systematic pro-
 1341 cessing of all Rubin Observatory data collected up to
 1342 a certain date to produce the calibrated images, cata-
 1343 logs of detections, and derived data products described
 1344 in Section 3. DP1 was processed entirely at the **United**

⁹² A sparse **HEALPix** representation that efficiently encodes data values on the celestial sphere. <https://healsparse.readthedocs.io>

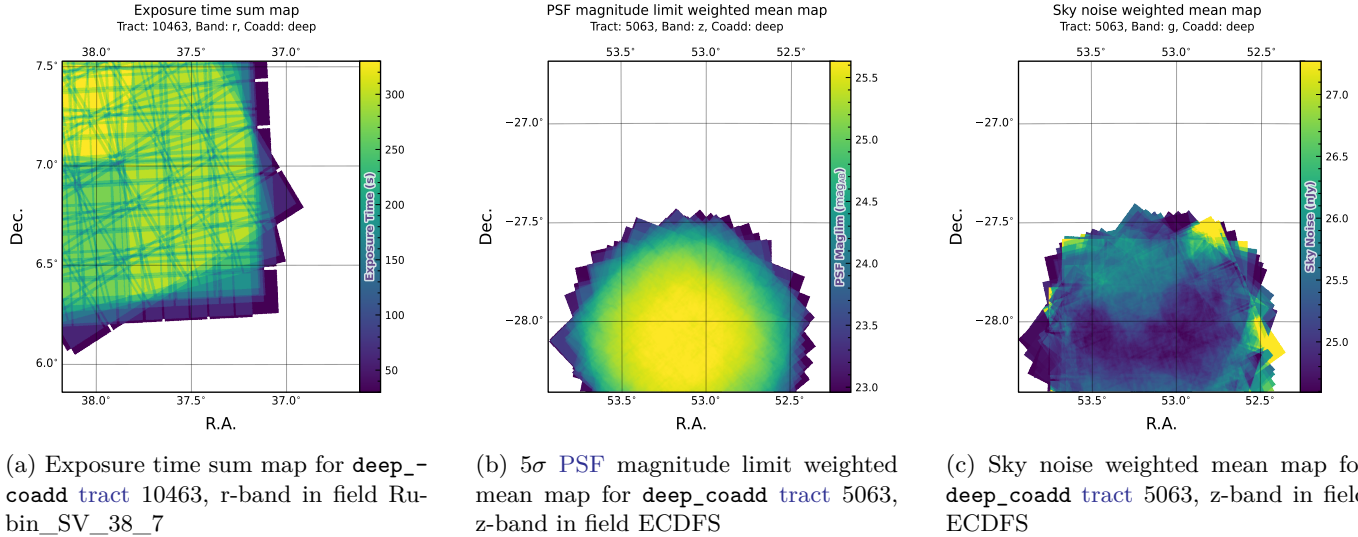


Figure 8. Examples of survey property maps from Rubin DP1 across different bands, clipped to the boundary of a single tract for visual clarity.

1345 States Data Facility (USDF) at SLAC using 17,024 CPU
 1346 hours.⁹³

1347 This section describes the pipeline algorithms used to
 1348 produce DP1 and how they differ from those planned for
 1349 full-scale LSST data releases. Data Release Production
 1350 consists of four major stages: (1) single-frame process-
 1351 ing, (2) calibration, (3) coaddition, and (4) difference
 1352 image analysis (DIA).

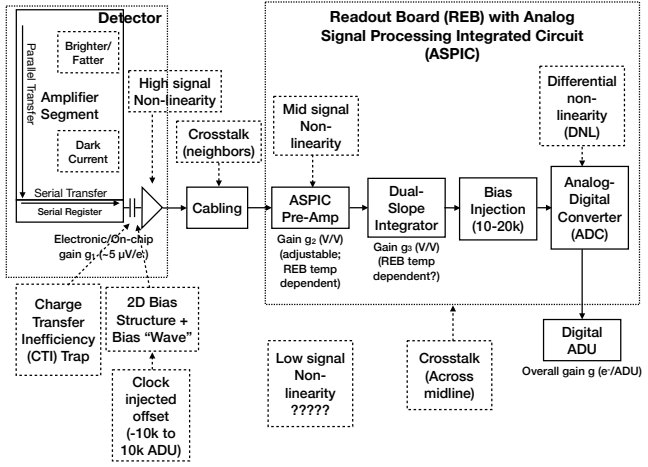
1353 4.1. LSST Science Pipelines Software
 1354 The LSST Science Pipelines software (Rubin Observatory
 1355 Science Pipelines Developers 2025; J. D. Swinbank
 1356 et al. 2020) will be used to generate all Rubin Observatory
 1357 and LSST data products. It provides both the algorithms
 1358 and middleware frameworks necessary to process
 1359 raw data into science-ready products, enabling analysis
 1360 by the Rubin scientific community. Version v29.1 of the
 1361 pipelines was used to produce DP1⁹⁴.
 1362 4.2. Single Frame Processing
 1363 4.2.1. Instrument Signature Removal
 1364 The first step in processing LSSTComCam images is
 1365 to correct for the effects introduced by the telescope and
 1366 detector. Each sensor and its readout amplifiers can
 1367 vary slightly in performance, causing images of even a
 1368 uniformly illuminated focal plane to exhibit discontinu-
 1369 ties and shifts due to detector effects. The ISR pipeline
 1370 aims to recover the original astrophysical signal as best
 1371 as possible and produce science-ready single-epoch im-
 1372 ages for source detection and measurement. A detailed
 1373 description of the ISR procedures can be found in P. Fag-
 1374 relius & E. S. Rykoff (2025); A. A. Plazas Malagón et al.
 1375 (2025). Figure 9 illustrates the model of detector com-
 1376 ponents and readout electronics and their impact on the
 1377 signal, tracing the process from photons incident on the
 1378 detector surface to the final quantized values⁹⁵ recorded
 1379 in the image files. The ISR pipeline essentially “works
 1380 backward” through the signal chain, correcting the in-
 1381 teger analog-to-digital units (ADU) raw camera output
 1382 back to a floating-point number of photoelectrons cre-
 1383 ated in the silicon. The physical detector, shown on the
 1384 left in Figure 9, is the source of effects that arise from the
 1385 silicon itself, such as the dark current and the brighter-
 1386 fatter effect (A. A. Plazas et al. 2018; A. Broughton
 1387 et al. 2024). After the integration time has elapsed, the
 1388 charge is shifted to the serial register and read out, which
 1389 can introduce charge transfer inefficiencies and a clock-
 1390 injected offset level. The signals for all amplifiers are
 1391 transferred via cables to the Readout Electronics Board
 1392 (REB), during which crosstalk between the amplifiers
 1393 may occur. The Analog Signal Processing Integrated
 1394 Circuit (ASIC) on the REB converts the analog sig-
 1395 nal from the detector into a digital signal, adding both
 1396 quantization and a bias level to the image. Although
 1397 the signal chain is designed to be stable and linear, the
 1398 presence of numerous sources of non-linearity indicates
 1399 otherwise.

⁹³ For future Data Releases, data processing will be distributed across the USDF, the French (FrDF) and UK (UKDF) data facilities.

⁹⁴ Documentation for this version is available at: https://pipelines.lsst.io/v/v29_1_1

⁹⁵ The images written to disk by the camera have values that are integers that come from the ADC converting an analog voltage.

1400 The **ISR** processing pipeline for **DP1** performs, in
 1401 the following order: **Analogue-to-Digital Unit (ADU)**
 1402 dithering to reduce quantization effects, serial over-
 1403 scan subtraction, saturation masking, gain normaliza-
 1404 tion, crosstalk correction, parallel overscan subtraction,
 1405 linearity correction, serial **CTI** correction, image as-
 1406 sembly, bias subtraction, dark subtraction, brighter-fatter
 1407 correction, defect masking and interpolation, variance
 1408 plane construction, flat fielding, and amplifier offset
 1409 (amp-offset) correction⁹⁶. Flat fielding for **DP1** was per-
 1410 formed using combined flats produced from twilight flats
 1411 acquired with sufficient rotational dithering to mitigate
 1412 artifacts from print-through stars, as described in §2.3.



1413 **Figure 9.** The model of the detector and REB components,
 1414 labeled with the effects that they impart on signal.

4.2.2. Background Subtraction

1415 The background subtraction algorithms in the LSST
 1416 Science Pipelines estimate and remove large-scale back-
 1417 ground signals from science imaging. Such signals may
 1418 include sky brightness from airglow, moonlight, scat-
 1419 tered light instrumental effects, zodiacal light, and dif-
 1420 fuse astrophysical emission. In so doing, true astrophys-
 1421 ical sources are isolated to allow for accurate detection
 1422 and measurement.

1423 To generate a **background** model, each post-**ISR** image
 1424 is divided into superpixels of 128×128 pixels. Pixels
 1425 with a mask flag set that indicates that they contain
 1426 no useful science data or that they contain **flux** from a
 1427 preliminary source detection are masked. The iterative

1428 3σ clipped mean of the remaining pixels is calculated
 1429 for each superpixel, constructing a **background** statistics
 1430 image. A sixth-order Chebyshev polynomial is fit to
 1431 these values on the scale of a single detector to allow for
 1432 an extrapolation back to the native pixel resolution of
 1433 the post-**ISR** image.

4.3. Calibration

1434 Stars are detected in each post-**ISR** image using a 5σ
 1435 threshold. Detections of the same star across multiple
 1436 images are then associated to identify a consistent set
 1437 of isolated stars with repeated observations suitable for
 1438 use in **PSF** modeling, photometric **calibration**, and as-
 1439 trometric **calibration**.

1440 Initial astrometric and photometric solutions are de-
 1441 rived using only the calibration reference catalogs (see
 1442 §3.2), and an initial **PSF** model is fit using **PSFEx** (E.
 1443 Bertin 2011). These preliminary solutions provide ap-
 1444 proximate source positions, fluxes, and **PSF** shapes that
 1445 serve as essential inputs to the **calibration** process, en-
 1446 abling reliable source matching, selection of high-quality
 1447 stars, and iterative refinement of the final astrometric,
 1448 photometric, and **PSF** models. These preliminary solu-
 1449 tions are subsequently replaced by more accurate fits, as
 1450 described in the following sections.

4.3.1. PSF Modeling

1451 **PSF** modeling in **DP1** uses the **Piff** (M. Jarvis et al.
 1452 2021) package. Our configuration of **Piff** utilizes its **Pix-
 1453 elGrid** model with a fourth-order polynomial interpola-
 1454 tion per **CCD**, except in the *u*-band, where star counts
 1455 are insufficient to support a fourth-order fit. In this
 1456 case, a second-order polynomial is used instead. Details
 1457 on the choice of polynomial order, overall **PSF** modeling
 1458 performance, and known issues are discussed in §5.2.

4.3.2. Astrometric Calibration

1459 Starting from the astrometric solution calculated in
 1460 single frame processing (§4.2), the final astrometric solu-
 1461 tion is computed using the ensemble of visits in a given
 1462 band that overlap a given **tract**. This allows the astro-
 1463 metric solution to be further refined by using all of the
 1464 isolated point sources of sufficient signal-to-noise ratio
 1465 in an image, rather than only those that appear in the
 1466 reference catalog, as is done in single frame processing.
 1467 Using multiple whole visits rather than a single detector
 1468 also allows us to account for effects that impact the full
 1469 focal plane, and for the proper motion and parallax of
 1470 the sources.

1471 In order to perform the fit of the astrometric solu-
 1472 tion, isolated point sources are associated between over-
 1473 lapping visits and with the **Gaia DR3** (Gaia Collabora-
 1474 tion et al. 2023b) reference catalog where possible. The

96 Amp-offset corrections are designed to address systematic discontinuities in background sky levels across amplifier boundaries. The implementation in the LSST Science Pipelines is based on the **Pan-STARRS** Pattern Continuity algorithm (C. Z. Waters et al. 2020).

model used for **DP1** consists of a static map from pixel space to an intermediate frame (the per-detector model), followed by a per-visit map from the intermediate frame to the plane tangent to the telescope boresight (the per-visit model), then finally a deterministic mapping from the tangent plane to the sky. The fit is done using the `gbdes` package (G. M. Bernstein et al. 2017), and a full description is given in C. Saunders (2024).

The per-detector model is intended to capture quasi-static characteristics of the telescope and camera. During **Rubin Operations**, the astrometric solution will allow for separate epochs with different per-detector models, to account for changes in the camera due to warming and cooling and other discrete events. However, for **DP1**, **LSSTComCam** was assumed to be stable enough that all visits use the same per-detector model. The model itself is a separate two-dimensional polynomial for each detector. For **DP1**, a degree 4 polynomial was used; the degree of the polynomial mapping is tuned for each instrument and may be different for LSSTCam. Further improvements may be made by including a pixel-based astrometric offset mapping, which would be fit from the ensemble of astrometric residuals, but this is not included in the **DP1** processing.

The per-visit model attempts to account for the path of a photon from both atmospheric sources and those dependent on the telescope orientation. This model is also a polynomial mapping, in this case a degree 6 two-dimensional polynomial. Correction for **DCR** (§5.4) was not done for **DP1**, but will be included in LSSTCam processing during **Rubin Operations**. Future processing will also likely include a Gaussian Process fit to better account for atmospheric turbulence, as was demonstrated by W. F. Fortino et al. (2021) and P. F. Léget et al. (2021).

The final component of the astrometric **calibration** involves the positions of the isolated point sources included in the fit, which are described by five parameters: sky coordinates, proper motion, and parallax. While proper motions and parallaxes are not released for **DP1**, they are fitted for these sources in the astrometric solution to improve the astrometric calibration.

4.3.3. Photometric Calibration

Photometric **calibration** of the **DP1** dataset is based on the **Forward Global Calibration Method (FGCM)** (FGCM D. L. Burke et al. 2018), adapted for the LSST Science Pipelines (H. Aihara et al. 2022; P. Fagrelius & E. S. Rykoff 2025). We used the **FGCM** to calibrate the full **DP1** dataset with a forward model that uses a parameterized model of the atmosphere as a function of airmass along with a model of the instrument through-

put as a function of wavelength. The **FGCM** process typically begins with measurements of the instrumental throughput, including the mirrors, filters, and detectors. However, because full scans of the **LSSTComCam** as-built filters and individual detectors were not available, we instead used the nominal reference throughputs for the Simonyi Survey Telescope and LSSTCam.⁹⁷ These nominal throughputs were sufficient for the **DP1** calibration, given the small and homogeneous focal plane consisting of only nine **ITL** detectors. The **FGCM** atmosphere model, provided by MODTRAN (A. Berk et al. 1999), was used to generate a look-up table for atmospheric throughput as a function of zenith distance at Cerro Pachón. This model accounts for absorption and scattering by molecular constituents of the atmosphere, including O_2 and O_3 ; absorption by water vapor; and Mie scattering by airborne aerosol particulates. Nightly variations in the atmosphere are modeled by minimizing the variance in repeated observations of stars with a **Signal to Noise Ratio (SNR)** greater than 10, measured using “compensated aperture fluxes”. These fluxes include a local **background** subtraction (see §4.2.2) to mitigate the impact of **background** offsets. The model fitting process incorporates all six bands (*ugrizy*) but does not include any gray (achromatic) terms, except for a linear assumption of mirror reflectance degradation, which is minimal over the short duration of the **DP1** observation campaign. As an additional constraint on the fit, we use a subset of stars from the reference catalog (P. S. Ferguson et al. 2025), primarily to constrain the system’s overall throughput and establish the “absolute” calibration.

4.4. Visit Images and Source Catalogs

With the final **PSF** models, **WCS** solutions, and photometric calibrations in place, we reprocess each single-epoch image to produce a final set of calibrated visit images and source catalogs. Source detection is performed down to a 5σ threshold using the updated **PSF** models, followed by measurement of **PSF** and aperture fluxes. These catalogs represent the best single-epoch source characterization, but they are not intended for constructing light curves. For time-domain analysis, we recommend using the **forced photometry** tables described in §4.6.2.

4.5. Coaddition Processing

4.5.1. Coaddition

Only exposures with a **seeing** better than 1.7 arcseconds FWHM are included in the deep coadded images.

⁹⁷ Available at: <https://github.com/lsst/throughputs/tree/1.9>

1576 For the template coadds, typically only the top third of
 1577 visits with the best [seeing](#) are used (although see §3.1 for
 1578 more details), resulting in an even tighter image qual-
 1579 ity cutoff for the template coadds. Exposures with poor
 1580 [PSF](#) model quality, identified using internal diagnostics,
 1581 are excluded to prevent contamination of the coadds
 1582 with unreliable [PSF](#) estimates. The remaining expo-
 1583 sures are combined using an inverse-variance weighted
 1584 mean stacking [algorithm](#).

1585 To mitigate transient artifacts before coaddition, we
 1586 apply the artifact rejection procedure described in [Y. Al-](#)
 1587 [Sayyad \(2018\)](#) that identifies and masks features such as
 1588 satellite trails, optical ghosts, and cosmic rays. It oper-
 1589 ates on a time series of [PSF](#)-matched images resampled
 1590 onto a common pixel grid (“warps”) and leverages their
 1591 temporal behavior to distinguish persistent astrophysical
 1592 sources from transient artifacts.

1593 Artifact rejection uses both direct (where no [PSF](#)-
 1594 matching is performed) and [PSF](#)-matched warps, ho-
 1595 mogenized to a standard [PSF](#) of 1.8 arcseconds FWHM,
 1596 broadly consistent with the 1.7 arcsecond FWHM [see-](#)
 1597 [ing](#) threshold used in data screening. A sigma-clipped
 1598 mean of the [PSF](#)-matched warps serves as a static sky
 1599 model, against which individual warps are differenced
 1600 to identify significant positive and negative residuals.
 1601 Candidate artifact regions are classified as [transient](#) if
 1602 they appear in less than a small percentage of the total
 1603 number of exposures, with the threshold based on the
 1604 number of visits, N , as follows:

- 1605 • $N = 1$ or 2 : threshold = 0 (no clipping).
- 1606 • $N = 3$ or 4 : threshold = 1.
- 1607 • $N = 5$: threshold = 2.
- 1608 • $N > 5$: threshold = $2 + 0.03N$.

1609 Identified [transient](#) regions are masked before coaddition,
 1610 improving image quality and reducing contamina-
 1611 tion in derived catalogs.

1612 4.5.2. *Detection, Deblending and Measurement*

1613 After constructing coadded images, sources are de-
 1614 tected in each band, merged across bands, deblended,
 1615 and measured to generate the final object catalogs
 1616 (§3.2). For each coadd in all six bands, we per-
 1617 form source detection at a 5σ detection threshold and
 1618 then adjust the background with a per-patch constant
 1619 (coadds are built from background-subtracted images,
 1620 but the deeper detection on coadds redefines what is
 1621 considered source versus background). Detections across
 1622 bands are merged in a fixed priority order, *irzygu*, to
 1623 form a union detection catalog, which serves as input to
 1624 deblending.

1625 Deblending is performed using the Scarlet Lite algo-
 1626 rithm, which implements the same model as Scarlet ([P.](#)
 1627 [Melchior et al. 2018](#)), but operates on a single pixel grid.
 1628 This allows the use of analytic gradients, resulting in
 1629 greater computational speed and memory efficiency.

1630 [Object](#) measurement is then performed on the de-
 1631 blended detection footprints in each band. Measure-
 1632 ments are conducted in three modes: independent per-
 1633 band measurements, forced measurements in each band,
 1634 and multiband measurements.

1635 Most measurement algorithms operate through a
 1636 single-band plugin system, largely as originally de-
 1637 scribed in [J. Bosch et al. \(2018\)](#). The same plugins are
 1638 run separately for each object on a deblended image,
 1639 which uses the Scarlet model as a template to re-weight
 1640 the original noisy coadded pixel values. This effectively
 1641 preserves the original image in regions where objects are
 1642 not blended, while dampening the noise elsewhere.

1643 A reference band is chosen for each object based on de-
 1644 tection significance and measurement quality using the
 1645 same priority order as detection merging (*irzygu*) and
 1646 a second round of measurements is performed in forced
 1647 mode using the shape and position from the reference
 1648 band to ensure consistent colors ([J. Bosch et al. 2018](#)).

1649 Measurement [algorithm](#) outputs include object fluxes,
 1650 centroids, and higher-order moments thereof like sizes
 1651 and shapes. A variety of [flux](#) measurements are pro-
 1652 vided, from aperture fluxes and forward modeling algo-
 1653 rithms.

1654 Composite model (CModel) magnitudes ([K. Abaza-](#)
 1655 [jian et al. 2004; J. Bosch et al. 2018](#)) are used to cal-
 1656 culate the extendedness parameter, which functions as
 1657 a star-galaxy classifier. Extendedness is a binary clas-
 1658 sifier that is set to 1 if the [PSF](#) model flux is less than
 1659 98.5% of the (free, not forced) CModel flux in a given
 1660 band. Additionally, the extendedness in the reference
 1661 band is provided as a separate column for convenience
 1662 as a multiband star-galaxy classification, and is recom-
 1663 mended generally but also specifically for objects with
 1664 low signal-to-noise ratio in some bands.

1665 Gaussian-Aperture-and-PSF ([Gaussian Aperture and](#)
 1666 [PSF \(GAaP\)](#) [K. Kuijken 2008; A. Kannawadi 2025](#))
 1667 fluxes are provided to ensure consistent galaxy colors
 1668 across bands. Sérsic model ([J. L. Sérsic 1963; J. L. Sersic](#)
 1669 [1968](#)) fits are run on all available bands simultaneously
 1670 ([MultiProFit, D. S. Tararu 2025](#)). The resulting Sérsic
 1671 model fluxes are provided as an alternative to CModel
 1672 and are intended to represent total galaxy fluxes. Like
 1673 CModel, the Sérsic model is a Gaussian mixture approx-
 1674 imation to a true Sérsic profile, convolved with a Gaus-
 1675 sian mixture approximation to the [PSF](#). Sérsic model
 1676 fits also include a free centroid, with all other structural

parameters shared across all bands. That is, the intrinsic model has no color gradients, but the convolved model may have color gradients if the PSF parameters vary significantly between bands.

CModel measurements use a double “shapelet” (A. Refregier 2003) PSF model with a single shared shape. The Sérsic fits are intended to use a double Gaussian with independent shape parameters for each component. Due to a pipeline misconfiguration, the Sérsic fits actually used the shapelet PSF parameters, with the higher-order terms ignored (since MultiProFit does not support shapelet PSFs). This bug has since been fixed and is not expected to impact the galaxy fluxes significantly, since the higher-order shapelet PSF parameters tend to be small. Either way, the double Gaussian PSF parameters are included for each object.

Further details on the performance of these algorithms are found in §5.7.

4.6. Variability Measurement

4.6.1. Difference Imaging Analysis

Difference Image Analysis (DIA) uses the decorrelated Alard & Lupton image differencing algorithm (D. J. Reiss & R. H. Lupton 2016). We detected both positive and negative DIASources at 5σ in the difference image. Sources with footprints containing both positive and negative peaks due to offsets from the template position or blending were fit with a dipole centroid code, which simultaneously fits offset positive and negative PSFs.

We filter a subset of DIASources that have pixel flags characteristic of artifacts, non-astrophysical trail lengths, and unphysically negative direct fluxes. We performed a simple spatial association of DIASources into DIAObjects with a one arcsecond matching radius.

The Machine Learning reliability model applied to DP1 was developed with the aim to meet the latency requirements for Rubin Alert Production when executed on CPUs. Accordingly we developed a relatively simple model: a Convolutional Neural Network with three convolutional layers, and two fully connected layers. The convolutional layers have a 5×5 kernel size, with 16, 32, and 64 filters, respectively. A max-pooling layer of size 2 is applied at the end of each convolutional layer, followed by a dropout layer of 0.4 to reduce overfitting. The last fully connected layers have sizes of 32 and 1. The ReLU activation function is used for the convolutional layers and the first fully connected layer, while a sigmoid function is used for the output layer to provide a probabilistic interpretation. The cutouts are generated by extracting postage stamps of 51×51 pixels centered on the detected sources. The input data of the model consist of the tem-

plate, science, and difference image stacked to have an array of `shape` (3, 51, 51). The model is implemented using PyTorch (J. Ansel et al. 2024). The Binary Cross Entropy loss function was used, along with the Adaptive Moment Estimation (Adam) optimizer with a fixed learning rate of 1×10^{-4} , weight decay of 3.6×10^{-2} , and a batch size of 128. The final model uses the weights that achieved the best precision/purity for the test set. Training was done on the SLAC Shared Scientific Data Facility (S3DF) with an NVIDIA model L40S GPU.

The model was initially trained using simulated data from the second DESC Data Challenge (DC2; (LSST Dark Energy Science Collaboration (LSST DESC) et al. 2021)) plus randomly located injections of PSFs to increase the number of real sources, for a total of 89,066 real sources. The same number of bogus sources were selected at random from non-injected DIASources. Once the LSSTComCam data were available, the model was fine-tuned on a subset of the data containing 183,046 sources with PSF injections. On the LSSTComCam test set, the model achieved an accuracy of 98.06%, purity of 97.87%, and completeness of 98.27%. As discussed in §5.8, the injections used to train this model version do not capture all types of astrophysical variability, so performance on the test set will not be representative for variable stars, comets, and other types of variable objects.

4.6.2. Light Curves

To produce light curves, we perform multi-epoch forced photometry on both the direct visit images and the difference images. For light curves we recommend the forced photometry on the difference images (`psDiffFlux` on the ForcedSource Table), as it isolates the variable component of the flux and avoids contamination from static sources. In contrast, forced photometry on direct images includes flux from nearby or blended static objects, and this contamination can vary with seeing. Centroids used in the multi-epoch forced photometry stage are taken either from object positions measured on the coadds or from the DIAObjects (the associated DIASources detected on difference images).

4.6.3. Solar System Processing

Solar system processing in DP1 consists of two key components: the association of observations (sources) with known solar system objects, and the discovery of previously unknown objects by linking sets of *tracklets*⁹⁸.

⁹⁸ A tracklet is defined as two or more detections of a moving object candidate taken in close succession in a single night.

To generate expected positions, ephemerides are computed for all objects found in the Minor Planet Center orbit catalog using the **Sorcha** survey simulation toolkit (Merritt et al., in press)⁹⁹. To enable fast lookup of objects potentially present in an observed visit, we use the **mpsky** package (M. Juric 2025). In each image, the closest DiaSource within 1 arcsecond of a known solar system object’s predicted position is associated to that object.

Solar system discovery uses the **heliolinx** package of asteroid identification and linking tools (A. Heinze et al. 2023). The suite consists of the following tasks:

- Tracklet creation with `make_tracklets`
- Multi-night `tracklet` linking with `heliolinc`
- Linkage post processing (orbit fitting, outlier rejection, and de-duplication) with `link_purify`

The inputs to the **heliolinx** suite included all sources detected in difference images produced by an early processing of the **LSSTComCam** commissioning data, including some that were later rejected as part of **DP1** processing and hence are not part of **DP1**.

About 10% of all commissioning visits targeted the near-ecliptic field Rubin_SV_38_7 chosen to facilitate asteroid discovery. Rubin_SV_38_7 produced the vast majority of asteroid discoveries in **DP1**, as expected, but a few were found in off-ecliptic fields as well.

Tracklet creation with `make_tracklets` used an upper limit angular velocity of 1.5 deg/day, faster than any main belt asteroid and in the range of many **Near-Earth Object (NEO)** discoveries. To minimize false tracklets from fields observed multiple times per night, the minimum `tracklet` length was set to three detections, and a minimum on-sky motion of five arcseconds was required for a valid `tracklet`.

The heart of the discovery **pipeline** is the **heliolinc** task, which connects (“links”) tracklets belonging to the same object over a series of nights. It employs the Heliolinc3D algorithm (S. Eggel et al. 2020; A. Heinze et al. 2022), a refinement of the original Heliolinc algorithm of M. J. Holman et al. (2018).

The **heliolinc** run tested each `tracklet` with 324 different hypotheses spanning heliocentric distances from 1.5 to 9.8 **astronomical unit (au)** and radial velocities spanning the full range of possible bound orbits (eccentricity 0.0 to nearly 1.0). This range of distance encompasses all main belt asteroids and Jupiter Trojans, as well as many comets and Mars-crossers and

some **NEOs**. Smaller heliocentric distances were not attempted here because nearby objects move rapidly across the sky and hence were not likely to remain long enough in an **LSSTComCam** field to be discovered. Candidate linkages, groups of tracklets whose propagated orbits cluster within a radius of 1.33×10^3 au at 1 au, are identified, then post-processed via `link_purify` to yield a final, non-overlapping set of high-confidence asteroid candidates, ranked by orbit-fit residuals and related metrics.

5. PERFORMANCE CHARACTERIZATION AND KNOWN ISSUES

In this section, we provide an assessment of the **DP1** data quality and known issues.

5.1. Sensor Anomalies and ISR

In addition to the known detector features identified before LSSTComCam commissioning, most of which are handled by the ISR processing (see §4.2.1), we discovered a number of new types of anomalies in the **DP1** data. Since no corrections are currently available for these anomalies, they are masked and excluded from downstream data products.

5.1.1. Vampire Pixels

“Vampire” pixels are visible on the images as a bright defect surrounded by a region of depressed flux, as though the defect is stealing charge from its neighboring pixels. Figure 10 shows an example of a vampire pixel near the center of R22_S11 on an *r*-band flat.

From studies on evenly illuminated images, vampires appear to conserve charge. Unfortunately, no unique optimum way exists to redistribute this stolen flux so, following visual inspection, a defect mask was created to exclude them from processing. We have found some similar features on the ITL detectors on LSSTCam, and will use the same approach to exclude them.

5.1.2. Phosphorescence

Some regions of the LSSTComCam CCD raft were seen to contain large numbers of bright defects. An example is shown in Figure 11 in a *g*-band flat. On further investigation, it appears that on some detectors a layer of photoresist wax was incompletely removed from the detector surface during production. As this wax is now trapped below the surface coatings, there is no way to physically clean these surfaces. If this wax responded to all wavelengths equally, then it would likely result in quantum efficiency dips, which might be removable during flat correction. However, it appears that this wax is slightly phosphorescent, with a decay time on the order

⁹⁹ Available at <https://github.com/dirac-institute/sorcha>

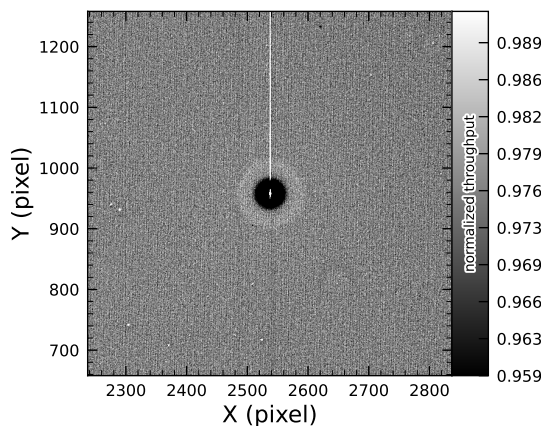


Figure 10. A large vampire pixel near the center of R22_S11, as seen on the *r*-band flat. This clearly shows the central hot "vampire" pixels, surrounded by a region of depressed signal, with a brighter ring surrounding that caused by the local electric field effects. The charge contained in the central pixels is incompletely shifted as the image is read, and that charge leaks out into subsequent rows as they are shifted through the remnant charge. The columns that contain the hot pixels are masked as defects in all processing, as this feature cannot be otherwise corrected.

1870 of minutes, resulting in the brightness of these defects
 1871 being dependent on the illumination of prior exposures.
 1872 The worst of these regions were excluded with manual
 1873 masks.

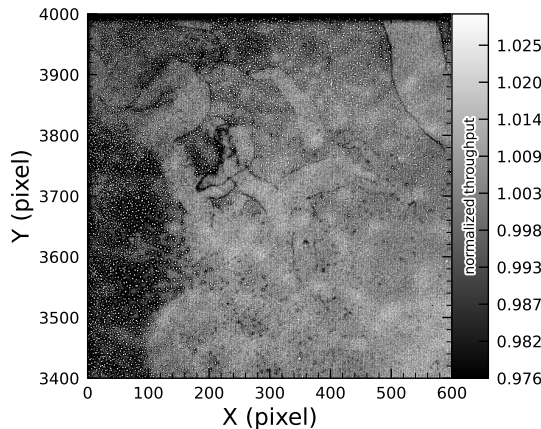


Figure 11. The top left corner of R22_S01 in the *g*-band flat, showing the many small defect features that are caused by the remnant photoresist wax. A single large defect box masks this region from further analysis to prevent these features from contaminating measurements.

1876
 1877
 1878
 1879
 1880
 1881
 1882
 1883
 1884
 1885
 1886
 1887

5.1.3. Crosstalk

Crosstalk refers to unwanted signal interference between adjacent pixels or amplifiers. We use an average inter-amp crosstalk correction based on laboratory measurements with LSSTCam. These average corrections proved satisfactory, and so have been used as-is for DP1 processing. There are, however, some residual crosstalk features present post-correction, with a tendency towards over-subtraction. [Figure 12](#) shows an example of a bright star with over-subtracted crosstalk residuals visible on neighboring amplifiers to both sides on exposure 2024120600239, detector R22_S02.

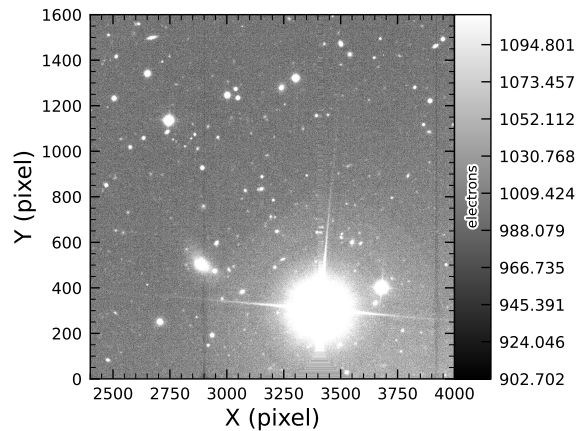


Figure 12. An example of a bright star with over-subtracted crosstalk residuals visible on neighboring amplifiers to both sides (exposure 2024120600239, detector R22_S02). The horizontal banding stretching from the center of the star shows the interpolation pattern covering the saturated core and the ITL edge bleed near the serial register.

1888
 1889
 1890
 1891
 1892
 1893
 1894
 1895
 1896
 1897
 1898

5.1.4. Bleed Trails

Bleed trails are produced when charge from saturated pixels spills into adjacent pixels. Bleed trails were anticipated on LSSTComCam sensors, but they appear in more dramatic forms than had been expected. As a bleed trail nears the serial register, it fans out into a "trumpet" shaped feature. Although bright, these features do not have consistently saturated pixels. In DP1 these "edge bleeds" were identified and masked.

Saturated sources can create a second type of bleed, where the central bleed drops below the background level. The depressed columns along these trails extend across the entire readout column of the detector, crossing the detector mid-line. We developed a model for these to identify which sources are sufficiently saturated to result in such a trail, which is then masked. As this kind of trail appears only on the ITL detectors, we've

1874

1875

1907 named these features “ITL dips”. Figure 13 shows an
 1908 example of a bright star exhibiting the “ITL dip” phe-
 1909 nomenon on exposure: 2024121000503, detector: R22_-
 1910 S21.

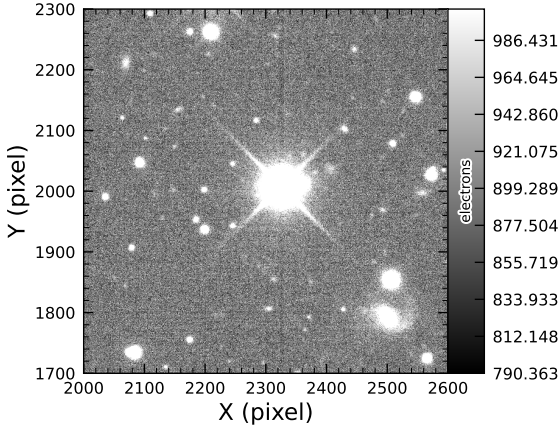


Figure 13. A bright star showing the “ITL dip” phe-
 nomenon, in which a dark trail extends out from the star
 to the top and bottom edges of the detector (exposure:
 2024121000503, detector: R22_S21).

1911
 1912

5.2. PSF Models

1914 To characterize PSF performance, we use adaptive
 1915 second moments (G. M. Bernstein & M. Jarvis 2002)
 1916 measured on PSF stars and on the PSF model using
 1917 the HSM implementation (C. Hirata & U. Seljak 2003;
 1918 R. Mandelbaum et al. 2005). All measurements are ex-
 1919 pressed in the pixel coordinate frame of each detector.
 1920 We characterize the performance of the PSF using the
 1921 classical trace of the second moment matrix T , along
 1922 with the ellipticity parameters e^1 and e^2 . Measure-
 1923 ments on the observed PSF stars are denoted as
 1924 T_{PSF} , e_{PSF}^1 , e_{PSF}^2 , while those from PSF models are
 1925 denoted as T_{model} , e_{model}^1 , e_{model}^2 . We compare two PSF
 1926 modeling approaches:

- Piff with second-order polynomial interpolation (Piff O2), the pipeline’s default, and
- Piff with fourth-order polynomial interpolation (Piff O4), which serves as the final DP1 PSF model.

1927 Table 5 summarizes each model’s ability to reconstruct
 1928 the mean T , e^1 , and e^2 on LSSTComCam. Both models
 1929 exhibit a negative residual bias in the reconstructed PSF
 1930 size, with Piff O4 providing improved performance over
 1931 Piff O2.

1932 An alternative approach to evaluating the perfor-
 1933 mance of the PSF model is to examine the average $\delta T/T$,
 1934

Table 5. Observed mean values and comparison of model residuals, across all visits and filters

Quantity	Observed	Piff O2	Piff O4
$\langle T \rangle$ (pixel ²)	11.366 ± 0.003		
$\langle e^1 \rangle$	$(-6.07 \pm 0.05) \times 10^{-3}$		
$\langle e^2 \rangle$	$(-4.57 \pm 0.05) \times 10^{-3}$		
$\langle e \rangle$	$(8.794 \pm 0.004) \times 10^{-2}$		
$\langle \delta T/T \rangle$		-4.0 ± 0.2	-5.0 ± 0.2
$\langle \delta e^1 \rangle$		0.6 ± 0.1	0.5 ± 0.1
$\langle \delta e^2 \rangle$		0.0 ± 0.1	0.0 ± 0.1

1940 where δT is $T_{\text{PSF}} - T_{\text{model}}$, across visits, projected onto
 1941 focal-plane coordinates, as shown in Figure 14. Piff re-
 1942 veals strong spatial correlations in the residuals, includ-
 1943 ing a systematic offset consistent with the results pre-
 1944 sented in Table 5. The presence of these spatial struc-
 1945 tures motivated the adoption of fourth-order polynomial
 1946 interpolation in all bands except u -band. Although not
 1947 shown in Figure 14, residual patterns persist even with
 1948 third-order interpolation, indicating that it is insuffi-
 1949 cient to capture the complexity of the PSF variation.
 1950 Increasing the interpolation order to five would nomi-
 1951 nally reduce the residuals further, but the limited num-
 1952 ber of stars available on some CCDs would not provide
 1953 adequate constraints for such a model, while the result-
 1954 ing improvement would likely be minimal. Preliminary
 1955 analysis of LSSTCam data in the laboratory at SLAC
 1956 National Accelerator Laboratory (SLAC) shows that the
 1957 ITL sensors exhibit the same pattern as ITL sensors on
 1958 LSSTComCam.

1959 Another way to look at the PSF modeling quality is
 1960 via whisker plots of the PSF second and fourth moments
 1961 and their modeling residuals projected on a part of the
 1962 sky. In addition to the second moment, the spin-2 fourth
 1963 moments, $e^{(4)}$, are defined as:

$$e_1^{(4)} = M_{40} - M_{04}$$

$$e_2^{(4)} = 2(M_{31} - M_{13}),$$

1964 where M_{pq} are the standardized higher moments as de-
 1965 fined in T. Zhang et al. (2023) measured on stars and
 1966 PSF models. Figure 15 shows the whisker plots of e , $e^{(4)}$
 1967 (top rows), and δe , $\delta e^{(4)}$ in the Extended Chandra Deep
 1968 Field-South Survey (ECDFS) field. The direction of a
 1969 whisker represents the orientation of the shape, while
 1970 the length represents the amplitude $|e|$ or $|e^{(4)}|$. We ob-
 1971 serve coherent patterns in both the PSF moments and
 1972

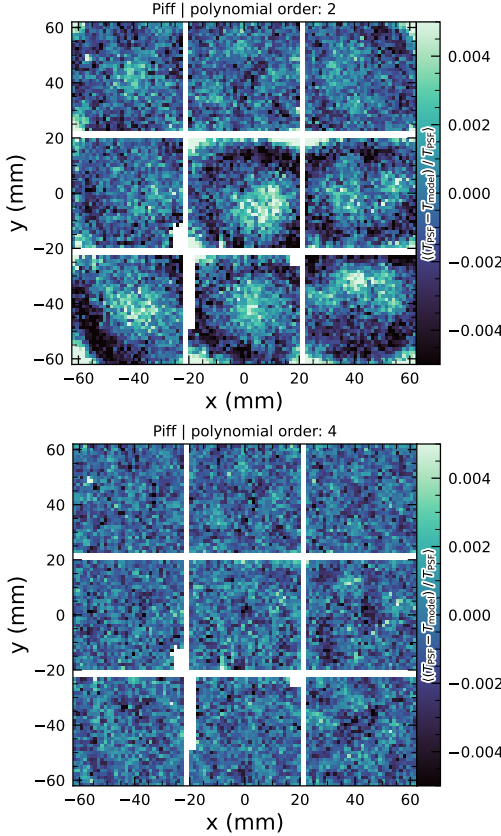


Figure 14. Average across all visits of $\delta T/T$ for Piff O2 and Piff O4 modeling on LSSTComCam. Averages are computed using a 120×120 binning.

the residuals, the latter of which warrants further investigation if it persists in future data releases. ▶

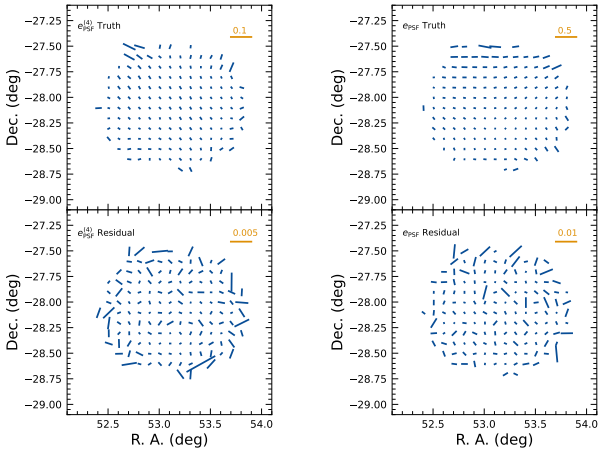


Figure 15. Whisker plots for the ECDFS field for e , $e^{(4)}$ and δe , $\delta e^{(4)}$.

Figure 16 shows a plot of $\delta T/T$ versus stellar magnitude, which can reveal any dependencies between PSF size and flux. We also repeat this analysis in color bins to probe chromatic effects. Binning by color uncovers a clear color dependence, as was also seen in DES (M. Jarvis et al. 2021). The residual is consistent with Table 5 and its cause is unknown. DP1 does not include the color correction implemented in the DES Year 6 analysis, T. Schutt et al. (2025). This will be included in processing of future data releases.

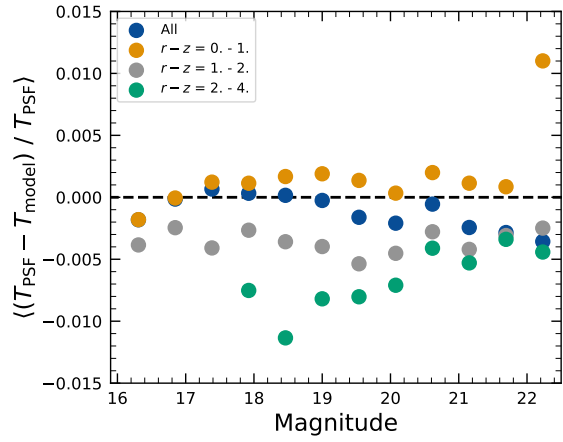


Figure 16. Binned $\delta T/T$ as a function of magnitude across all visits and filters and in bins of stellar colors.

As noted in Rubin Observatory Science Pipelines Developers (2025), two key Piff features were not used in the DP1 processing. PSF color dependence was not implemented, and, while Rubin software allows Piff to work with sky coordinates (including WCS transformations), it does not yet correct for sensor-induced astrometric distortions such as tree rings (H. Y. Park et al. 2017). Both features are planned for upcoming releases.

5.3. Astrometry

To characterize astrometric performance, we evaluate both internal consistency and agreement with an external reference. The primary measure of internal consistency is the repeatability of position measurements for the same object, defined as the RMS of the astrometric distance distribution for stellar pairs having a specified separation in arcminutes. We associate isolated point sources across visits and compute the rms of their fitted positions, rejecting any stars with another star within $2''$. Figure 17 shows the median per-tract rms astrometric error in RA for all isolated point sources, both after the initial calibration and after the final calibration, which includes proper motion corrections. The results indicate that the astrometric solution is already

2014 very good after the initial calibration. Global calibration yields only modest improvement, likely due to the
 2015 short time span of DP1 and the minimal distortions
 2016 in the LSSTComCam. In the main survey, the longer
 2017 time baseline and greater distortions near the LSSTCam
 2018 field edges will make global calibration more impactful.
 2019 An additional measure of internal consistency is the re-
 2020

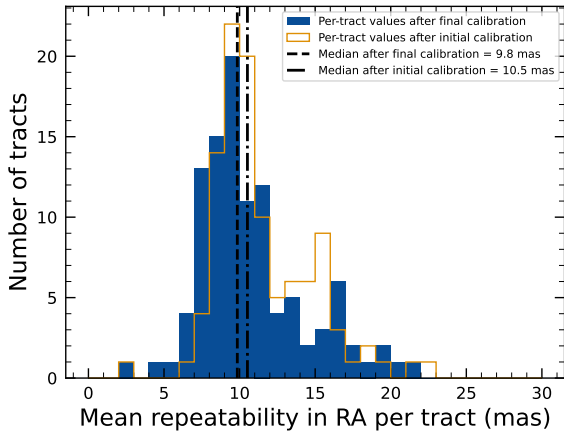


Figure 17. Mean per-tract astrometric repeatability of measurements of isolated point sources in RA in visits across all bands.

2021
 2022
 2023 peatability of separations between objects at a given distance. To compute this, we identify pairs of objects that
 2024 are separated by a specified distance and measure their
 2025 precise separation during each visit in which both ob-
 2026 jects are observed. The scatter in these separation mea-
 2027 surements provides an indication of the internal consis-
 2028 tency of the astrometric model. Figure 18 shows the
 2029 median separation for pairs of objects separated by ap-
 2030 proximately 5 arcminutes, computed per tract after the
 2031 final calibration. These values are already approaching
 2032 the design requirement of 10 mas.
 2033

2034 To assess external consistency, we consider the median
 2035 separation between sources not included in the astromet-
 2036 ric fit and associated objects from a reference catalog.
 2037 For this, we use the Gaia DR3 catalog, with the object
 2038 positions shifted to the observation epoch using the Gaia
 2039 proper motion parameters. Figure 19 shows the median
 2040 separation for each visit in the *r*-band in tract 4849 in
 2041 the ECDFS fields (Table 3). The calculated values are
 2042 almost all within 5 mas, well below the design require-
 2043 ment of 50 mas for the main survey. By examining the
 2044 astrometric residuals, we can assess whether there are
 2045 distortions not accounted for by the astrometric model.
 2046 In some cases, residuals from a single visit exhibit behav-
 2047 ior consistent with atmospheric turbulence, as shown in
 2048 Figure 20, which is characterized by a curl-free gradient
 2049 2050

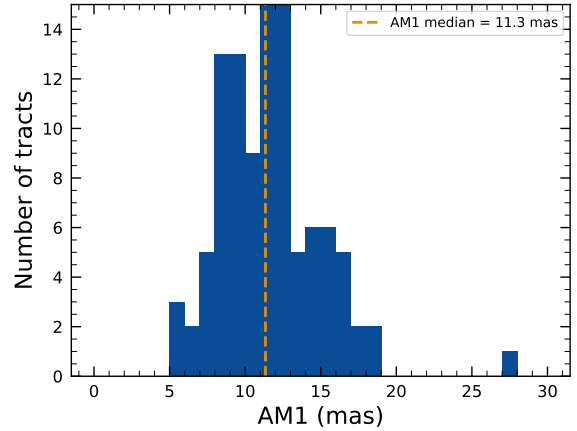


Figure 18. Median per-tract repeatability in separations between isolated point sources 5 arcmin apart in visits across all bands.

2051 field in the two-point correlation function of the resi-
 2052 als (E-mode), P. F. Léget et al. (2021) and W. F. Fortino
 2053 et al. (2021). However, as seen in Figure 21, the resi-
 2055 als in many visits also have correlation functions with
 2056 a non-negligible divergence-free B-mode, indicating that
 2057 some of the remaining residuals are due to unmodeled
 2058 instrumental effects, such as rotations between visits.
 2059

2060 We can see unmodeled camera distortions by stacking
 2061 the astrometric residuals over many visits as a function
 2062 of the focal plane position. Figure 22 shows the median
 2063 residuals in *x* and *y* directions for 1792 visits. Spatial
 2064 structures are evident at the CCD level, as well as at
 2065 the mid-line break, the discontinuity between the two
 2066 rows of amplifiers, in the *y*-direction residuals. Further
 2067 stacking all the detectors makes certain effects particu-
 2068 larly clear. Figure 23 shows distortions very similar to
 2069 those measured for an LSSTCam ITL sensor in a labo-
 2070 ratory setting in J. H. Esteves et al. (2023).
 2071

2073 5.4. Differential Chromatic Refraction

2074 Differential Chromatic Refraction (DCR) occurs when
 2075 light passes through Earth’s atmosphere, refracting
 2076 more for shorter wavelengths, which causes blue light
 2077 to appear shifted closer to the zenith. This wavelength-
 2078 dependent effect results in the smearing of point sources
 2079 along the zenith direction, specifically parallel to the
 2080 parallactic angle. The DCR effect is observable in
 2081 LSSTComCam data, particularly in the angular offset
 2082 versus *g*–*i* band magnitude difference plots, as shown in
 2083 Figure 24. These plots contain 228 visits chosen to max-
 2084 imize the range of observed airmass. When looking at
 2085 data perpendicular to the parallactic angle, sources ex-
 2086 hibit no discernible DCR effect, which is expected, and
 2087 2088

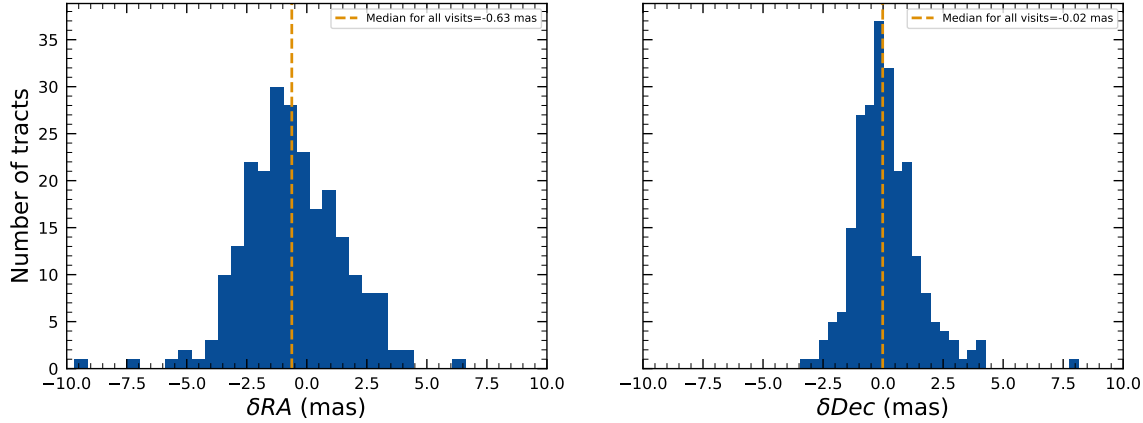


Figure 19. Median absolute offset for all visits in r -band in tract 4849 in the ECDFS field. The offset is the difference between the positions of isolated point sources that were reserved from the astrometric fit and matched objects from the Gaia DR3 catalog.

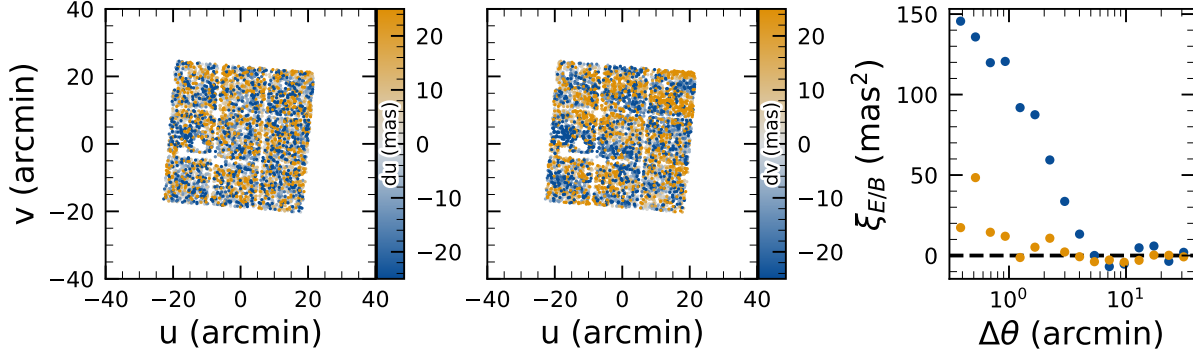


Figure 20. Astrometric residuals in u (left panel) and v (center panel) directions with the E (blue) and B (orange) modes of the two-point correlation function (right panel) seen in visit 2024120200359 in tract 2393 in u band. The residuals show a wave-like pattern characteristic of atmospheric turbulence, and there is significant E-mode and negligible B-mode in the correlation function.

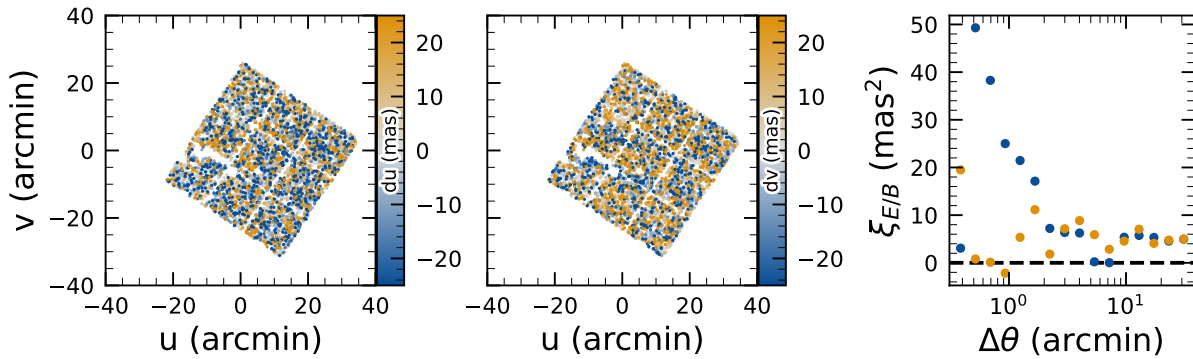


Figure 21. Astrometric residuals in u (left panel) and v (center panel) directions, with the E (blue) and B (orange) modes of the two-point correlation function (right panel) seen in visit 2024120700527 in tract 2393 in u band. There are coherent residuals, but without the wave-like pattern seen in Figure 20, and the correlation function has significant values for both E and B-modes.

form a clear vertical distribution on the two-dimensional density plots in Figure 24.

In contrast, sources aligned with the parallactic angle exhibit a tilted, linear distribution, clearly demon-

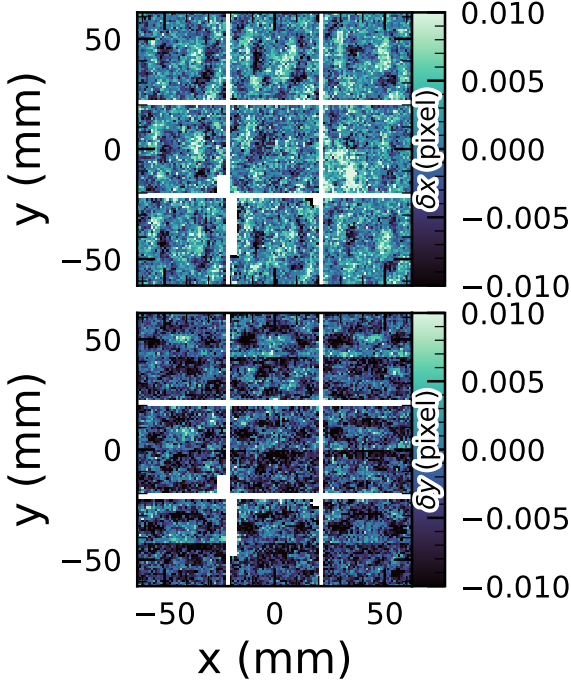


Figure 22. Median astrometric residuals as a function of focal plane position, shown in the left panel for the x direction and in the right panel for the y direction, for all nine LSSTComCam CCDs independently. The range of the color scale is ± 0.01 pixels, corresponding to 2 mas, showing that the effect is small.

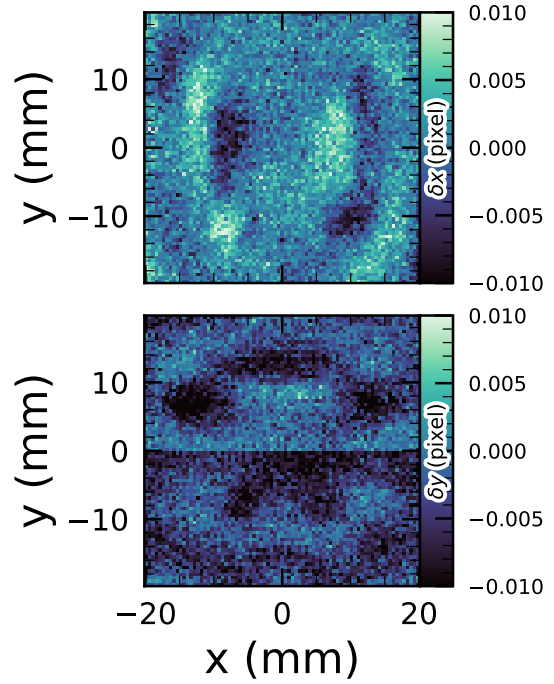


Figure 23. Median residuals as a function of pixel position, shown in the left panel for the x direction and in the right panel for the y direction. These residuals are aggregated across all nine CCDs that comprise the central LSSTComCam raft. The range of the color scale is ± 0.01 pixels, corresponding to 2 mas, showing that the effect is small.

ing that the relationship between angular offset and the $g - i$ band magnitude difference, thereby providing a visual indication of the **DCR** effect. The DCR effect will be addressed in future releases.

5.5. Stellar Photometry

The photometric repeatability for isolated bright unresolved sources following the **FGCM** fits was excellent. For the 10% of unresolved sources withheld from the fit and having signal-to-noise ratios greater than 100, the photometric repeatability after applying chromatic correction was 7.1, 5.4, 5.4, 5.1, 5.9, and 6.5 mmag in the *ugriz* bands respectively, across all fields. After accounting for photometric noise, the intrinsic photometric repeatability was approximately 4.8, 2.7, 1.7, 1.0, 2.0, and 1.1 mmag in *ugriz*. The DP1 processing does not yet include chromatic corrections in the final photometry. In this case the delivered photometric repeatability was 3–8 mmag for *griz*.

In Figure 25, we show the stellar loci for *ugriz* for unresolved sources in the DP1 **Object** table (§3.2). These unresolved sources were selected using the extendedness parameter (§3.2) in the **Object** catalog. This parame-

ter is assigned a value of 0 (unresolved) or 1 (resolved) in each band based on the difference between the PSF and CModel magnitudes. The extendedness is set to 1 when this magnitude difference exceeds 0.016 mag, as the PSF flux for extended sources is biased low relative to the CModel flux. This method has been previously employed by the SDSS pipelines, and its statistical properties, including the optimal combination of information from different bands and repeated measurements, are discussed in C. T. Slater et al. (2020).

Figure 26 illustrates the behavior of the extendness parameter. Its behavior in the g and r bands is similar, with unresolved sources scattered around the vertical line centered on zero. The width of the distribution increases towards fainter magnitudes. Resolved sources are found to the right and the dashed lines in the top panels show the adopted “star-galaxy” separation boundary. The morphology of the two color-magnitude diagrams in the bottom panels suggest that the unresolved sample suffers from increasing contamination by galaxies for $r > 24$. This behavior is consistent with simulation-based predictions from C. T. Slater et al. (2020).

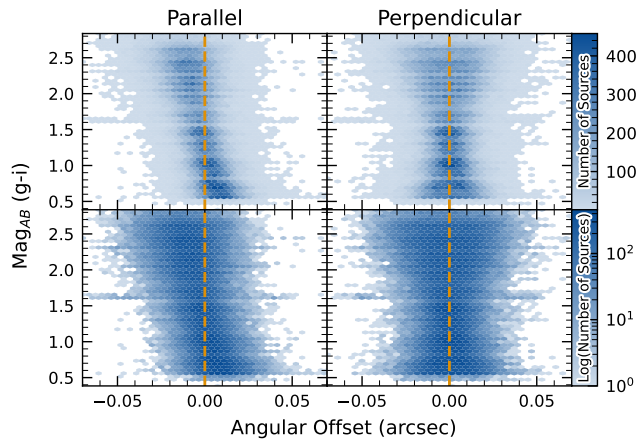


Figure 24. Visualization of Differential Chromatic Refraction (DCR) observed in the LSSTComCam commissioning campaign. The $g - i$ color is computed for every source in the reference catalog that is matched to a direct source in the science image, and the binned density for the full survey is plotted against the angular offset between the reference and detected positions. The angular offset is projected along coordinates parallel and perpendicular to the parallactic angle of the observation, and shows a characteristic correlation along the parallel axis with no correlation along the perpendicular axis. The orange vertical dashed line indicates the expected $g - i$ magnitude distribution at zero angular offset.

5.6. Detection Completeness on Coadds

We characterize completeness by injecting synthetic sources into coadded images, and by comparing source detections to external catalogs. In both cases, we use a greedy, probabilistic matching algorithm that matches reference objects, in order of descending brightness, to the most likely target within a $0.5''$ radius.

We inject sources in 12 of the patches of the ECDFS region with the deepest coverage. The input catalog contains stars and galaxies from part of the Data Challenge 2 (DC2) simulations (LSST Dark Energy Science Collaboration (LSST DESC) et al. 2021), where the galaxies consist of an exponential disk and de Vaucouleurs (G. de Vaucouleurs 1948, 1953) bulge. To avoid deblender failures from excessive increases in object density, stars with a total flux (i.e., summed across all six bands) brighter than 17.5 mag are excluded, as are galaxies whose total flux is brighter than 15 mag or fainter than 26.5 mag. Half of the remaining objects are selected for injection. Afterwards, individual bulge and disk components fainter than 29 mag are also excluded, both for computational expediency and because their structural properties are less likely to be representative of real galaxies.

Figure 27 shows completeness as a function of magnitude for these injected objects in the ECDFS field. These completeness estimates are comparable to results from matching external catalogs. Matching to the Hubble Legacy Field catalog (G. Illingworth et al. 2016; K. E. Whitaker et al. 2019) reaches 50% completeness at $F775W = 26.13$, or about $i = 25.83$ from differences in matched object magnitudes. Similarly, completeness drops below 90% at $VIS = 23.80$ from matching to Euclid Q1 (Euclid Collaboration et al. 2025) objects, equivalent to roughly $i = 23.5$. The Euclid imaging is of comparable or shallower depth, so magnitude limits at lower completeness percentages than 90% are unreliable, whereas the HST images cover too small and irregular of an area to accurately characterize 80-90% completeness limits.

At the 80% completeness limit, nearly 20% of objects, primarily injected galaxies, are incorrectly classified as stars based on their reference band extendedness. Similarly, the fraction of correctly classified injected stars drops to about 50% at $i = 23.8$ (corresponding to 90% completeness).

This analysis has several caveats. The selection of objects for matching in any catalog is not trivial. Some fraction of the detections are spurious, particularly close to bright stars and their diffraction spikes. Additionally, some objects lie in masked regions of one survey but not another, which has not been accounted for. For injected source matching, the reference catalog does not include real on-sky objects. Based on prior analyses of the DC2 simulations, purity is generally greater than completeness at any given magnitude. Similarly, for bright ($i < 23$) objects classified as stars by reference band extendedness, $< 5\%$ are either unmatched to a Euclid or HST object, or misclassified - that is, selecting on extendedness alone yields a fairly pure but incomplete sample of stars. We expect to remedy some of these shortcomings in future releases.

5.7. Model Flux and Shape Measurement

Figure 28 shows i -band magnitude residuals for CModel and Sérsic measurements using the matched injected galaxies described in §5.6. Similar behavior is seen in other bands. Sérsic fluxes show reduced scatter for galaxies with $i < 22.5$, though CModel fluxes are less biased, with median residuals closer to zero and less magnitude-dependent. For fainter objects, Sérsic fluxes are more biased and less accurate. The magnitude of this bias is considerably larger than previously seen in simulated data and is being investigated. Aperture fluxes - including Kron and GAAp - are not shown as they are not corrected to yield total fluxes. The cor-

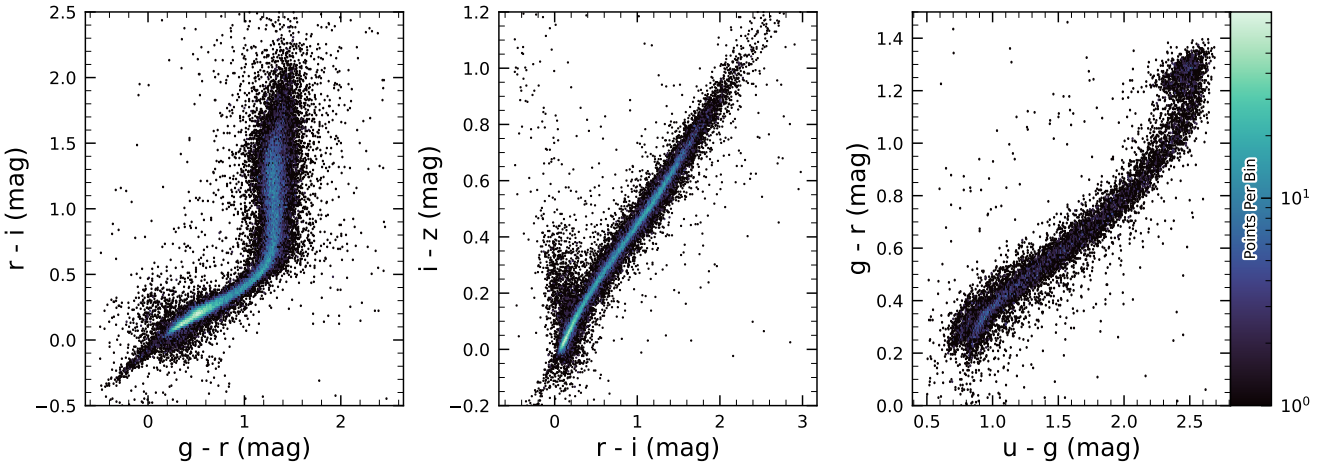


Figure 25. Examples of stellar loci for unresolved sources from the DP1 dataset. From left to right: gri stellar locus containing 63,236 stars with signal-to-noise ratio > 200 in the i band; riz stellar locus containing 46,760 stars with signal-to-noise ratio > 200 in the i band ugr stellar locus containing 12,779 stars with signal-to-noise ratio > 50 in the u band.

rection for Kron fluxes can be derived from the Sérsic index (A. W. Graham & S. P. Driver 2005), but this correction is not provided in object tables.

Figure 29 shows $g - i$ color residuals versus r -band magnitude for the same sample of galaxies as Figure 28. For this and most other colors, GAAP (with a $1''$ aperture) and Sérsic colors both yield lower scatter; however, the CModel colors have the smallest bias. Curiously, the GAAP bias appears to be magnitude-dependent, whereas the Sérsic bias remains stable from $19 < r < 26$. Any of these color measurements are suitable for use for deriving quantities like photometric redshifts, stellar population parameters, etc.

In addition to photometry, some algorithms include measurements of structural parameters like size, ellipticity, and Sérsic index. One particular known issue is that many (truly) faint objects have significantly overestimated sizes and fluxes. This was also seen in the Dark Energy Survey (K. Bechtol et al. 2025), who dubbed such objects “super-spreaders”. These super-spreaders contribute significantly to overestimated fluxes at the faint end (see e.g. Figure 28), and are particularly problematic for the Kron algorithm (R. G. Kron 1980), which should only be used with caution.

As mentioned in §4.5, the Sérsic fits include a free centroid, which is initialized from the fiducial centroid of the object. Preliminary analyses of matched injected objects suggest that the Sérsic model galaxy astrometry residuals are somewhat smaller than for the standard centroids used in other measurements, and so users of the Sérsic photometry should also use these centroid values. One caveat is that for faint objects and/or in crowded regions with unreliable deblending, free cen-

troids can drift significantly and potentially towards other objects, so objects with large differences between the fiducial and Sérsic astrometry should be discarded or used with caution.

Sérsic model parameter uncertainties are estimated by computing and inverting the Hessian matrix with the best-fit parameter values, after replacing the pixel data (but not uncertainties) by the best-fit model values. Currently, only the on-diagonal dispersion term (square root of the variance) is provided as an error estimate for each parameter. Future releases may provide more off-diagonal terms of the covariance matrix - particularly for the structural parameters, which are known to be correlated.

A major outstanding issue is that many parameter uncertainties - including but not limited to those for fluxes - are underestimated. This is at least partly (but not wholly) due to the fact that coaddition introduces covariance between pixels, which is not captured in per-pixel variances.

The degree to which uncertainties are underestimated can depend on the parameter in question and on the brightness of the object. In plots of uncertainty-scaled residuals, the ideal behavior is for the median (i.e. the bias) to lie close to zero, and for the $\pm 1\sigma$ lines to lie at ± 1 , without any dependence on magnitude. Figure 30 shows that flux and color uncertainties for PSF model magnitudes of injected stars are both underestimated, but by a factor of approximately $1.7 - 2$ that is not very sensitive to SNR. This holds for astrometric/centroid parameters as well.

In turn, Figure 31 shows that CModel color uncertainties of galaxies are underestimated by a similar factor at

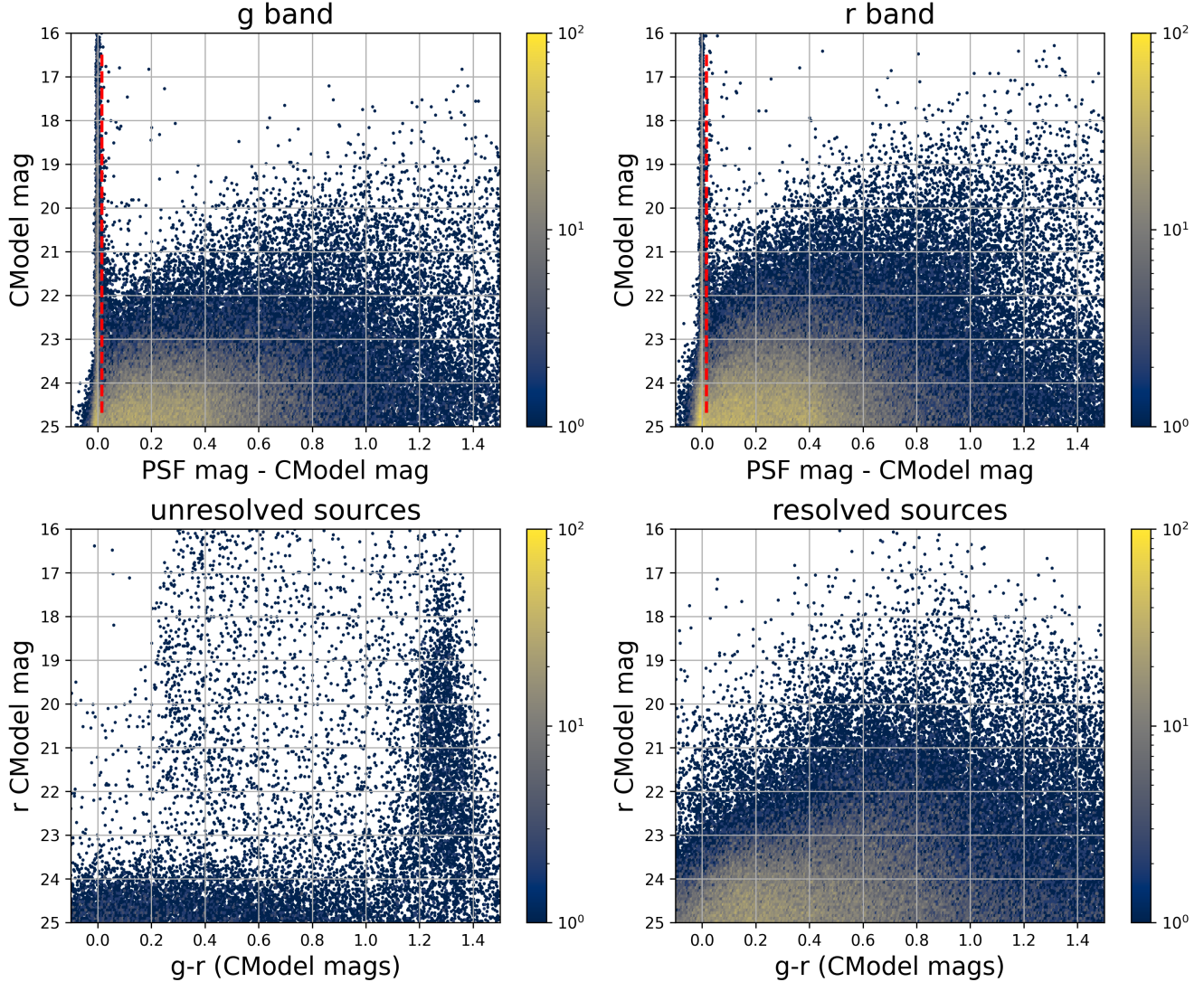


Figure 26. The top two panels shows the difference between the PSF and CModel magnitudes as a function of CModel magnitude in the *g* and *r* bands for 178,547 sources with $CModel_r < 25$ from the ECDFS field. The vertical dashed line in each panel marks the minimum value (0.016 mag) for setting the extendedness parameter to 1. The bottom two panels show the *r* vs. *g-r* color-magnitude diagrams for 14,701 unresolved (left) and 163,666 resolved (right) sources. Note the unresolved sample suffers from increasing contamination by galaxies for $r > 24$.

the faint end, but with appreciable scaling with magnitude (and thereby **SNR**). Flux error underestimation is both larger than for colors and scales more strongly with **SNR**. This indicates that systematic effects dominate the errors in fluxes, particularly for bright galaxies. This is also at least partly but not wholly due to so-called model inadequacy - that is, the fact that galaxy models, parameteric or otherwise, are insufficiently complex to capture the structure of real galaxies.

Figure 32 shows that Sérsic model fluxes and colors have similar behavior as CModel, but with a greater degree of overestimation. This may be partly due to the fact that Sérsic parameter uncertainties are estimated

along with the free centroid and structural (shape and Sérsic index) parameters, whereas the forced CModel fluxes and errors are derived from linear flux fits with a fixed shape and centroid.

Efforts are underway to investigate and quantify the origin of uncertainty underestimates and future releases will, at the least, provide recommendations for mitigations.

5.8. Difference Imaging Purity

We assessed the performance of image differencing using human vetting and source injection (§5.9). Members of the **DP1** team labeled more than 9500 DIASource image triplets consisting of cutouts from the science, tem-

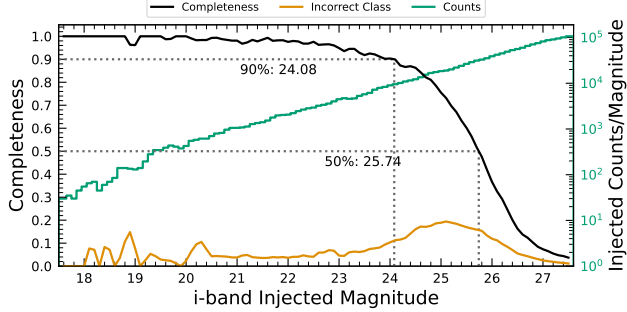


Figure 27. Completeness and incorrect classification fraction as a function of i -band CModel magnitude (Reference Magnitude) for DC2-based injected objects into a portion of the ECDFS field. The “Incorrect Class” line shows the proportion of objects that are matched but classified incorrectly by their reference-band extendedness, i.e. stars with extendedness of 1 or galaxies with extendedness of 0 in the reference band.

plate, and difference images. We classified these into various real and artifact categories. The raw artifact to real ratio without filtering was roughly 9:1. Bright stars are the main source of artifacts. Correlated noise, primarily in u and g bands, also leads to spurious detections near the flux threshold. We expect to be able to mitigate these effects for [LSSTCam](#).

Applying a reliability threshold improves the purity of transients but not variable stars; technical limitations at the time of model training prevented injection of variable stars into the synthetic training set. Reliability models, described in §4.6.1, for [LSSTCam](#) data will be trained on a wider range of input data.

5.9. Difference Imaging Detection Completeness

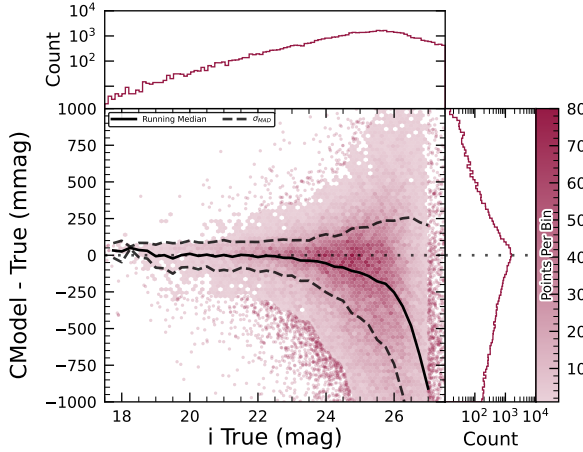
We assess the performance of our difference imaging pipeline using synthetic source injection on the science images prior to differencing. We construct a catalog of injected sources by joining two different samples of point sources, a set of hosted sources to emulate transients in galaxies and second set of hostless sources. The hosts are selected from the pipeline source catalog that is produced upstream by imposing a cut on their extendedness measurement and selecting $N_{\text{src}} = \min(100, N \times 0.05)$ of the N available sources per detector. For each host we pick a random position angle and radius using its light profile shape to decide where to place the source, and also a random value of brightness for the injected source, with magnitudes higher than the host source.

The hostless sources instead have random positions in the [CCD](#) focal plane, and magnitudes chosen from a random uniform distribution with $20 \geq m \geq m_{\text{lim}} + 1$, where m_{lim} is the limiting magnitude of the image. We

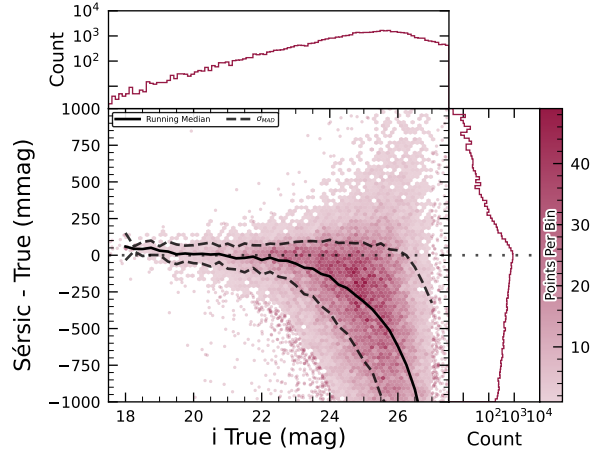
used the [LSST source_injection](#) package¹⁰⁰ to include these sources in our test images. We performed a coordinate cross-match task, with a threshold of $0.^{\circ}5$ to find which of these sources were detected and which were lost, enabling the calculation of a set of performance metrics.

In Figure 33 we show the detection completeness as a function of the [SNR](#), for sources in the [ECDFS](#) field, for filters $griz$. We observe a completeness $> 95\%$ for sources with $\text{SNR} > 6$, with mean completeness $\simeq 99\%$ and standard deviation of $\simeq 0.7\%$. In Figure 34 we show the distribution of the residuals of the recovered sky coordinates for the detected synthetic sources. The marginal distributions are both centered at zero, and for sources of $\text{SNR} > 20$ the residuals are compatible with normal distributions $\mathcal{N}(\mu = 0, \sigma^2 = (0.^{\circ}02)^2)$. In Figure 35 we show photometry results for our detected synthetic sources in the i filter, using [PSF](#) photometry on the difference images. We include both the magnitude residuals as well as the flux pulls, defined as $f_{\text{PSF}} - f_{\text{True}})/\sigma_{f_{\text{PSF}}}$ for PSF flux f_{PSF} and error $\sigma_{f_{\text{PSF}}}$, as a function of the true magnitude of the synthetic sources, including the running median and median absolute deviation (MAD) for the whole brightness range. We also include the true magnitude distribution as well as the detection completeness on the top panel, and for reference the 90% and 50% completeness magnitude values in vertical lines. On the right panels we include the marginal distribution for sources brighter than $mag < 22.5$, splitting the data into hosted and hostless, as well as the robust mean and standard deviation. From this figure we can see that our [flux](#) measurements are accurate within a wide range of magnitudes, for both hosted and hostless synthetic sources. We find that the median offset is below 0.002 mag for true magnitudes below 21, and with a maximum σ_{MAD} scatter of about 0.02 mag in this range. For true $m_i < 22.5$, the robust running median PSF magnitudes residuals are < 0.02 mag, and when splitting into hosted and hostless both robust median are well below 0.01, and robust σ , i.e. σ_{MAD} are also well below 0.05. For all sources with $m_i < 21.5$ the running median is always $|\langle \delta \rangle| < 0.1$, and MAD $\sigma_{\delta} < 1$. Extending to sources with $m_i < 22.5$ then hostless sources have a robust mean pull below 0.02, with a robust standard deviation < 1.15 , while these parameters increase to 0.2 and 1.2 for hosted sources, suggesting that we might have contamination from host background sources potentially biasing our fluxes.

¹⁰⁰ <https://pipelines.lsst.io/modules/lsst.source.injection/index.html>

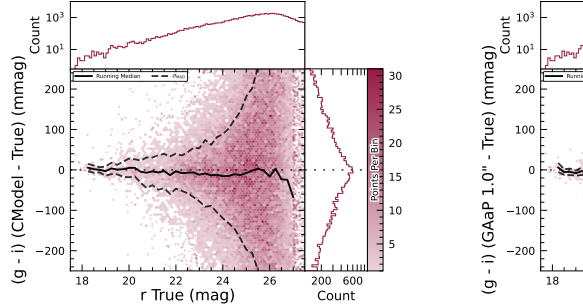


(a) i -band magnitude residuals for CModel measurements of injected galaxies.

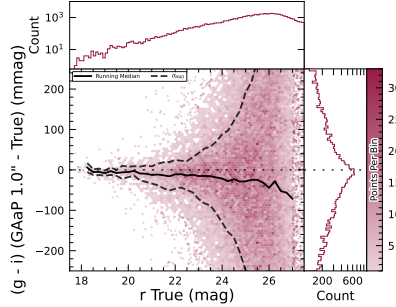


(b) i -band magnitude residuals for Sérsic model measurements of injected galaxies.

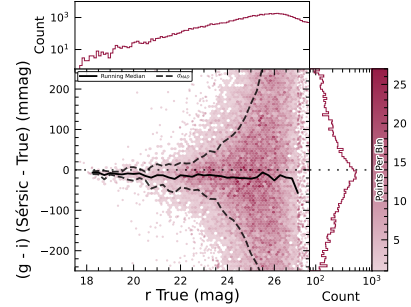
Figure 28. i -band magnitude residuals for matched injected DC2 galaxies with the CModel and Sérsic algorithms in a portion of the [ECDFS](#) region, including the median and scatter thereof. The black line is the median.



(a) $g - i$ color residuals for CModel measurements of injected galaxies.



(b) $g - i$ color residuals for GAAP measurements of injected galaxies.



(c) $g - i$ color residuals for Sérsic model measurements of injected galaxies.

Figure 29. $g - i$ color residuals versus true r -band magnitude for matched injected DC2 galaxies with the CModel, GAAP and Sérsic algorithms in a portion of the [ECDFS](#) region.

2388

5.10. Solar System

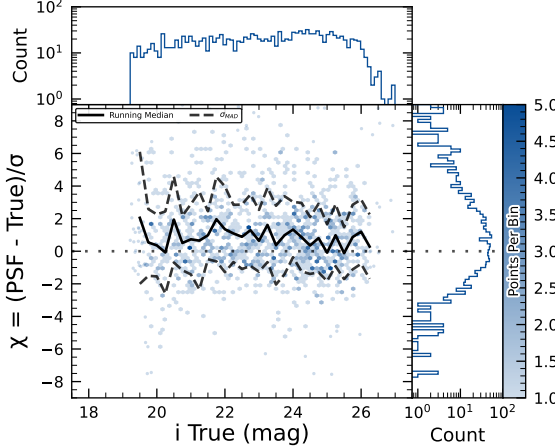
2389

5.10.1. Asteroid Linking Performance

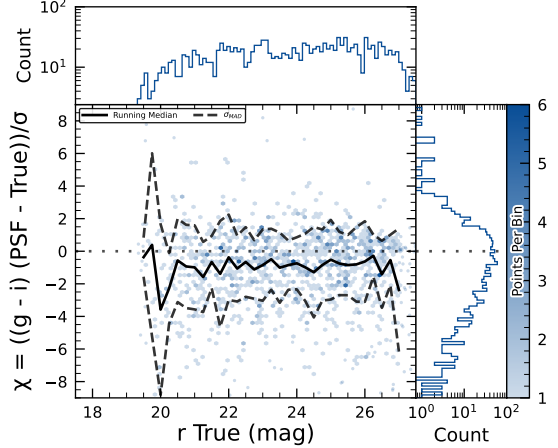
2390 The evaluation of asteroid linking performance in DP1
 2391 focused on demonstrating discovery capability. The solar
 2392 system discovery pipeline produced 269,581 track-
 2393 lets, 5,691 linkages, and 281 post-processed candidates.

2394 As described in §4.6.3, post-processing of the `heli-
 2395 olinc` output with `link_purify` produced a final set of
 2396 281 candidate linkages, ranked with the most promising
 2397 first. We then used `find_orb` (B. Gray 2025) to derive
 2398 orbit fits for each candidate, sorting the resulting list by
 2399 χ_{dof}^2 , a measure of fit quality. A conservative
 2400 manual investigation of these candidates yielded a curated
 2401 list of 93 probable new asteroid discoveries. Manual
 2402 inspection of the linkages indicated that those ranked
 2403 0–137 corresponded to unique real asteroids; ranks 138–
 2404 200 contained additional real objects intermixed with

2405 some spurious linkages; and ranks higher than 200 were
 2406 essentially all spurious. This analysis indicates that it
 2407 will be possible to identify cuts on quality metrics such
 2408 as χ^2 to define discovery candidate samples with high
 2409 purity; determining the exact quantitative cut values re-
 2410 quires more data with [LSSTCam](#). We next removed all
 2411 observations matched to known asteroids (using [Minor](#)
 2412 [Planet Center \(MPC\)](#)’s MPCChecker service), reducing
 2413 the number of candidates to 97. Of these, four had
 2414 strong astrometric and/or photometric outliers, likely
 2415 due to self-subtraction in difference images due to the
 2416 unavoidable limitations of template generation from the
 2417 limited quantity of data available from [LSSTComCam](#). We
 2418 suspect these four linkages do correspond to real
 2419 objects, but have chosen to discard them out of an abun-
 2420 dance of caution. The remaining 93 were submitted to
 2421 the Minor Planet Center and accepted as discoveries,

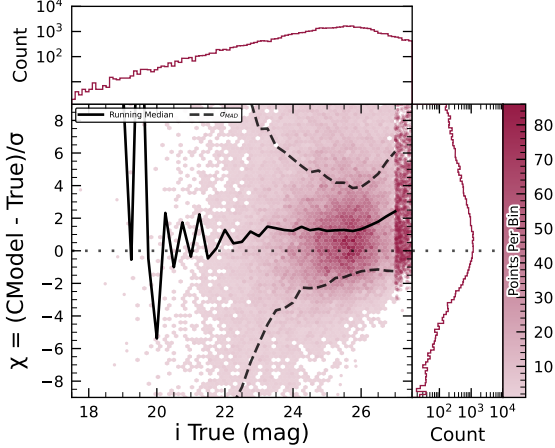


(a) i -band flux uncertainty-scaled residuals for PSF model measurements of injected stars.

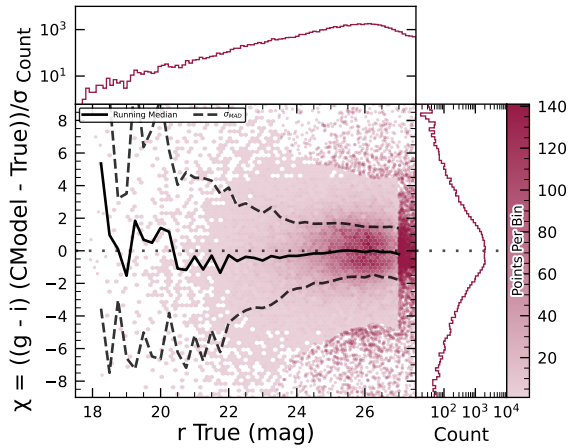


(b) $g - i$ color uncertainty-scaled residuals for PSF model measurements of injected stars.

Figure 30. Color and flux uncertainty-scaled residuals for matched injected DC2 stars’ PSF model measurements in a portion of the ECDFS region.



(a) i -band flux uncertainty-scaled residuals for CModel measurements of injected galaxies.



(b) $g - i$ color uncertainty-scaled residuals for CModel measurements of injected galaxies.

Figure 31. Color and flux uncertainty-scaled residuals for matched injected DC2 galaxies’ CModel measurements in a portion of the ECDFS region.

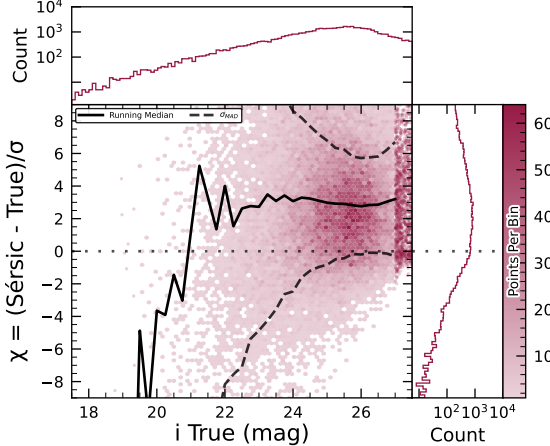
demonstrating the LSST pipelines are able to successfully discover new solar system objects.

2422 specifically the minimum number of detections and/or
2423 the maximum allowed time span between observations.

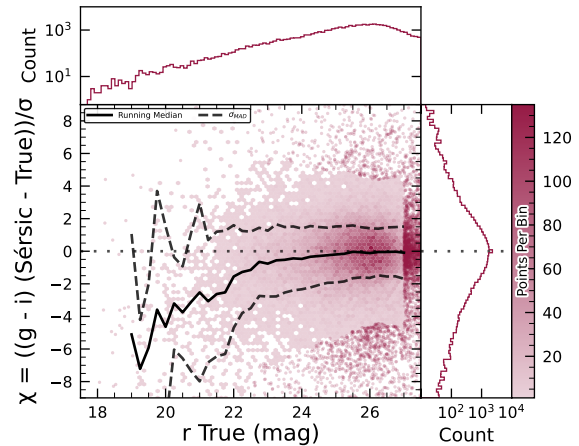
2434 The astrometric residuals of known asteroid associations
2435 are shown in Figure 36. The astrometric precision
2436 for solar system sources is excellent, with the majority
2437 of objects detected within $0.^{\circ}1$ of their expected positions.
2438 Taking the signed median residuals to search for
2439 biases, we find that previously-known objects have mean
2440 residuals of $0.^{\circ}001$ and $-0.^{\circ}016$ in the RA and Dec direc-
2441 tions respectively, while newly-discovered objects have
2442 mean residuals of $-0.^{\circ}035$ and $-0.^{\circ}010$ in the RA and Dec
2443 directions, respectively. These mean residuals are
2444 small enough to eliminate the possibility of a timing offset
2445 greater than the second-scale shutter motion, which

5.10.2. Asteroid Association Performance

2425 During the Solar System association step, 5988 *Di-
2426 aSources* were linked to 431 unique Solar System ob-
2427 jects. These include 3,934 *DiSources* with 338 previ-
2428 ously known objects cataloged by the MPC, and 2,054
2429 *DiSources* with the 93 newly-discovered objects. An
2430 additional 143 detections of these newly discovered ob-
2431 jects were also recovered. These detections were not
2432 initially identified by the discovery pipelines, as they
2433 did not meet the required criteria for tracklet formation,



(a) i -band flux uncertainty-scaled residuals for Sérsic model measurements of injected galaxies.



(b) $g - i$ color uncertainty-scaled residuals for Sérsic model measurements of injected galaxies.

Figure 32. Color and flux uncertainty-scaled residuals for matched injected DC2 galaxies' Sérsic measurements in a portion of the ECDFS region.

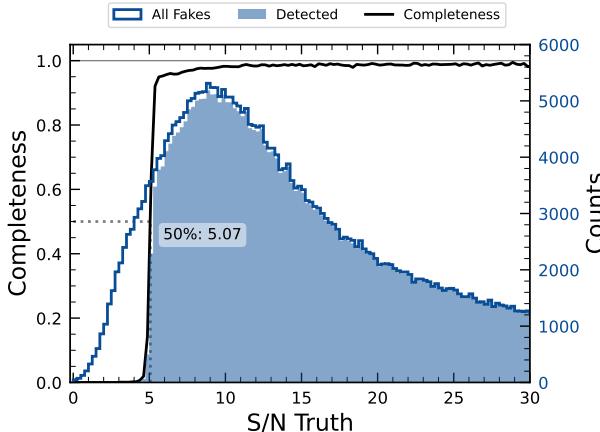


Figure 33. The difference image detection completeness for injected sources in the ECDFS field, for filters $griz$, as a function of the estimated signal to noise ratio SNR. This completeness is the ratio between the found fake sources (shaded histogram) and all the sources (solid line). The horizontal dashed line represents where the 50% completeness level is reached, at approximately $\text{SNR} \simeq 5.07$.

2448 is consistent with the timing studies presented in Section 2.2.2.
2449

2450 5.11. Crowded Fields

2451 Among the seven Rubin DP1 target fields, two stand
2452 out for their severe stellar crowding: the globular cluster
2453 47 Tucanae (47_Tuc) and the Fornax dwarf spheroidal
2454 galaxy (Fornax dSph). These fields were selected in part
2455 to stress-test the LSST Science Pipelines under high-
2456 density conditions. While both exhibit high stellar den-

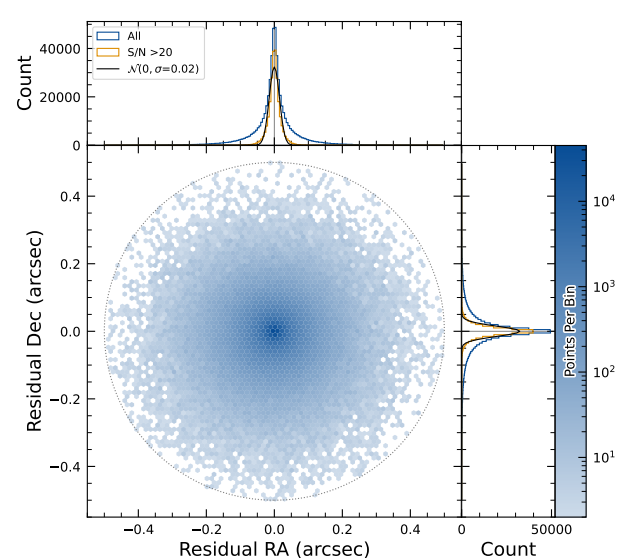


Figure 34. Coordinate residuals for detected synthetic sources in difference images, between recovered and true position of the sources in the ECDFS field. In the top and right panels we include the distribution of these offsets, for all sources as well as for sources with $\text{SNR} > 20$. These high SNR sources show gaussian coordinate residual distributions with $\sigma = 0.02$ (black solid lines). The circle reflects the matching radius of 0.5 .

2457 sities, the nature and spatial extent of the crowding differ significantly.
2458

2459 47 Tuc presents extreme crowding across much of the
2460 field, encompassing its dense core and the eastern re-
2461 gions influenced by the Small Magellanic Cloud (SMC).

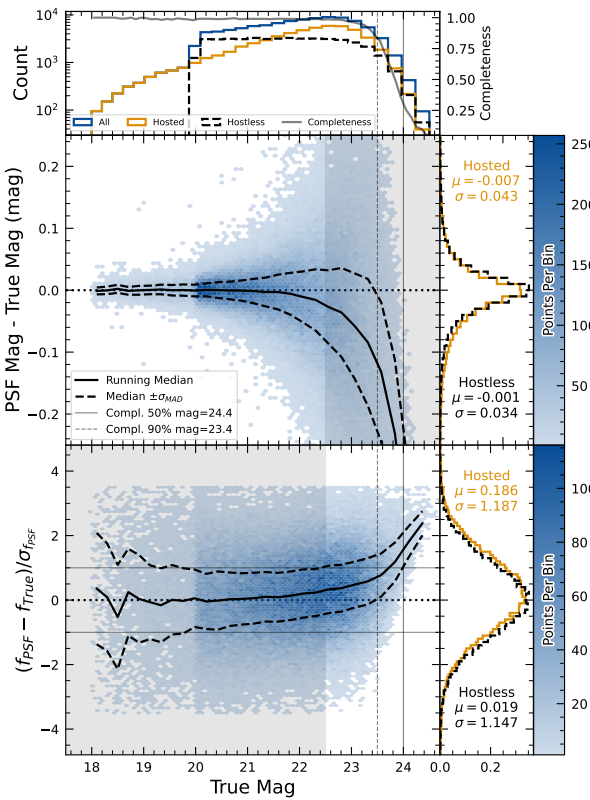


Figure 35. Magnitude residuals and flux pulls for i -band PSF photometry on difference images for ECDFS field in i for detected injected sources. Top panel: Distribution of true magnitudes for injected sources (blue), and split into hostless (black dash) and hosted (orange) sources, with detection completeness as a function of true magnitude (gray line). Vertical dashed lines indicate the 90% and 50% completeness magnitude limits. Center left panel: 2D hexbin plot of PSF magnitude residuals (measured minus true) versus true magnitude for detected sources, with running median (solid black) and σ_{MAD} (dashed black) overlaid. Center right panel: Marginalized distributions of PSF magnitude residuals for hostless (blue) and hosted (orange) sources with true magnitude $m_i < 22.5$, annotated with robust mean and standard deviation. Bottom left panel: 2D hexbin plot of PSF flux pulls versus true magnitude for detected sources, with running median (solid black) and σ_{MAD} (dashed black) overlaid. Bottom right panel: Marginalized distributions of PSF flux pulls for hostless (blue) and hosted (orange) sources with true magnitude $m_i < 22.5$, annotated with robust mean and standard deviation.

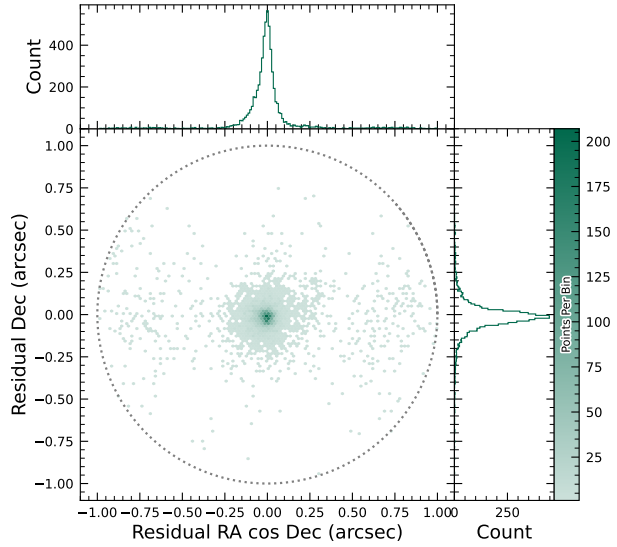


Figure 36. Astrometric residuals between expected and observed positions of Solar System Objects in DP1. The median residuals are $0.^{\prime\prime}001$ and $-0.^{\prime\prime}016$ in R.A./Dec direction, with standard deviations of $0.^{\prime\prime}19$ and $0.^{\prime\prime}10$, respectively. No detectable systematic offset from zero indicates there are no major errors in either timing or astrometry delivered by the Rubin system. The wider scatter in the RA direction is due to objects whose measured orbital elements are less well constrained, translating to larger along-track positional errors in the predicted positions.

2462 This pervasive crowding leads to persistent challenges
 2463 for deblending and reliable source detection, exposing
 2464 field-wide limitations in the current pipeline perform-
 2465 ance (Y. Choi et al. 2025). In contrast, Fornax dSph
 2466 shows significant crowding only in its central region,
 2467 with outer areas remaining well resolved and easier to
 2468 process.

2469 In both 47 Tuc and Fornax, extreme crowding led
 2470 to the deblending step being skipped frequently when
 2471 memory or runtime limits were exceeded, typically due
 2472 to an excessive number of peaks, or large parent foot-
 2473 prints. However, the impact of these limitations dif-
 2474 fered: in 47 Tuc, deblending was often skipped across the
 2475 entire field, resulting in large gaps and substantially re-
 2476 duced completeness. In Fornax, these issues were largely
 2477 confined to the central region, with much better recov-
 2478 ery in the outskirts. This contrast highlights how the
 2479 pipeline’s limitations depend on the spatial extent of
 2480 high-density regions: 47 Tuc exposed systematic, field-
 2481 wide challenges, whereas Fornax revealed more localized,
 2482 density-driven limits.

2483 T. M. Wainer et al. (2025) explored the Rubin DP1
 2484 **DiaObject** catalog (§3.2) in the 47 Tuc field, which
 2485 contains sources detected in difference images. Because
 2486 forced photometry is performed at these positions across
 2487 all single-epoch images, this dataset bypasses the coadd-
 2488 based detection and deblending stages that often fail
 2489 in crowded regions. By computing the median of the
 2490 forced photometry for each **DiaObject** across available
 2491 visits, they recovered approximately three times more
 2492 candidate cluster members than found in the standard
 2493 **Object table** (Y. Choi et al. 2025). This result un-
 2494 derscores the value of difference-imaging-based catalogs
 2495 for probing dense stellar regions inaccessible to standard
 2496 coadd processing in DP1.

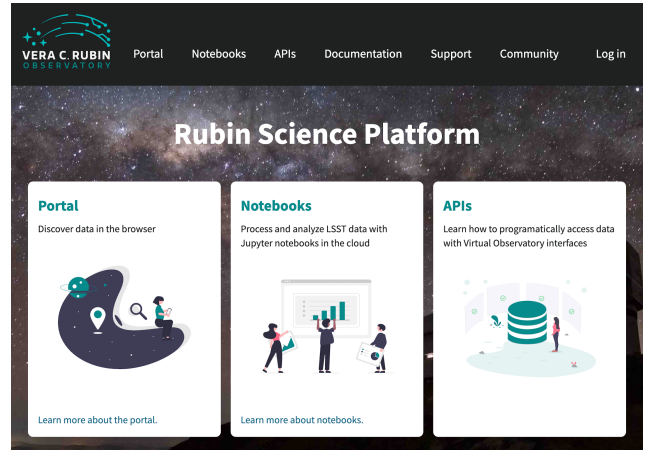
2497 Although the DP1 pipeline was not optimized for
 2498 crowded-field photometry, these early studies of 47 Tuc
 2499 and Fornax provide critical benchmarks. They highlight
 2500 both the limitations and opportunities for science with
 2501 Rubin data in crowded environments, and they inform
 2502 future pipeline development aimed at robust source re-
 2503 covery in complex stellar fields.

2504 6. RUBIN SCIENCE PLATFORM

2505 The **RSP** (M. Jurić et al. 2019) is a powerful, cloud-
 2506 based environment for scientific research and analysis
 2507 of petascale-scale astronomical survey data. It serves
 2508 as the primary interface for scientists to access, visual-
 2509 ize, and conduct next-to-the-data analysis of Rubin and
 2510 LSST data. The **RSP** is designed around a “bring the
 2511 compute to the data” principle, eliminating the need for
 2512 users to download massive datasets. Although **DP1** is
 2513 much smaller in size (3.5 TB) than many current sur-
 2514 vey datasets, future LSST datasets will be far larger and
 2515 more complex, making it crucial to co-locate data and
 2516 analysis for effective scientific discovery.

2517 The **RSP** provides users with access to data and
 2518 services through three distinct user-facing Aspects: a
 2519 *Portal*, which facilitates interactive exploration of the
 2520 data; a JupyterLab-based *Notebook* environment for
 2521 data analysis using Python; and an extensive set of
 2522 *Application Programming Interfaces (APIs)* that enable
 2523 programmatic access to both data and services. The
 2524 three Aspects are designed to be fully integrated, en-
 2525 abling seamless workflows across the **RSP**. The data
 2526 products described in §3 are accessible via all three
 2527 Aspects, and the system facilitates operations such as
 2528 starting a query in one Aspect and retrieving its results
 2529 in another. Figure 37 shows the Rubin Science Platform
 2530 landing page in the Google cloud.

2532 The **RSP** is supported by a number of back-end ser-
 2533 vices, including databases, files, and batch comput-



2534 **Figure 37.** The Rubin Science Platform landing page at
 2535 data.lsst.io showing the three user-facing Aspects as well as
 2536 links to documentation and support information.

2537 ing. Support for collaborative work through shared
 2538 workspaces is also included in the **RSP**.

2539 A preview of the **RSP** was launched on Google Cloud
 2540 in 2022, operating under a shared-risk model to support
 2541 **Data Preview 0** (W. O’Mullane et al. 2024a). This al-
 2542 lowed the community to test the platform, begin prepa-
 2543 rations for science, and provide valuable feedback to in-
 2544 form ongoing development. It was the first time an as-
 2545 tronomical research environment was hosted in a **cloud**
 2546 environment. The DP1 release brings major updates to
 2547 **RSP** services, enhancing scientific analysis capabilities.
 2548 The **RSP** remains under active development, with incre-
 2549 mental improvements being rolled out as they mature.
 2550 During the Rubin Early Science Phase, the **RSP** will
 2551 continue to operate under a shared-risk model. This
 2552 section outlines the RSP functionality available at the
 2553 time of the DP1 release and provides an overview of
 2554 planned future capabilities.

2555 6.1. Rubin Data Access Center

2556 The Rubin US Data Access Center (US DAC) utilizes
 2557 a novel hybrid on-premises-**cloud** architecture, which
 2558 combines on-premises infrastructure at the **USDF** at
 2559 SLAC with flexible and scalable resources in the Google
 2560 **cloud**. This architecture has been deployed and tested
 2561 using the larger simulated data set of DP0.2 (W.
 2562 O’Mullane et al. 2024b).

2563 In this hybrid model, user-facing services are deployed
 2564 in the **cloud** to support dynamic scaling in response to
 2565 user demand and to simplify the provisioning and man-
 2566 agement of large numbers of science user accounts. The
 2567 majority of the static data products described in §3 are
 2568 stored on-premises at the **USDF** to benefit from cost-
 2569 effective mass storage and close integration with Ru-

2567 bin data processing infrastructure, also located at the
 2568 [USDF](#). For imaging data, the Data Butler ([§6.2.2](#)) pro-
 2569 vides the interface between the [cloud](#)-based users and
 2570 data services, and the on-premises data. For catalog
 2571 data, a [cloud](#)-based [TAP](#) client ([§6.2.1](#)) submits queries
 2572 to the on-premises [Qserv](#) database cluster ([§6.5](#)) and re-
 2573 trieves the results. In the initial DP1 deployment, cat-
 2574 alog data is hosted at the [USDF](#) while image data is
 2575 stored in the cloud. The full hybrid model will be rolled
 2576 out and further tested following the release of [DP1](#). The
 2577 RSP features a single-sign-on authentication and auth-
 2578 orization system to provide secure access for Rubin data
 2579 rights holders ([R. Blum & the Rubin Operations Team](#)
 2580 [2020](#)).

2581 6.2. API Aspect

2582 The [API](#) Aspect provides a comprehensive set of user-
 2583 facing interfaces for programmatic access to the [DP1](#)
 2584 data products, through both [IVOA](#)-compliant services
 2585 and the Rubin Data Butler. [IVOA](#) services enable stan-
 2586 dard queries and integration with existing tools, while
 2587 the Butler facilitates advanced data processing within
 2588 the LSST Science Pipelines.

2589 At the time of the [DP1](#) release, some [IVOA](#) ser-
 2590 vices are unavailable, and certain data products are
 2591 only accessible via the Butler. This section provides
 2592 an overview of the available [IVOA](#) services and Butler
 2593 access.

2594 6.2.1. IVOA Services

2595 Rubin has adopted a [Virtual Observatory \(VO\)](#)-first
 2596 design philosophy, prioritizing compliance with [IVOA](#)
 2597 standard interfaces to foster interoperability, standard-
 2598 ization, and collaboration. In cases where standardized
 2599 protocols have yet to be established, additional services
 2600 have been introduced to complement these efforts. This
 2601 approach ensures that the RSP can be seamlessly inte-
 2602 grated with community-standard tools such as [Tool for](#)
 2603 [O](#)[perations on Catalogues And Tables \(TOPCAT\)](#) ([M.](#)
 2604 [Taylor 2011](#)) and [Aladin](#) ([F. Bonnarel et al. 2000; T.](#)
 2605 [Boch & P. Fernique 2014; M. Baumann et al. 2022](#)), as
 2606 well as libraries such as [PyVO](#) ([M. Graham et al. 2014](#)).

2607 The user-facing [APIs](#) are also used internally within
 2608 the [RSP](#), creating a unified design that ensures consis-
 2609 tent and reproducible workflows across all three Aspects.
 2610 This reduces code duplication, simplifies maintenance,
 2611 and ensures all users, both internal and external, access
 2612 data in the same way. For example, an [Astronomical](#)
 2613 [Data Query Language \(IVOA standard\) \(ADQL\)](#) query
 2614 on the [Object](#) catalog via [TAP](#) yields identical results
 2615 whether run from the [Portal](#), [Notebook](#), or an external
 2616 client.

2617 The following [IVOA](#) services are available at the time
 2618 of the DP1 release:

- 2619 • **Table Access Protocol (TAP) Service:** A
 2620 [TAP](#) service ([P. Dowler et al. 2019](#)) enables queries
 2621 of catalog data via the [IVOA](#)-standard [ADQL](#), a
 2622 dialect of [SQL92](#) with spherical geometry exten-
 2623 sions. The main [TAP](#) service for [DP1](#) runs on the
 2624 Rubin-developed [Qserv](#) database ([§ 6.5](#)), which
 2625 hosts the core science tables described in [§3.2](#), as
 2626 well as the [Visit](#) database. It also provides image
 2627 metadata in the [IVOA](#) [ObsCore](#) format via the
 2628 standard [ivoa.ObsCore](#) table, making it an “Ob-
 2629 sTAP” service ([ObsTAP](#); [M. Louys et al. 2017](#)).
 2630 The [TAP](#) service is based on the [Canadian Astro-
 2631 nomy Data Centre \(CADC\)](#)’s open-source Java
 2632 [TAP](#) implementation¹⁰¹, modified for the exact
 2633 query language accepted by [Qserv](#). It currently
 2634 supports a large subset of [ADQL](#), with limitations
 2635 documented in the data release materials (see [§7.1](#))
 2636 and exposed via the [TAP](#) **capabilities** endpoint
 2637 where possible.

2638 The [TAP](#) service provides metadata annotations
 2639 consistent with the standard, including table and
 2640 column descriptions, indications of foreign-key re-
 2641 lationships between tables, and column metadata
 2642 such as units and [IVOA](#) Unified Content Descrip-
 2643 tors (UCDs).

- 2644 • **Image Access Services:** Rubin image access
 2645 services are compliant with [IVOA](#) [SIAv2](#) (Sim-
 2646 ple Image Access Protocol, version 2; [T. Jenness](#)
 2647 et al. 2024; [P. Dowler et al. 2015](#)) for discovering
 2648 and accessing astronomical images based on [meta-
 2649 data](#). [SIAv2](#) is a [REpresentational State Transfer
 2650 \(REST\)](#)-based protocol designed for the discovery
 2651 and retrieval of image data. It allows, for instance,
 2652 querying all images in a given band over a defined
 2653 sky region and time period.

2654 Users identify an image or observation of inter-
 2655 est and query the service. The result set includes
 2656 [metadata](#) about the image, such as the sky pos-
 2657 ition, time, or band, and a data access URL, which
 2658 includes an [IVOA](#) Identifier uniquely identifying
 2659 the dataset ([T. Jenness & G. P. Dubois-Felmann](#)
 2660 [2025](#)), allowing the dataset to be retrieved or a
 2661 cutout requested via [Server-side Operations for](#)
 2662 [Data Access \(IVOA standard\)](#) ([SODA](#)).

101 <https://github.com/opencadc/tap>

- **Image Cutout Service:** The Rubin Cutout Service (R. Allbery 2023, 2024) is based on the IVOA SODA standard (F. Bonnarel et al. 2017). Users submit requests specifying sky coordinates and the cutout size as the radius from the coordinates, and the service performs the operation on the full image and returns a result set. For DP1, the cutout service is a single cutout service only where N cutout requests will require N independent synchronous calls. We expect some form of bulk cutout service by mid 2026.
- **HiPS Data Service:** An authenticated HiPS (P. Fernique et al. 2017) data service for seamless pan-and-zoom access to large-scale co-adds. It supports fast interactive progressive image exploration at a range of resolutions.
- **WebDAV:** A Web Distributed Authoring and Versioning (WebDav) service is provided to enable users to remotely manage, edit, and organize files and directories on the RSP as if they were local files on their own computer. This is especially useful for local development.

6.2.2. Data Butler

The Rubin Data Butler (T. Jenness et al. 2022; N. B. Lust et al. 2023), is a high-level interface designed to facilitate seamless access to data for both users and software systems. This includes managing storage formats, physical locations, data staging, and database mappings. A Butler repository contains two components:

- the *Data Store*: A physical storage system for datasets, e.g., a Portable Operating System Interface (POSIX) file system or S3 object store; and
- the *Registry*: An Structured Query Language (SQL)-compatible database that stores metadata about the datasets in the data store.

For DP1, the Butler repository is hosted in the Google Cloud, using an (Amazon) Simple Storage Service (S3)-compatible store for datasets and AlloyDB, a PostgreSQL-compatible database, for the registry.

In the context of the Butler, a *dataset* refers to a unique data product, such as an image, catalog or map, generated by the observatory or processing pipelines. Datasets belong to one of the various types of data products, described in §3. The Butler ensures that each dataset is uniquely identifiable by a combination of three pieces of information: a data coordinate, a dataset type, and a run collection. For example,

a dataset that represents a single raw image in the *i* band taken on the night starting 2024-11-11 with exposure ID 2024111100074 would be represented as `dataId='exposure':2024111100074, 'band':'i', 'instrument':'LSSTComCam'` and is associated with the `raw` DatasetType. For a deep coadd on a `patch` of sky in the Seagull field, there would be no exposure dimensions and instead the tract, `patch` and band would be specified as `dataId='tract':7850, 'patch':6, 'band':'g', 'instrument':'LSSTComCam', skymap='lsst_cells_v1'` and is associated with the `deep_coadd` DatasetType.

The data coordinate is used to locate a dataset in multi-dimensional space, where dimensions are defined in terms of scientifically meaningful concepts, such as instrument, visit, detector or band. For example, a calibrated single-visit image (§3.1) has dimensions including band, instrument, and detector. In contrast, the visit table (§3.2), a catalog of all calibrated single-epoch visits in DP1, has only the instrument dimension. The main dimensions used in DP1 are listed, together with a brief description, in Table 6. To determine which dimensions are relevant for a specific dataset, the Butler defines dataset types, which associate each dataset with its specific set of relevant dimensions, as well as the associated Python type representing the dataset. The dataset type defines the kind of data a dataset represents, such as a raw image (`raw`), a processed catalog (`object_forced_source`), or a sky map (`skyMap`). Table 7 lists all the dataset types available via the Butler in DP1, together with the dimensions needed to uniquely identify a specific dataset and the number of unique datasets of each type.

It is important to highlight a key difference between accessing catalog data via the TAP service versus the Butler. While the TAP service contains entire catalogs, many of the same catalogs in the Butler are split into multiple separate catalogs. This is partly due to how these catalogs are generated, but also because of the way data is stored within and retrieved from the Butler repository – it is inefficient to retrieve the entire `Source` catalog, for example, from the file system. Instead, because the `Source` catalog contains data for sources detected in the `visit_images`, there is one `Source` catalog in the Butler for each `visit_image`. Similarly, there is one `Object` catalog for each `deep_coadd`. All the catalogs described in §3.2, aside from the `CcdVisit`, `SSObject`, `SSSource`, and `Calibration` catalogs, are split within the Butler.

A dataset is associated with one or more *Collections*; logical groupings of datasets within the Butler system that were created or processed together by the same

Table 6. Descriptions of and valid values for the key data dimensions in DP1. YYYYMMDD signifies date and # signifies a single 0–9 digit.

Dimension	Format/Valid values	Description
day_obs	YYYYMMDD	A day and night of observations that rolls over during daylight hours.
visit	YYYYMMDD#####	A sequence of observations processed together; synonymous with “exposure” in DP1.
exposure	YYYYMMDD#####	A single exposure of all nine ComCam detectors.
instrument	LSSTComCam	The instrument name.
detector	0–8	A ComCam detector.
skymap	lsst_cells_v1	A set of tracts and patches that subdivide the sky into rectangular regions with simple projections and intentional overlaps.
tract	See Table 3	A large rectangular region of the sky.
patch	0–99	A rectangular region within a tract.
physical_filter	u_02, g_01, i_06, r_03, z_03, y_04	A physical filter.
band	u, g, r, i, z, y	An conceptual astronomical passband.

Table 7. The name and number of each type of data product in the Butler and the dimensions required to identify a specific dataset.

Data Product	Name in Butler	Required Dimensions	Number in DP1
Image Data Products			
raw	raw	instrument, detector, exposure	16125
visit_image	visit_image	instrument, detector, visit	15972
deep_coadd	deep_coadd	band, skymap, tract, patch	2644
template_coadd	template_coadd	band, skymap, tract, patch	2730
difference_image	difference_image	instrument, detector, visit	15972
Catalog Data Products			
Source	source	instrument, visit	1786
Object	object	skymap, tract	29
ForcedSource	object_forced_source	skymap, tract, patch	636
DiaSource	dia_source	skymap, tract	25
DiaObject	dia_object	skymap, tract	25
ForcedSourceOnDiaObject	dia_object_forced_source	skymap, tract, patch	597
SSSource	ss_source	—	1
SSObject	ss_object	—	1
Visit	visit_table	instrument	1
CCDVisit	visit_detector_table	instrument	1

batch operation. Collections allow multiple datasets with the same data coordinate to coexist without conflict. Collections support flexible, parallel processing by enabling repeated analyses of the same input data using different configurations.

For DP1, a subset of the consolidated database contents (§6.5.2) is accessible through the Data Butler. However, not all metadata from the Visit table (§3.5)

are available. The DP1 Butler is read-only; a writeable Butler is expected by mid-2026.

6.2.3. Remote Programmatic Access

The Rubin RSP API can be accessed from a local system by data rights holders outside of the RSP, by creating a user security token. This token can then be used as a bearer token for API calls to the RSP TAP service.

2779 This capability is especially useful for remote data analysis
 2780 using tools such as [TOPCAT](#), as well as enabling
 2781 third-party systems, e.g., Community Alert Brokers, to
 2782 access Rubin data. Additionally, it supports remote de-
 2783 velopment, allowing for more flexible workflows and in-
 2784 tegration with external systems.

2785 6.3. *Portal Aspect*

2786 The Portal Aspect provides an interactive web-based
 2787 environment for exploratory data discovery, filtering,
 2788 querying, and visualization of both image and catalog
 2789 data, without requiring programming expertise. It en-
 2790 ables users to access and analyze large datasets via tools
 2791 for catalog queries, image browsing, time-series inspec-
 2792 tion, and cross-matching.

2793 The Portal is built on [Firefly](#) (X. Wu et al. 2019),
 2794 a web application framework developed by the Infrared
 2795 Processing and Analysis Center (IPAC). [Firefly](#) provides
 2796 interactive capabilities such as customizable table views,
 2797 image overlays, multi-panel visualizations, and synchro-
 2798 nized displays linking catalog and image data.

2799 Designed to support both exploratory data access and
 2800 detailed scientific investigation, the Portal delivers an
 2801 intuitive user experience, allowing users to visually ana-
 2802 lyze data while retaining access to underlying metadata
 2803 and query controls.

2804 6.4. *Notebook Aspect*

2805 The Notebook Aspect provides an interactive, web-
 2806 based environment built on Jupyter Notebooks, en-
 2807 abling users to write and execute Python code directly
 2808 on Rubin and [LSST](#) data without downloading it locally.
 2809 It offers programmatic access to Rubin and LSST data
 2810 products, allowing users to query and retrieve datasets,
 2811 manipulate and display images, compute derived prop-
 2812 erties, plot results, and reprocess data using the LSST
 2813 Science Pipelines (§4.1). The environment comes pre-
 2814 installed with the pipelines and a broad set of widely
 2815 used astronomical software tools, supporting immediate
 2816 and flexible data analysis.

2817 6.5. *Databases*

2818 The user-facing Aspects of the [RSP](#) are supported by
 2819 several backend databases that store catalog data prod-
 2820 ucts, image metadata, and other derived datasets. The
 2821 schema for DP1 and other Rubin databases are available
 2822 online at <https://sdm-schemas.lsst.io>.

2823 6.5.1. *Qserv*

2824 The final 10-year [LSST](#) catalog is expected to reach
 2825 15 PB and contain measurements for billions of stars
 2826 and galaxies across trillions of detections. To support

2827 efficient storage, querying, and analysis of this dataset,
 2828 Rubin Observatory developed Qserv (D. L. Wang et al.
 2829 2011; F. Mueller et al. 2023) – a scalable, parallel, dis-
 2830 tributed SQL database system. [Qserv](#) partitions data
 2831 over approximately equal-area regions of the celestial
 2832 sphere, replicates data to ensure resilience and high
 2833 availability, and uses shared scanning to reduce overall
 2834 I/O load. It also supports a package of scientific user-
 2835 defined functions (SciSQL: <https://smonkewitz.github.io/scisql/>) simplifying complex queries involving spher-
 2836 ical geometry, statistics, and photometry. [Qserv](#) is
 2837 built on robust production-quality components, includ-
 2838 ing MariaDB (<https://www.mariadb.org/>) and XRootD
 2839 (<https://xrootd.org/>). Qserv runs at the [USDF](#) and user
 2840 access to catalog data is via the TAP service (§6.2.1).
 2841 This enables catalog-based analysis through both the
 2842 [RSP](#) Portal and Notebook Aspects.

2843 Although the small [DP1](#) dataset does not require
 2844 Qserv’s full capabilities, we nevertheless chose to use
 2845 it for [DP1](#) to accurately reflect the future data access
 2846 environment and to gain experience with scientifically-
 2847 motivated queries ahead of full-scale deployment. [Qserv](#)
 2848 is open-source and available on GitHub: <https://github.com/lsst/qserv>.

2851 6.5.2. *Consolidated Database*

2852 The Consolidated Database (ConsDB) (K.-T. Lim
 2853 2025) is an SQL-compatible database designed to store
 2854 and manage metadata for Rubin Observatory science
 2855 and calibration images. Metadata are recorded on a per-
 2856 exposure basis and includes information such as the tar-
 2857 get name, pointing coordinates, observation time, physi-
 2858 cal filter and band, exposure duration, and environmen-
 2859 tal conditions (e.g., temperature, humidity, and wind
 2860 speed). These key image metadata are also stored in
 2861 the Butler Registry (§6.2.2), however the ConsDB stores
 2862 additional information including derived metrics from
 2863 image processing and information from the [Engineering](#)
 2864 and [Facility Database \(EFD\)](#) transformed from the time
 2865 dimension to the exposure dimension.

2866 The ConsDB schema is organized into instrument-
 2867 specific tables, e.g., [LSSTComCam](#) and LSSTCam, fa-
 2868 cilitating instrument-specific queries. Within the [LSST-](#)
 2869 [ComCam](#) schema, data is further structured into ta-
 2870 bles for individual exposures and detectors. An example
 2871 query on the [DP1](#) dataset might retrieve all visits within
 2872 a specified time range in the r-band for a given [DP1](#) tar-
 2873 get.

2874 The ConsDB is hosted at the [USDF](#). Following the
 2875 initial release of DP1, a release of the DP1 exposure-
 2876 specific ConsDB data will be made available through the
 2877 [RSP](#), and accessible externally via TAP. The detailed

2878 LSSTComCam schema can be found at: [https://sdm-
2879 schemas.lsst.io/cdb_lsstcomcam.html](https://sdm-schemas.lsst.io/cdb_lsstcomcam.html)

2880 7. SUPPORT FOR COMMUNITY SCIENCE

2881 The Rubin Observatory has a science community that
2882 encompasses thousands of individuals worldwide, with
2883 a broad range of experience and expertise in astronomy
2884 in general, and in the analysis of optical imaging data
2885 specifically.

2886 Rubin’s model to support this diverse community to
2887 access and analyze DP1 emphasizes self-help via docu-
2888 mentation and tutorials, and employs an open platform
2889 for asynchronous issue reporting that enables crowd-
2890 sourced solutions. These two aspects of community sup-
2891 port are augmented by virtual engagement activities. In
2892 addition, Rubin supports its Users Committee to advo-
2893 cate on behalf of the science community, and supports
2894 the eight LSST Science Collaborations (§7.6).

2895 All of the resources for scientists that are discussed in
2896 this section are discoverable by browsing the For Scien-
2897 tists pages of the Rubin Observatory website¹⁰².

2908 7.1. Documentation

2909 The data release documentation for DP1¹⁰³ provides
2910 an overview of the LSSTComCam observations, detailed
2911 descriptions of the data products, and a high-level sum-
2912 mary of the processing pipelines. Although much of its
2913 content overlaps significantly with this paper, the doc-
2914 umentation is presented as a searchable, web-based re-
2915 source built using Sphinx¹⁰⁴, with a focus on enabling
2916 scientific use of the data products.

2907 7.2. Tutorials

2908 A suite of tutorials (N.-D. V. C. R. Observatory 2021)
2909 that demonstrate how to access and analyze DP1 using
2910 the RSP accompanies the DP1 release¹⁰⁵. Jupyter Note-
2911 book tutorials are available via the “Tutorials” drop-
2912 down menu within the Notebook aspect of the RSP.
2913 Tutorials for the Portal and API aspects of the RSP can
2914 be found in the data release documentation.

2915 These tutorials are designed to be inclusive, accessible,
2916 clear, focused, and consistent. Their format and
2917 contents follow a set of guidelines (M. L. Graham et al.
2918 2025) that are informed by modern standards in tech-
2919 nical writing.

2921 7.3. Community Forum

2922 The venue for all user support is the Rubin Commu-
2923 nity Forum¹⁰⁶.

2924 Questions about any and all aspects of the Rubin
2925 data products, pipelines, and services – including DP1
2926 – should be posted as new topics in the Support cate-
2927 gory. This includes beginner-level and “how-to” ques-
2928 tions, advanced scientific analysis questions, technical
2929 bug reports, account and data access issues, and every-
2930 thing in between. The Support category of the Forum
2931 is monitored by Rubin staff, who follow an established
2932 internal workflow for following-up and resolving all re-
2933 ported issues.

2934 The Rubin Community Forum is built on the open-
2935 source Discourse platform. It was chosen because, for
2936 a worldwide community of ten thousand Rubin users, a
2937 traditional (i.e., closed) help desk represents a risk to
2938 Rubin science (e.g., many users with the same question
2939 having to wait for responses). The open nature of the
2940 Forum enables self-help by letting users search for sim-
2941 ilar issues, and enables crowd-sourced problem solving
2942 (and avoids knowledge bottlenecks) by letting users help
2943 users.

2944 The Rubin Community Forum, and the internal staff
2945 workflows for user support, were set up, tested, and re-
2946 fined with /glsDP0 so that it was ready for use with
2947 DP1.

2947 7.4. Engagement Activities

2948 A variety of live virtual and in-person workshops and
2949 seminars offer learning opportunities to scientists and
2950 students working with the Rubin data products, ser-
2951 vices, and tools.

- 2952 • Rubin Science Assemblies (weekly, virtual, 1
2953 hour): alternates between hands-on tutorials
2954 based on the most recent data release and open
2955 drop-in “office hours” with Rubin staff.
- 2956 • Rubin Data Academy (annual, virtual, 3-4 days):
2957 an intense set of hands-on tutorials based on the
2958 most recent data release, along with co-working
2959 and networking sessions.
- 2960 • Rubin Community Workshop (annual, virtual, 5
2961 days), a science-focused conference of contributed
2962 posters, talks, and sessions led by members of the
2963 Rubin science community and Rubin staff.

2964 Following the release of DP1, all of these engagement
2965 activities focused on use of DP1 by the science commu-

¹⁰² <https://rubinobservatory.org/for-scientists>

¹⁰³ <https://dp1.lsst.io>

¹⁰⁴ <https://www.sphinx-doc.org/>

¹⁰⁵ <https://dp1.lsst.io/tutorials>

¹⁰⁶ <https://community.lsst.org/>

2966 nity. In particular, the 2025 Rubin Data Academy was
 2967 run the week of the [DP1](#) release, in order to immediately
 2968 facilitate community access. The 2025 Rubin Commu-
 2969 nity Workshop had several sessions to introduce people
 2970 to the [DP1](#) dataset and demonstrate how to access and
 2971 analyze it with the [RSP](#).

2972 For schedules, connection information, zoom record-
 2973 ings, and associated materials, visit the For Scientists
 2974 pages of the Rubin Observatory website¹⁰⁷. Requests for
 2975 custom tutorials and presentations for research groups
 2976 are also accommodated.

2977 7.5. *Users Committee*

2978 This committee is charged with soliciting feedback
 2979 from the science community, advocating on their behalf,
 2980 and recommending science-driven improvements to the
 2981 [LSST](#) data products and the Rubin Science Platform
 2982 tools and services. Community members are encour-
 2983 aged to attend their virtual meetings and raise issues
 2984 to their attention, so they can be included in the com-
 2985 mittee’s twice-yearly reports to the Rubin Observatory
 2986 Director.

2987 Like the Forum, the Users Committee was established
 2988 and began its work with [DP0](#), and that feedback was
 2989 implemented for [DP1](#). The community’s response to
 2990 [DP1](#) will be especially valuable input to [DP2](#) and [Data](#)
 2991 [Release 1 \(DR1\)](#), and the Users Committee encourages
 2992 all users to interact with them. For a list of members
 2993 and contact information, visit the For Scientists pages
 2994 of the Rubin Observatory website.

2995 7.6. *Science Collaborations*

2996 The eight [LSST](#) Science Collaborations are inde-
 2997 pendent, worldwide communities of scientists, self-organized
 2998 into collaborations based on their research interests and
 2999 expertise. Members work together to apply for funding,
 3000 build software infrastructure and analysis algorithms,
 3001 and incorporate external data sets into their [LSST](#)-
 3002 based research.

3003 The Science Collaborations also provide valuable ad-
 3004 vice to Rubin Observatory on the operational strategies
 3005 and data products to accomplish specific science goals,
 3006 and Rubin Observatory supports the collaborations via
 3007 staff liaisons and regular virtual meetings with Rubin
 3008 operations leadership.

3009 The Science Collaborations have been functioning for
 3010 many years, and their engagement and feedback on [DP0](#)
 3011 was implemented into the community science model for
 3012 [DP1](#), as it will for future data releases.

¹⁰⁷ <https://rubinobservatory.org/for-scientists/events-deadlines>

3013 8. SUMMARY AND FUTURE RELEASES

3014 Rubin Data Preview 1 ([DP1](#)) offers an initial look at
 3015 the first on-sky data products and access services from
 3016 the Vera C. Rubin Observatory. [DP1](#) forms part of Ru-
 3017 bin’s Early Science Program, and provides the sci-
 3018 entific community with an early opportunity to familiarize
 3019 themselves with the data formats and access infrastruc-
 3020 ture for the forthcoming Legacy Survey of Space and
 3021 Time. This early release has a proprietary period of two
 3022 years, during which time it is available to Rubin data
 3023 rights holders only via the cloud-based Rubin Science
 3024 Platform ([RSP](#)).

3025 In this paper we have described the completion status
 3026 of the observatory at the time of data acquisition, the
 3027 commissioning campaign that forms the basis of [DP1](#),
 3028 and the processing pipelines used to produce early ver-
 3029 sions of data products. We provide details on the data
 3030 products, their characteristics and known issues, and
 3031 describe the Rubin Science Platform for access to and
 3032 analysis of [DP1](#).

3033 The data products described in this paper derive from
 3034 observations obtained by [LSSTComCam](#). [LSSTCom](#)
 3035 [Cam](#) contains only around 5% the number of CCDs as
 3036 the full LSST Science Camera (LSSTCam), yet the [DP1](#)
 3037 dataset that it has produced will already enable a very
 3038 broad range of science. At 3.5 TB in size, [DP1](#) covers
 3039 a total area of $\sim 15 \text{ deg}^2$ and contains 1792 single-epoch
 3040 images, 2644 deep coadded images and 2.3 million dis-
 3041 tinct astrophysical objects, including 93 new asteroid
 3042 discoveries.

3043 While some data products anticipated from the LSST
 3044 are not yet available, e.g., cell-based coadds, [DP1](#) in-
 3045 cludes several products that will not be provided in fu-
 3046 ture releases. Notably, difference images are included in
 3047 [DP1](#) as pre-generated products; in future releases, these
 3048 will instead be generated on demand via dedicated ser-
 3049 vices. The inclusion of pre-generated difference images
 3050 in [DP1](#) is feasible due to the relatively small size of the
 3051 dataset, an approach that will not scale to the signifi-
 3052 cantly larger data volumes expected in subsequent re-
 3053 leases.

3054 The [RSP](#) is continually under development, and new
 3055 functionality will continue to be deployed incrementally
 3056 as it becomes available, and independent of the future
 3057 data release schedule. User query history capabilities,
 3058 context-aware documentation and a bulk cutout services
 3059 are just a few of the services currently under develop-
 3060 ment.

3061 Coincident with the release of [DP1](#), Rubin Obser-
 3062 vatory begins its Science Validation Surveys with the
 3063 LSST Science Camera. This final commissioning phase
 3064 will produce a dataset that will form the foundation for

3065 the second Rubin Data Preview, DP2. Full operations, 3081 marking the start of the LSST, are expected to com-
 3066 mence in 2026. 3082
 3067

3083 This work has been supported by the French Na-
 3084 tional Institute of Nuclear and Particle Physics (IN2P3)
 3085 through dedicated funding provided by the National
 3086 Center for Scientific Research (CNRS).
 3087

3088 This work has been supported by STFC fund-
 3089 ing for UK participation in LSST, through grant
 3090 ST/Y00292X/1.

3068 ACKNOWLEDGMENTS

3069 . This material is based upon work supported in part by
 3070 the National Science Foundation through Cooperative
 3071 Agreements AST-1258333 and AST-2241526 and Co-
 3072 operative Support Agreements AST-1202910 and AST-
 3073 2211468 managed by the Association of Universities for
 3074 Research in Astronomy (AURA), and the Department of
 3075 Energy under Contract No. DE-AC02-76SF00515 with
 3076 the SLAC National Accelerator Laboratory managed
 3077 by Stanford University. Additional Rubin Observatory
 3078 funding comes from private donations, grants to univer-
 3079 sities, and in-kind support from LSST-DA Institutional
 3080 Members.

3088 *Facilities:* Rubin:Simonyi (LSSTComCam), Ru-
 3089 bin:USDAC

3090 *Software:* Rubin Data Butler (T. Jenness et al.
 3091 2022), LSST Science Pipelines (Rubin Observatory Sci-
 3092 ence Pipelines Developers 2025), LSST Feature Based
 3093 Scheduler v3.0 (P. Yoachim et al. 2024; E. Naghib et al.
 3094 2019) Astropy (Astropy Collaboration et al. 2013, 2018,
 3095 2022) PIFF (M. Jarvis et al. 2021), GBDES (G. M.
 3096 Bernstein 2022), Qserv (D. L. Wang et al. 2011; F.
 3097 Mueller et al. 2023), Slurm, HTCondor, CVMFS, FTS3,
 3098 ESNet

3099 APPENDIX

REFERENCES

3100 Abazajian, K., Adelman-McCarthy, J. K., Agüeros, M. A., 3121 Antilogus, P., Astier, P., Doherty, P., Guyonnet, A., &
 3101 et al. 2004, AJ, 128, 502, doi: [10.1086/421365](https://doi.org/10.1086/421365) 3122 Regnault, N. 2014, Journal of Instrumentation, 9,
 3102 Ahumada, R., Allende Prieto, C., Almeida, A., et al. 2020, 3123 C03048, doi: [10.1088/1748-0221/9/03/C03048](https://doi.org/10.1088/1748-0221/9/03/C03048)
 3103 ApJS, 249, 3, doi: [10.3847/1538-4365/ab929e](https://doi.org/10.3847/1538-4365/ab929e) 3124 Astropy Collaboration, Robitaille, T. P., Tollerud, E. J.,
 3104 Aihara, H., AlSayyad, Y., Ando, M., et al. 2022, PASJ, 74, 3125 et al. 2013, A&A, 558, A33,
 3105 247, doi: [10.1093/pasj/psab122](https://doi.org/10.1093/pasj/psab122) 3126 doi: [10.1051/0004-6361/201322068](https://doi.org/10.1051/0004-6361/201322068)
 3106 Allbery, R. 2023, IVOA SODA implementation experience, 3127 Astropy Collaboration, Price-Whelan, A. M., Sipőcz, B. M.,
 3107 SQuaRE Technical Note SQR-063, NSF-DOE Vera C. 3128 et al. 2018, AJ, 156, 123, doi: [10.3847/1538-3881/aabc4f](https://doi.org/10.3847/1538-3881/aabc4f)
 3108 Rubin Observatory. <https://sqr-063.lsst.io/> 3129 Astropy Collaboration, Price-Whelan, A. M., Lim, P. L.,
 3109 Allbery, R. 2024, Draft IVOA SODA web service 3130 et al. 2022, ApJ, 935, 167, doi: [10.3847/1538-4357/ac7c74](https://doi.org/10.3847/1538-4357/ac7c74)
 3110 specification, SQuaRE Technical Note SQR-093, 3131 Baumann, M., Boch, T., Pineau, F.-X., et al. 2022, in
 3111 NSF-DOE Vera C. Rubin Observatory. 3132 Astronomical Society of the Pacific Conference Series,
 3112 <https://sqr-093.lsst.io/> 3133 Vol. 532, Astronomical Data Analysis Software and
 3113 AlSayyad, Y. 2018, Coaddition Artifact Rejection and 3134 Systems XXX, ed. J. E. Ruiz, F. Pierfederici, &
 3114 CompareWarp, Data Management Technical Note 3135 P. Teuben, 7
 3115 DMTN-080, NSF-DOE Vera C. Rubin Observatory, 3136 Bechtol, K., Sevilla-Noarbe, I., Drlica-Wagner, A., et al.
 3116 doi: [10.71929/rubin/2583441](https://doi.org/10.71929/rubin/2583441) 3137 2025, arXiv e-prints, arXiv:2501.05739,
 3117 Ansel, J., Yang, E., He, H., et al. 2024, in 29th ACM 3138 doi: [10.48550/arXiv.2501.05739](https://doi.org/10.48550/arXiv.2501.05739)

3139 Berk, A., Anderson, G. P., Bernstein, L. S., et al. 1999, in
 3140 Society of Photo-Optical Instrumentation Engineers
 3141 (SPIE) Conference Series, Vol. 3756, Optical
 3142 Spectroscopic Techniques and Instrumentation for
 3143 Atmospheric and Space Research III, ed. A. M. Larar,
 3144 348–353, doi: [10.1111/12.366388](https://doi.org/10.1111/12.366388)

3145 Bernstein, G. M. 2022, gbdes: DECam instrumental
 3146 signature fitting and processing programs,, *Astrophysics*
 3147 *Source Code Library*, record ascl:2210.011
<http://ascl.net/2210.011>

3148 Bernstein, G. M., & Jarvis, M. 2002, *AJ*, 123, 583,
 3149 doi: [10.1086/338085](https://doi.org/10.1086/338085)

3150 Bernstein, G. M., Armstrong, R., Plazas, A. A., et al. 2017,
 3151 *PASP*, 129, 074503, doi: [10.1088/1538-3873/aa6c55](https://doi.org/10.1088/1538-3873/aa6c55)

3152 Bertin, E. 2011, in *Astronomical Society of the Pacific*
 3153 Conference Series, Vol. 442, *Astronomical Data Analysis*
 3154 *Software and Systems XX*, ed. I. N. Evans,
 3155 A. Accomazzi, D. J. Mink, & A. H. Rots, 435

3156 Bianco, F. B., Ivezić, Ž., Jones, R. L., et al. 2022, *ApJS*,
 3157 258, 1, doi: [10.3847/1538-4365/ac3e72](https://doi.org/10.3847/1538-4365/ac3e72)

3158 Blum, R., & the Rubin Operations Team. 2020, *Vera C.*
 3159 *Rubin Observatory Data Policy, Data Management*
 3160 *Operations Controlled Document RDO-013*, NSF-DOE
 3161 *Vera C. Rubin Observatory*. <https://ls.st/RDO-013>

3162 Boch, T., & Fernique, P. 2014, in *Astronomical Society of*
 3163 *the Pacific Conference Series*, Vol. 485, *Astronomical*
 3164 *Data Analysis Software and Systems XXIII*, ed.
 3165 N. Manset & P. Forshay, 277

3166 Bonnarel, F., Dowler, P., Demleitner, M., Tody, D., &
 3167 Dempsey, J. 2017, *IVOA Server-side Operations for Data*
 3168 *Access Version 1.0.*, *IVOA Recommendation 17 May 2017*
 3169 doi: [10.5479/ADS/bib/2017ivoa.spec.0517B](https://doi.org/10.5479/ADS/bib/2017ivoa.spec.0517B)

3170 Bonnarel, F., Fernique, P., Bienaymé, O., et al. 2000,
 3171 *A&AS*, 143, 33, doi: [10.1051/aas:2000331](https://doi.org/10.1051/aas:2000331)

3172 Bosch, J., Armstrong, R., Bickerton, S., et al. 2018, *PASJ*,
 3173 70, S5, doi: [10.1093/pasj/psx080](https://doi.org/10.1093/pasj/psx080)

3174 Broughton, A., Utsumi, Y., Plazas Malagón, A. A., et al.
 3175 2024, *PASP*, 136, 045003, doi: [10.1088/1538-3873/ad3aa2](https://doi.org/10.1088/1538-3873/ad3aa2)

3176 Burke, D. L., Rykoff, E. S., Allam, S., et al. 2018, *AJ*, 155,
 3177 41, doi: [10.3847/1538-3881/aa9f22](https://doi.org/10.3847/1538-3881/aa9f22)

3178 Chambers, K. C., Magnier, E. A., Metcalfe, N., et al. 2016,
 3179 *arXiv e-prints*, arXiv:1612.05560,
 3180 doi: [10.48550/arXiv.1612.05560](https://doi.org/10.48550/arXiv.1612.05560)

3181 Choi, Y., Olsen, K. A. G., Carlin, J. L., et al. 2025, *arXiv*
 3182 *e-prints*, arXiv:2507.01343,
 3183 doi: [10.48550/arXiv.2507.01343](https://doi.org/10.48550/arXiv.2507.01343)

3184 de Vaucouleurs, G. 1948, *Annales d’Astrophysique*, 11, 247

3185 de Vaucouleurs, G. 1953, *MNRAS*, 113, 134,
 3186 doi: [10.1093/mnras/113.2.134](https://doi.org/10.1093/mnras/113.2.134)

3187 Dowler, P., Bonnarel, F., & Tody, D. 2015, *IVOA Simple*
 3188 *Image Access Version 2.0.*, *IVOA Recommendation 23*
 3189 December 2015
 3190 doi: [10.5479/ADS/bib/2015ivoa.spec.1223D](https://doi.org/10.5479/ADS/bib/2015ivoa.spec.1223D)

3191 Dowler, P., Rixon, G., Tody, D., & Demleitner, M. 2019,
 3192 *Table Access Protocol Version 1.1.*, *IVOA*
 3193 *Recommendation 27 September 2019*
 3194 doi: [10.5479/ADS/bib/2019ivoa.spec.0927D](https://doi.org/10.5479/ADS/bib/2019ivoa.spec.0927D)

3195 Eggel, S., Juric, M., Moeyens, J., & Jones, L. 2020, in
 3196 *AAS/Division for Planetary Sciences Meeting Abstracts*,
 3197 Vol. 52, *AAS/Division for Planetary Sciences Meeting*
 3198 *Abstracts*, 211.01

3199 Esteves, J. H., Utsumi, Y., Snyder, A., et al. 2023, *PASP*,
 3200 135, 115003, doi: [10.1088/1538-3873/ad0a73](https://doi.org/10.1088/1538-3873/ad0a73)

3201 Euclid Collaboration, Romelli, E., Kümmel, M., et al. 2025,
 3202 *arXiv e-prints*, arXiv:2503.15305,
 3203 doi: [10.48550/arXiv.2503.15305](https://doi.org/10.48550/arXiv.2503.15305)

3204 Fagrelius, P., & Rykoff, E. S. 2025, *Rubin Observatory*
 3205 *Baseline Calibration Plan, Commissioning Technical*
 3206 *Note SITCOMTN-086*, NSF-DOE *Vera C. Rubin*
 3207 *Observatory*, doi: [10.71929/rubin/2583850](https://doi.org/10.71929/rubin/2583850)

3208 Ferguson, P. S., Rykoff, E. S., Carlin, J. L., Saunders, C., &
 3209 Parejko, J. K. 2025, *The Monster: A reference catalog*
 3210 with synthetic ugrizy-band fluxes for the *Vera C. Rubin*
 3211 *observatory*, *Data Management Technical Note*
 3212 *DMTN-277*, NSF-DOE *Vera C. Rubin Observatory*,
 3213 doi: [10.71929/rubin/2583688](https://doi.org/10.71929/rubin/2583688)

3214 Fernique, P., Allen, M. G., Boch, T., et al. 2015, *A&A*, 578,
 3215 A114, doi: [10.1051/0004-6361/201526075](https://doi.org/10.1051/0004-6361/201526075)

3216 Fernique, P., Allen, M., Boch, T., et al. 2017, *HiPS -*
 3217 *Hierarchical Progressive Survey Version 1.0.*, *IVOA*
 3218 *Recommendation 19 May 2017*
 3219 doi: [10.5479/ADS/bib/2017ivoa.spec.0519F](https://doi.org/10.5479/ADS/bib/2017ivoa.spec.0519F)

3220 Fortino, W. F., Bernstein, G. M., Bernardinelli, P. H., et al.
 3221 2021, *AJ*, 162, 106, doi: [10.3847/1538-3881/ac0722](https://doi.org/10.3847/1538-3881/ac0722)

3222 Gaia Collaboration, Montegriffo, P., Bellazzini, M., et al.
 3223 2023a, *A&A*, 674, A33,
 3224 doi: [10.1051/0004-6361/202243709](https://doi.org/10.1051/0004-6361/202243709)

3225 Gaia Collaboration, Vallenari, A., Brown, A. G. A., et al.
 3226 2023b, *A&A*, 674, A1, doi: [10.1051/0004-6361/202243940](https://doi.org/10.1051/0004-6361/202243940)

3227 Górski, K. M., Hivon, E., Banday, A. J., et al. 2005, *ApJ*,
 3228 622, 759, doi: [10.1086/427976](https://doi.org/10.1086/427976)

3229 Graham, A. W., & Driver, S. P. 2005, *PASA*, 22, 118,
 3230 doi: [10.1071/AS05001](https://doi.org/10.1071/AS05001)

3231 Graham, M., Plante, R., Tody, D., & Fitzpatrick, M. 2014,
 3232 *PyVO: Python access to the Virtual Observatory*,
 3233 *Astrophysics Source Code Library*, record ascl:1402.004

3234

3235 Graham, M. L., Carlin, J. L., Adair, C. L., et al. 2025,
 3236 Guidelines for User Tutorials, Technical Note RTN-045,
 3237 NSF-DOE Vera C. Rubin Observatory,
 3238 doi: [10.71929/rubin/2584020](https://doi.org/10.71929/rubin/2584020)

3239 Gray, B. 2025, *find_orb*: Orbit determination from
 3240 observations, https://github.com/Bill-Gray/find_orb

3241 Guy, L. P., Bechtol, K., Bellm, E., et al. 2025, Rubin
 3242 Observatory Plans for an Early Science Program,
 3243 Technical Note RTN-011, NSF-DOE Vera C. Rubin
 3244 Observatory, doi: [10.71929/rubin/2584021](https://doi.org/10.71929/rubin/2584021)

3245 Heinze, A., Eggel, S., Juric, M., et al. 2022, in AAS/Division
 3246 for Planetary Sciences Meeting Abstracts, Vol. 54,
 3247 AAS/Division for Planetary Sciences Meeting Abstracts,
 3248 504.04

3249 Heinze, A., Juric, M., & Kurlander, J. 2023, heliolinx: Open
 3250 Source Solar System Discovery Software,
 3251 <https://github.com/heliolinx/heliolinx>

3252 Hirata, C., & Seljak, U. 2003, MNRAS, 343, 459,
 3253 doi: [10.1046/j.1365-8711.2003.06683.x](https://doi.org/10.1046/j.1365-8711.2003.06683.x)

3254 Holman, M. J., Payne, M. J., Blankley, P., Janssen, R., &
 3255 Kuindersma, S. 2018, AJ, 156, 135,
 3256 doi: [10.3847/1538-3881/aad69a](https://doi.org/10.3847/1538-3881/aad69a)

3257 Howard, J., Reil, K., Claver, C., et al. 2018, in Society of
 3258 Photo-Optical Instrumentation Engineers (SPIE)
 3259 Conference Series, Vol. 10700, Ground-based and
 3260 Airborne Telescopes VII, ed. H. K. Marshall &
 3261 J. Spyromilio, 107003D, doi: [10.1117/12.2312684](https://doi.org/10.1117/12.2312684)

3262 Illingworth, G., Magee, D., Bouwens, R., et al. 2016, arXiv
 3263 e-prints, arXiv:1606.00841,
 3264 doi: [10.48550/arXiv.1606.00841](https://doi.org/10.48550/arXiv.1606.00841)

3265 Ingraham, P., Fagrelius, P., Stubbs, C. W., et al. 2022, in
 3266 Society of Photo-Optical Instrumentation Engineers
 3267 (SPIE) Conference Series, Vol. 12182, Ground-based and
 3268 Airborne Telescopes IX, ed. H. K. Marshall,
 3269 J. Spyromilio, & T. Usuda, 121820R,
 3270 doi: [10.1117/12.2630185](https://doi.org/10.1117/12.2630185)

3271 Ivezić, Ž., Kahn, S. M., Tyson, J. A., et al. 2019a, ApJ,
 3272 873, 111, doi: [10.3847/1538-4357/ab042c](https://doi.org/10.3847/1538-4357/ab042c)

3273 Ivezić, Ž., Kahn, S. M., Tyson, J. A., et al. 2019b, ApJ,
 3274 873, 111, doi: [10.3847/1538-4357/ab042c](https://doi.org/10.3847/1538-4357/ab042c)

3275 Jarvis, M., et al. 2021, Mon. Not. Roy. Astron. Soc., 501,
 3276 1282, doi: [10.1093/mnras/staa3679](https://doi.org/10.1093/mnras/staa3679)

3277 Jenness, T., & Dubois-Felsmann, G. P. 2025, IVOA
 3278 Identifier Usage at the Rubin Observatory, Data
 3279 Management Technical Note DMTN-302, NSF-DOE Vera
 3280 C. Rubin Observatory, doi: [10.71929/rubin/2583848](https://doi.org/10.71929/rubin/2583848)

3281 Jenness, T., Voutsinas, S., Dubois-Felsmann, G. P., &
 3282 Salnikov, A. 2024, arXiv e-prints, arXiv:2501.00544,
 3283 doi: [10.48550/arXiv.2501.00544](https://doi.org/10.48550/arXiv.2501.00544)

3284 Jenness, T., Bosch, J. F., Salnikov, A., et al. 2022, in
 3285 Society of Photo-Optical Instrumentation Engineers
 3286 (SPIE) Conference Series, Vol. 12189, Software and
 3287 Cyberinfrastructure for Astronomy VII, 1218911,
 3288 doi: [10.1117/12.2629569](https://doi.org/10.1117/12.2629569)

3289 Jones, R. L., Yoachim, P., Ivezić, Ž., Neilsen Jr., E. H., &
 3290 Ribeiro, T. 2021, Survey Strategy and Cadence Choices
 3291 for the Vera C. Rubin Observatory Legacy Survey of
 3292 Space and Time (LSST), Project Science Technical Note
 3293 PSTN-051, NSF-DOE Vera C. Rubin Observatory,
 3294 doi: [10.71929/rubin/2584084](https://doi.org/10.71929/rubin/2584084)

3295 Juric, M. 2025, mpsky: Multi-purpose sky catalog
 3296 cross-matching, <https://github.com/mjuric/mpsky>

3297 Jurić, M., Ciardi, D., Dubois-Felsmann, G., & Guy, L.
 3298 2019, LSST Science Platform Vision Document, Systems
 3299 Engineering Controlled Document LSE-319, NSF-DOE
 3300 Vera C. Rubin Observatory, doi: [10.71929/rubin/2587242](https://doi.org/10.71929/rubin/2587242)

3301 Jurić, M., Axelrod, T. S., Becker, A. C., et al. 2023, Data
 3302 Products Definition Document, Systems Engineering
 3303 Controlled Document LSE-163, NSF-DOE Vera C. Rubin
 3304 Observatory, doi: [10.71929/rubin/2587118](https://doi.org/10.71929/rubin/2587118)

3305 Kannawadi, A. 2025, Consistent galaxy colors with
 3306 Gaussian-Aperture and PSF photometry, Data
 3307 Management Technical Note DMTN-190, NSF-DOE Vera
 3308 C. Rubin Observatory, doi: [10.71929/rubin/2583849](https://doi.org/10.71929/rubin/2583849)

3309 Kron, R. G. 1980, ApJS, 43, 305, doi: [10.1086/190669](https://doi.org/10.1086/190669)

3310 Kuijken, K. 2008, A&A, 482, 1053,
 3311 doi: [10.1051/0004-6361:20066601](https://doi.org/10.1051/0004-6361:20066601)

3312 Lange, T., Nordby, M., Pollek, H., et al. 2024, in Society of
 3313 Photo-Optical Instrumentation Engineers (SPIE)
 3314 Conference Series, Vol. 13096, Ground-based and
 3315 Airborne Instrumentation for Astronomy X, ed. J. J.
 3316 Bryant, K. Motohara, & J. R. D. Vernet, 130961O,
 3317 doi: [10.1117/12.3019302](https://doi.org/10.1117/12.3019302)

3318 Léget, P. F., Astier, P., Regnault, N., et al. 2021, A&A,
 3319 650, A81, doi: [10.1051/0004-6361/202140463](https://doi.org/10.1051/0004-6361/202140463)

3320 Lim, K.-T. 2023, Proposal and Prototype for Prompt
 3321 Processing, Data Management Technical Note
 3322 DMTN-219, NSF-DOE Vera C. Rubin Observatory,
 3323 doi: [10.71929/rubin/2585429](https://doi.org/10.71929/rubin/2585429)

3324 Lim, K.-T. 2025, The Consolidated Database of Image
 3325 Metadata, Data Management Technical Note
 3326 DMTN-227, NSF-DOE Vera C. Rubin Observatory,
 3327 doi: [10.71929/rubin/2586436](https://doi.org/10.71929/rubin/2586436)

3328 Louys, M., Tody, D., Dowler, P., et al. 2017, Observation
 3329 Data Model Core Components, its Implementation in the
 3330 Table Access Protocol Version 1.1., IVOA
 3331 Recommendation 09 May 2017
 3332 doi: [10.5479/ADS/bib/2017ivoa.spec.0509L](https://doi.org/10.5479/ADS/bib/2017ivoa.spec.0509L)

3333 LSST Dark Energy Science Collaboration (LSST DESC),
 3334 Abolfathi, B., Alonso, D., et al. 2021, ApJS, 253, 31,
 3335 doi: [10.3847/1538-4365/abd62c](https://doi.org/10.3847/1538-4365/abd62c)

3336 Lust, N. B., Jenness, T., Bosch, J. F., et al. 2023, arXiv
 3337 e-prints, arXiv:2303.03313,
 3338 doi: [10.48550/arXiv.2303.03313](https://doi.org/10.48550/arXiv.2303.03313)

3339 Mandelbaum, R., Hirata, C. M., Seljak, U., et al. 2005,
 3340 MNRAS, 361, 1287,
 3341 doi: [10.1111/j.1365-2966.2005.09282.x](https://doi.org/10.1111/j.1365-2966.2005.09282.x)

3342 Megias Homar, G., Kahn, S. M., Meyers, J. M., Crenshaw,
 3343 J. F., & Thomas, S. J. 2024, The Astrophysical Journal,
 3344 974, 108, doi: [10.3847/1538-4357/ad6cdc](https://doi.org/10.3847/1538-4357/ad6cdc)

3345 Megias Homar, G., Tighe, R., Thomas, S., et al. 2024, in
 3346 Ground-based and Airborne Telescopes X, ed. H. K.
 3347 Marshall, J. Spyromilio, & T. Usuda, Vol. 13094,
 3348 International Society for Optics and Photonics (SPIE),
 3349 130943C, doi: [10.1117/12.3019031](https://doi.org/10.1117/12.3019031)

3350 Melchior, P., Moolekamp, F., Jerdee, M., et al. 2018,
 3351 Astronomy and Computing, 24, 129,
 3352 doi: [10.1016/j.ascom.2018.07.001](https://doi.org/10.1016/j.ascom.2018.07.001)

3353 Mueller, F., et al. 2023, in ASP Conf. Ser., Vol. TBD,
 3354 ADASS XXXII, ed. S. Gaudet, S. Gwyn, P. Dowler,
 3355 D. Bohlender, & A. Hincks (San Francisco: ASP), in
 3356 press. <https://dmtn-243.lsst.io>

3357 Naghib, E., Yoachim, P., Vanderbei, R. J., Connolly, A. J.,
 3358 & Jones, R. L. 2019, The Astronomical Journal, 157, 151,
 3359 doi: [10.3847/1538-3881/aafce](https://doi.org/10.3847/1538-3881/aafce)

3360 NSF-DOE Vera C. Rubin Observatory. 2025a, Legacy
 3361 Survey of Space and Time Data Preview 1 [Data set],
 3362 NSF-DOE Vera C. Rubin Observatory,
 3363 doi: [10.71929/RUBIN/2570308](https://doi.org/10.71929/RUBIN/2570308)

3364 NSF-DOE Vera C. Rubin Observatory. 2025b, Legacy
 3365 Survey of Space and Time Data Preview 1: raw dataset
 3366 type [Data set], NSF-DOE Vera C. Rubin Observatory,
 3367 doi: [10.71929/RUBIN/2570310](https://doi.org/10.71929/RUBIN/2570310)

3368 NSF-DOE Vera C. Rubin Observatory. 2025c, Legacy
 3369 Survey of Space and Time Data Preview 1: visit_image
 3370 dataset type [Data set], NSF-DOE Vera C. Rubin
 3371 Observatory, doi: [10.71929/RUBIN/2570311](https://doi.org/10.71929/RUBIN/2570311)

3372 NSF-DOE Vera C. Rubin Observatory. 2025d, Legacy
 3373 Survey of Space and Time Data Preview 1: deep_coadd
 3374 dataset type [Data set], NSF-DOE Vera C. Rubin
 3375 Observatory, doi: [10.71929/RUBIN/2570313](https://doi.org/10.71929/RUBIN/2570313)

3376 NSF-DOE Vera C. Rubin Observatory. 2025e, Legacy
 3377 Survey of Space and Time Data Preview 1:
 3378 template_coadd dataset type [Data set], NSF-DOE Vera
 3379 C. Rubin Observatory, doi: [10.71929/RUBIN/2570314](https://doi.org/10.71929/RUBIN/2570314)

3380 NSF-DOE Vera C. Rubin Observatory. 2025f, Legacy
 3381 Survey of Space and Time Data Preview 1:
 3382 difference_image dataset type [Data set], NSF-DOE Vera
 3383 C. Rubin Observatory, doi: [10.71929/RUBIN/2570312](https://doi.org/10.71929/RUBIN/2570312)

3384 NSF-DOE Vera C. Rubin Observatory. 2025g, Legacy
 3385 Survey of Space and Time Data Preview 1: Source
 3386 searchable catalog [Data set], NSF-DOE Vera C. Rubin
 3387 Observatory, doi: [10.71929/RUBIN/2570323](https://doi.org/10.71929/RUBIN/2570323)

3388 NSF-DOE Vera C. Rubin Observatory. 2025h, Legacy
 3389 Survey of Space and Time Data Preview 1: Object
 3390 searchable catalog [Data set], NSF-DOE Vera C. Rubin
 3391 Observatory, doi: [10.71929/RUBIN/2570325](https://doi.org/10.71929/RUBIN/2570325)

3392 NSF-DOE Vera C. Rubin Observatory. 2025i, Legacy
 3393 Survey of Space and Time Data Preview 1: ForcedSource
 3394 searchable catalog [Data set], NSF-DOE Vera C. Rubin
 3395 Observatory, doi: [10.71929/RUBIN/2570327](https://doi.org/10.71929/RUBIN/2570327)

3396 NSF-DOE Vera C. Rubin Observatory. 2025j, Legacy
 3397 Survey of Space and Time Data Preview 1: DiaSource
 3398 searchable catalog [Data set], NSF-DOE Vera C. Rubin
 3399 Observatory, doi: [10.71929/RUBIN/2570317](https://doi.org/10.71929/RUBIN/2570317)

3400 NSF-DOE Vera C. Rubin Observatory. 2025k, Legacy
 3401 Survey of Space and Time Data Preview 1: DiaObject
 3402 searchable catalog [Data set], NSF-DOE Vera C. Rubin
 3403 Observatory, doi: [10.71929/RUBIN/2570319](https://doi.org/10.71929/RUBIN/2570319)

3404 NSF-DOE Vera C. Rubin Observatory. 2025l, Legacy
 3405 Survey of Space and Time Data Preview 1:
 3406 ForcedSourceOnDiaObject searchable catalog [Data set],
 3407 NSF-DOE Vera C. Rubin Observatory,
 3408 doi: [10.71929/RUBIN/2570321](https://doi.org/10.71929/RUBIN/2570321)

3409 NSF-DOE Vera C. Rubin Observatory. 2025m, Legacy
 3410 Survey of Space and Time Data Preview 1: CcdVisit
 3411 searchable catalog [Data set], NSF-DOE Vera C. Rubin
 3412 Observatory, doi: [10.71929/RUBIN/2570331](https://doi.org/10.71929/RUBIN/2570331)

3413 NSF-DOE Vera C. Rubin Observatory. 2025n, Legacy
 3414 Survey of Space and Time Data Preview 1: SSOBJECT
 3415 searchable catalog [Data set], NSF-DOE Vera C. Rubin
 3416 Observatory, doi: [10.71929/RUBIN/2570335](https://doi.org/10.71929/RUBIN/2570335)

3417 NSF-DOE Vera C. Rubin Observatory. 2025o, Legacy
 3418 Survey of Space and Time Data Preview 1: SSSource
 3419 searchable catalog [Data set], NSF-DOE Vera C. Rubin
 3420 Observatory, doi: [10.71929/RUBIN/2570333](https://doi.org/10.71929/RUBIN/2570333)

3421 NSF-DOE Vera C. Rubin Observatory. 2025p, Legacy
 3422 Survey of Space and Time Data Preview 1: survey
 3423 property dataset type [Data set], NSF-DOE Vera C.
 3424 Rubin Observatory, doi: [10.71929/RUBIN/2570315](https://doi.org/10.71929/RUBIN/2570315)

3425 Observatory, N.-D. V. C. R. 2021, Rubin Observatory
 3426 LSST Tutorials [Computer Software], NSF-DOE Vera C.
 3427 Rubin Observatory, doi: [10.11578/rubin/dc.20250909.20](https://doi.org/10.11578/rubin/dc.20250909.20)

3428 Oke, J. B., & Gunn, J. E. 1983, ApJ, 266, 713,
 3429 doi: [10.1086/160817](https://doi.org/10.1086/160817)

3430 O'Mullane, W., Economou, F., Huang, F., et al. 2024a, in 3480 Rubin's Survey Cadence Optimization Committee, Bauer,
 3431 Astronomical Society of the Pacific Conference Series, 3481 F. E., Brough, S., et al. 2022, Survey Cadence
 3432 Vol. 535, Astromical Data Analysis Software and Systems 3482 Optimization Committee's Phase 1 Recommendation,
 3433 XXXI, ed. B. V. Hugo, R. Van Rooyen, & O. M. 3483 Project Science Technical Note PSTN-053, NSF-DOE
 3434 Smirnov, 227, doi: [10.48550/arXiv.2111.15030](https://doi.org/10.48550/arXiv.2111.15030) 3484 Vera C. Rubin Observatory, doi: [10.71929/rubin/2584276](https://doi.org/10.71929/rubin/2584276)

3435 O'Mullane, W., AlSayyad, Y., Chiang, J., et al. 2024b, in 3485 Rubin's Survey Cadence Optimization Committee, Bauer,
 3436 Society of Photo-Optical Instrumentation Engineers 3486 F. E., Bianco, F. B., et al. 2023, Survey Cadence
 3437 (SPIE) Conference Series, Vol. 13101, Software and 3487 Optimization Committee's Phase 2 Recommendations,
 3438 Cyberinfrastructure for Astronomy VIII, ed. J. Ibsen & 3488 Project Science Technical Note PSTN-055, NSF-DOE
 3439 G. Chiozzi, 131012B, doi: [10.1117/12.3018005](https://doi.org/10.1117/12.3018005) 3489 Vera C. Rubin Observatory, doi: [10.71929/rubin/2585249](https://doi.org/10.71929/rubin/2585249)

3440 Onken, C. A., Wolf, C., Bessell, M. S., et al. 2019, PASA, 3490 Rubin's Survey Cadence Optimization Committee, Bianco,
 3441 36, e033, doi: [10.1017/pasa.2019.27](https://doi.org/10.1017/pasa.2019.27) 3491 F. B., Jones, R. L., et al. 2025, Survey Cadence
 3442 Park, H. Y., Nomerotski, A., & Tsybychev, D. 2017, 3492 Optimization Committee's Phase 3 Recommendations,
 3443 Journal of Instrumentation, 12, C05015, 3493 Project Science Technical Note PSTN-056, NSF-DOE
 3444 doi: [10.1088/1748-0221/12/05/C05015](https://doi.org/10.1088/1748-0221/12/05/C05015) 3494 Vera C. Rubin Observatory, doi: [10.71929/rubin/2585402](https://doi.org/10.71929/rubin/2585402)

3445 Petrosian, V. 1976, ApJL, 210, L53, 3495 Rykoff, E. S., Tucker, D. L., Burke, D. L., et al. 2023, arXiv
 3446 doi: [10.1086/18230110.1086/182253](https://doi.org/10.1086/18230110.1086/182253) 3496 e-prints, arXiv:2305.01695,
 3447 Plazas, A. A., Shapiro, C., Smith, R., Huff, E., & Rhodes, 3497 doi: [10.48550/arXiv.2305.01695](https://doi.org/10.48550/arXiv.2305.01695)

3448 J. 2018, Publications of the Astronomical Society of the 3498 Saunders, C. 2024, Astrometric Calibration in the LSST
 3449 Pacific, 130, 065004, doi: [10.1088/1538-3873/aab820](https://doi.org/10.1088/1538-3873/aab820) 3499 Pipeline, Data Management Technical Note DMTN-266,
 3450 Plazas Malagón, A. A., Digel, S. W., Roodman, A., 3500 NSF-DOE Vera C. Rubin Observatory,
 3451 Broughton, A., & LSST Camera Team. 2025, LSSTCam 3501 doi: [10.71929/rubin/2583846](https://doi.org/10.71929/rubin/2583846)

3452 and LSSTComCam Focal Plane Layouts, Camera 3502 Schutt, T., Jarvis, M., Roodman, A., et al. 2025, The Open
 3453 Technical Note CTN-001, NSF-DOE Vera C. Rubin 3503 Journal of Astrophysics, 8, 26, doi: [10.33232/001c.132299](https://doi.org/10.33232/001c.132299)

3454 Observatory, doi: [10.71929/rubin/2584019](https://doi.org/10.71929/rubin/2584019) 3504 Sérsic, J. L. 1963, Boletin de la Asociacion Argentina de
 3455 Plazas Malagón, A. A., Waters, C., Broughton, A., et al. 3505 Astronomia La Plata Argentina, 6, 41

3456 2025, Journal of Astronomical Telescopes, Instruments, 3506 Sérsic, J. L. 1968, Atlas de Galaxias Australes (Cordoba,
 3457 and Systems, 11, 011209, 3507 Argentina: Observatorio Astronomico)

3458 doi: [10.1117/1.JATIS.11.1.011209](https://doi.org/10.1117/1.JATIS.11.1.011209) 3508 Shanks, T., Metcalfe, N., Chehade, B., et al. 2015,
 3459 Refregier, A. 2003, ARA&A, 41, 645, 3509 MNRAS, 451, 4238, doi: [10.1093/mnras/stv1130](https://doi.org/10.1093/mnras/stv1130)

3460 doi: [10.1146/annurev.astro.41.111302.102207](https://doi.org/10.1146/annurev.astro.41.111302.102207) 3510 SLAC National Accelerator Laboratory, & NSF-DOE Vera
 3461 Reiss, D. J., & Lupton, R. H. 2016, Implementation of 3511 Rubin Observatory. 2024, LSST Commissioning
 3462 Image Difference Decorrelation, Data Management 3512 Camera, SLAC National Accelerator Laboratory (SLAC),
 3463 Technical Note DMTN-021, NSF-DOE Vera C. Rubin 3513 Menlo Park, CA (United States),
 3464 Observatory, doi: [10.71929/rubin/2586490](https://doi.org/10.71929/rubin/2586490) 3514 doi: [10.71929/RUBIN/2561361](https://doi.org/10.71929/RUBIN/2561361)

3465 Roodman, A., Rasmussen, A., Bradshaw, A., et al. 2024, in 3515 Slater, C. T., Ivezić, Ž., & Lupton, R. H. 2020, AJ, 159, 65,
 3466 Society of Photo-Optical Instrumentation Engineers 3516 doi: [10.3847/1538-3881/ab6166](https://doi.org/10.3847/1538-3881/ab6166)

3467 (SPIE) Conference Series, Vol. 13096, Ground-based and 3517 Smith, G. E. 2010, Rev. Mod. Phys., 82, 2307,
 3468 Airborne Instrumentation for Astronomy X, ed. J. J. 3518 doi: [10.1103/RevModPhys.82.2307](https://doi.org/10.1103/RevModPhys.82.2307)

3469 Bryant, K., Motohara, & J. R. D. Vernet, 130961S, 3519 Stalder, B., Reil, K., Claver, C., et al. 2020, in Society of
 3470 doi: [10.1117/12.3019698](https://doi.org/10.1117/12.3019698) 3520 Photo-Optical Instrumentation Engineers (SPIE)

3471 Rubin, V. C., & Ford, Jr., W. K. 1970, ApJ, 159, 379, 3521 Conference Series, Vol. 11447, Ground-based and
 3472 doi: [10.1086/150317](https://doi.org/10.1086/150317) 3522 Airborne Instrumentation for Astronomy VIII, ed. C. J.
 3473 Rubin, V. C., Ford, Jr., W. K., & Thonnard, N. 1980, ApJ, 3523 Evans, J. J. Bryant, & K. Motohara, 114470L,
 3474 238, 471, doi: [10.1086/158003](https://doi.org/10.1086/158003) 3524 doi: [10.1117/12.2561132](https://doi.org/10.1117/12.2561132)

3525 Stalder, B., Reil, K., Aguilar, C., et al. 2022, in Society of
 3526 Photo-Optical Instrumentation Engineers (SPIE)
 3527 Conference Series, Vol. 12184, Ground-based and
 3528 Airborne Instrumentation for Astronomy IX, ed. C. J.
 3529 Evans, J. J. Bryant, & K. Motohara, 121840J,
 3530 doi: [10.1117/12.2630184](https://doi.org/10.1117/12.2630184)

3531 Stalder, B., Munoz, F., Aguilar, C., et al. 2024, in Society
 3532 of Photo-Optical Instrumentation Engineers (SPIE)
 3533 Conference Series, Vol. 13094, Ground-based and
 3534 Airborne Telescopes X, ed. H. K. Marshall, J. Spyromilio,
 3535 & T. Usuda, 1309409, doi: [10.1117/12.3019266](https://doi.org/10.1117/12.3019266)

3536 Swinbank, J. D., Axelrod, T. S., Becker, A. C., et al. 2020,
 3537 Data Management Science Pipelines Design, Data
 3538 Management Controlled Document LDM-151, NSF-DOE
 3539 Vera C. Rubin Observatory, doi: [10.71929/rubin/2587108](https://doi.org/10.71929/rubin/2587108)

3540 Taranu, D. S. 2025, The MultiProFit astronomical source
 3541 modelling code, Data Management Technical Note
 3542 DMTN-312, NSF-DOE Vera C. Rubin Observatory,
 3543 doi: [10.71929/rubin/2584108](https://doi.org/10.71929/rubin/2584108)

3544 Taylor, M. 2011, TOPCAT: Tool for OPerations on
 3545 Catalogues And Tables,, Astrophysics Source Code
 3546 Library, record ascl:1101.010

3547 Thomas, S., Connolly, A., Crenshaw, J. F., et al. 2023, in
 3548 Adaptive Optics for Extremely Large Telescopes
 3549 (AO4ELT7), 67, doi: [10.13009/AO4ELT7-2023-069](https://doi.org/10.13009/AO4ELT7-2023-069)

3550 Tonry, J. L., Denneau, L., Heinze, A. N., et al. 2018, PASP,
 3551 130, 064505, doi: [10.1088/1538-3873/aabadf](https://doi.org/10.1088/1538-3873/aabadf)

3552 Wainer, T. M., Davenport, J. R. A., Bellm, E. C., et al.
 3553 2025, Research Notes of the American Astronomical
 3554 Society, 9, 171, doi: [10.3847/2515-5172/adecef](https://doi.org/10.3847/2515-5172/adecef)

3555 Wang, D. L., Monkewitz, S. M., Lim, K.-T., & Becla, J.
 3556 2011, in State of the Practice Reports, SC '11 (New
 3557 York, NY, USA: ACM), 12:1–12:11,
 3558 doi: [10.1145/2063348.2063364](https://doi.org/10.1145/2063348.2063364)

3559 Waters, C. Z., Magnier, E. A., Price, P. A., et al. 2020,
 3560 ApJS, 251, 4, doi: [10.3847/1538-4365/abb82b](https://doi.org/10.3847/1538-4365/abb82b)

3561 Whitaker, K. E., Ashas, M., Illingworth, G., et al. 2019,
 3562 ApJS, 244, 16, doi: [10.3847/1538-4365/ab3853](https://doi.org/10.3847/1538-4365/ab3853)

3563 Wu, X., Roby, W., Goldian, T., et al. 2019, in Astronomical
 3564 Society of the Pacific Conference Series, Vol. 521,
 3565 Astronomical Data Analysis Software and Systems
 3566 XXVI, ed. M. Molinaro, K. Shortridge, & F. Pasian, 32

3567 Xin, B., Claver, C., Liang, M., et al. 2015, ApOpt, 54,
 3568 9045, doi: [10.1364/AO.54.009045](https://doi.org/10.1364/AO.54.009045)

3569 Yoachim, P. 2022, Survey Strategy: Rolling Cadence,
 3570 Project Science Technical Note PSTN-052, NSF-DOE
 3571 Vera C. Rubin Observatory, doi: [10.71929/rubin/2584109](https://doi.org/10.71929/rubin/2584109)

3572 Yoachim, P., Jones, L., Eric H. Neilsen, J., & Becker, M. R.
 3573 2024, lsst/rubin_scheduler: v3.0.0, v3.0.0 Zenodo,
 3574 doi: [10.5281/zenodo.13985198](https://doi.org/10.5281/zenodo.13985198)

3575 Zhang, T., Almoubayyed, H., Mandelbaum, R., et al. 2023,
 3576 MNRAS, 520, 2328, doi: [10.1093/mnras/stac3350](https://doi.org/10.1093/mnras/stac3350)